การศึกษากลศาสตร์ไฟฟ้าของอนุภาคที่มีรูปร่างไม่เป็นทรงกลมภายใต้สนามไฟฟ้าในระบบฉนวน

นายเวียต คอค ฮุย

วิทยานิพนธ์นี้เป็นส่วนหนึ่งของการศึกษาตามหลักสูตรปริญญาวิศวกรรมศาสตรดุษฎีบัณฑิต
สาขาวิชาวิศวกรรมไฟฟ้า ภาควิชาวิศวกรรมไฟฟ้า
คณะวิศวกรรมศาสตร์ จุฬาลงกรณ์มหาวิทยาลัย
ปีการศึกษา 2556
ลิขสิทธิ์ของจุฬาลงกรณ์มหาวิทยาลัย

STUDY ON THE ELECTROMECHANICS OF NON-SPHERICAL PARTICLES UNDER
ELECTRIC FIELD IN DIELECTRIC SYSTEMS

Mr. Viet Quoc Huynh

A Dissertation Submitted in Partial Fulfillment of the Requirements

for the Degree of Doctor of Philosophy Program in Electrical Engineering

Department of Electrical Engineering

Faculty of Engineering

Chulalongkorn University

Academic Year 2013

Thesis Title	STUDY ON THE ELECTROMECHANICS OF NON-SPHERICAL PARTICLES UNDER ELECTRIC FIELD IN DIELECTRIC SYSTEMS
By	Mr. Viet Quoc Huynh
Field of Study	Electrical Engineering
Thesis Advisor	Associate Professor Boonchai Techaumnat
Thesis Co-Advisor	Professor Kunihiko Hidaka

Accepted by the Faculty of Engineering, Chulalongkorn University in Partial Fulfillment of the Requirements for the Doctoral Degree

⋯⋯⋯⋯⋯⋯⋯⋯⋯⋯⋯⋯⋯⋯ Dean of the Faculty of Engineering

(Professor Bundhit Eua-arporn)

THESIS COMMITTEE

⋯⋯⋯⋯⋯⋯⋯⋯⋯⋯⋯⋯⋯⋯ Chairman

(Assistant Professor Komson Petcharaks)

⋯⋯⋯⋯⋯⋯⋯⋯⋯⋯⋯⋯⋯⋯ Thesis Advisor

(Associate Professor Boonchai Techaumnat)

⋯⋯⋯⋯⋯⋯⋯⋯⋯⋯⋯⋯⋯⋯ Thesis Co-Advisor

(Professor Kunihiko Hidaka)

⋯⋯⋯⋯⋯⋯⋯⋯⋯⋯⋯⋯⋯⋯ Examiner

(Assistant Professor Weerapun Rungseevijitprapa)

⋯⋯⋯⋯⋯⋯⋯⋯⋯⋯⋯⋯⋯⋯ Examiner

(Doctor Channarong Banmongkol)

⋯⋯⋯⋯⋯⋯⋯⋯⋯⋯⋯⋯⋯⋯ External Examiner

(Assistant Professor Peerawut Yutthagowith)

เวียต คอค ฮุย : การศึกษากลศาสตร์ไฟฟ้าของอนุภาคที่มีรูปร่างไม่เป็นทรงกลมภายใต้
สนามไฟฟ้าในระบบฉนวน. (STUDY ON THE ELECTROMECHANICS OF NON-
SPHERICAL PARTICLES UNDER ELECTRIC FIELD IN DIELECTRIC SYSTEMS) อ.ที่
ปรึกษาวิทยานิพนธ์หลัก: รศ. บุญชัย เตชะอำนาจ,   อ.ที่ปรึกษาวิทยานิพนธ์ร่วม: Prof.
Kunihiko Hidaka, 146 หน้า.

ระบบฉนวนก๊าซ เช่น สวิตช์เกียร์แบบฉนวนก๊าซ หรือสายส่งแบบฉนวนก๊าซ ถูกใช้อย่าง
แพร่หลายในระบบส่งกำลังไฟฟ้าระบบดังกล่าวสามารถเพิ่มความปลอดภัยและความน่าเชื่อถือให้แก่การ
ส่งกำลังไฟฟ้าได้   การผิดพร่องส่วนใหญ่ที่เกิดขึ้นในการทำงานของระบบฉนวนก๊าซ เกิดจากอนุภาค
ตัวนำที่ปนอยู่ในระบบ   ดังนั้น จึงได้มีการศึกษาการเคลื่อนที่ของอนุภาคภายใต้สนามไฟฟ้าจากกลุ่ม
นักวิจัยมากมาย เพื่อเป็นพื้นฐานของการจับยึดอนุภาค แม้ว่ามีการพบผลกระทบของโคโรนาที่มีต่อการ
เคลื่อนที่ของอนุภาค แต่ยังไม่สามารถอธิบายผลกระทบดังกล่าวได้อย่างสมบูรณ์ วิทยานิพนธ์นี้มี
วัตถุประสงค์ที่จะวิเคราะห์และทดลองด้านกลศาสตร์ไฟฟ้าของอนุภาคตัวนำหรืออนุภาคฉนวนที่มีรูปร่าง
ไม่เป็นทรงกลมบนระนาบตัวนำ และทำให้ทราบผลของรูปร่างและโคโรนาดีสชาร์จที่มีต่อการเคลื่อนที่
ของอนุภาคภายใต้สนามไฟฟ้า   การวิเคราะห์ใช้รูปแบบการจัดเรียงอนุภาคตัวนำหรือฉนวน ซึ่งอยู่บน
หรือลอยอยู่เหนือระนาบกราวนด์   การวิเคราะห์ความสัมพันธ์ของปริมาณทางไฟฟ้าสถิต กับ
พารามิเตอร์ต่างๆ ของการจัดเรียง ปริมาณทางไฟฟ้าสถิตได้แก่ สนามไฟฟ้า ประจุเหนี่ยวนำ แรง และ
แรงบิด การวิเคราะห์พิจารณา 2 กรณี คือ   แกนเอกของทรงคล้ายทรงกลมตั้งฉาก หรือทำมุมกับระนาบ
การวิเคราะห์ใช้มัลติโพลและการกระจายมัลติโพลใหม่สำหรับระบบพิกัดทรงคล้ายทรงกลม ซึ่งให้ผลที่มี
ความแม่นยำสูง สำหรับการทดลองวิทยานิพนธ์นี้วัดหาสนามไฟฟ้าที่ทำให้อนุภาคยกตัวขึ้นและสังเกต
พฤติกรรมของอนุภาคภายใต้ระบบอิเล็กโตรดคู่ขนาน อนุภาคทรงคล้ายทรงกลมแบนข้างและลวด
อนุภาคถูกใช้ในการทดลอง แรงและแรงบิดบนลวดอนุภาคถูกประมาณโดยใช้แบบจำลองทรงคล้ายทรง
กลมแบนข้างในการวิจารณ์ผล

ภาควิชา	วิศวกรรมไฟฟ้า	ลายมือชื่อนิสิต	....
สาขาวิชา	วิศวกรรมไฟฟ้า	ลายมือชื่อ อ.ที่ปรึกษาวิทยานิพนธ์หลัก	....
ปีการศึกษา	2556	ลายมือชื่อ อ.ที่ปรึกษาวิทยานิพนธ์ร่วม	....

5471440921 : MAJOR ELECTRICAL ENGINEERING

KEYWORDS: ELECTROMECHANICS PROLATE SPHEROID IMAGE METHOD MULTIPOLE RE-EXPANSION METALLIC PARTICLES PARTIAL DISCHARGE

VIET QUOC HUYNH: STUDY ON THE ELECTROMECHANICS OF NON-SPHERICAL PARTICLES UNDER ELECTRIC FIELD IN DIELECTRIC SYSTEMS. ADVISOR: ASSOC. PROF. BOONCHAI TECHAUMNAT, CO-ADVISOR: PROF. KUNIHIKO HIDAKA, 146 pp.

Gas insulated systems such as gas insulated switchgears (GIS) and gas insulated transmission lines (GITL) are widely used in the electric power systems for increasing operational reliability and safety as well as reducing space. Most of failures in operation of gas insulated systems are caused by contaminating conducting particles. To improve the reliability of the systems, many researchers have investigated the movement behavior of the particles as the foundation for particle deactivation. Although the effect of the corona discharge is found on the particle movement, the effect has not been fully explained yet. The objective of this dissertation is to clarify the electromechanics of conducting and dielectric non-spherical particles lying on an electrode under electric field, and the effects of the particle profile and the corona discharge on the particle movement. This dissertation describes analytical and experimental studies on the electromechanics of non-spherical particles under external electric field. For the analysis, the configuration is a conducting or dielectric prolate spheroid lying on or above a grounded plane under uniform electric field. The analysis determines the relationships between the electrostatic quantities and parameters of the configuration. The electrostatic quantities are electric field, induced charge, force, and torque. The analysis is done for two arrangements in which the major axis of the spheroid (i) is perpendicular to the plane or (ii) makes a tilt angle with the plane. In the analysis, the electric field is calculated by using the method of multipole images and the multipole re-expansion in prolate spheroidal coordinates to realize high accuracy. The force and torque are determined from the stress on the spheroid surface which is a function of the electric field. For the experiment, the measurement of lifting electric field and the observation of the particle movement between two parallel-plate electrodes are carried out. The spheroidal particles and the wire particles are used in the experiment. The force and torque on a wire particle in the movement are estimated by using an approximated model of a prolate spheroid for discussion.

Department:	Electrical Engineering	Student's Signature	-------------------------------
Field of Study:	Electrical Engineering	Advisor's Signature	-------------------------------
Academic Year:	2013	Co-Advisor's Signature	-------------------------------

ACKNOWLEDGEMENTS

CONTENTS

List of Tables

List of Figures

List of Notations

Symbols

a	z coordinate of focal points of ellipses
b	minor semi-axis of spheroid
c	major semi-axis of spheroid
d	horizontal distance between **p** and **o**
f	force per unit area (electrostatic stress)
g	gravitational acceleration
l	arc length measured from spheroid pole
i, j, n, m	integer indices
r	radial coordinate of spherical coordinates
x, y, z	Cartesian coordinates, x is sometime used as a variable
$B_{n,m}$	(n, m)th-order spheroidal multipole
L	arc length between two poles of a spheroid or length of a particle
$L_{n,m}$	real-number potential coefficient
E	electric field
E_0	externally applied electric field
E_L	lifting electric field
E_R	rotating electric field
F_e	electrostatic force (Coulomb force)
F_g	gravitational force
F_0, F_1, F_2	quantities used for normalizing force
Q	induced charge when particle is in contact with electrode
Q_i	charge amount on particle
Q_0, Q_1, Q_2	quantities used for normalizing charge
$P_{n,m}, Q_{n,m}$	associated Legendre functions of the first and second kind

N	number of spheroidal harmonics used in expansion
R	radius of sphere or cylinder
S	surface area
T_e	electrostatic torque
T_g	gravitational torque
T_{tot}	total torque
U_i	corona inception voltage
V	volume
X, Y, Z	Cartesian coordinates
α	tilt angle between major axis of spheroid and grounded plane
ε_0	permittivity of vacuum or gaseous dielectric
ε_E	permittivity of background medium
ε_S	permittivity of dielectric particle
$\varepsilon = \varepsilon_S / \varepsilon_E$	dielectric-constant ratio
η, ξ, φ	prolate spheroidal coordinates
ϕ, ψ	potential
σ_f	density of free charges on spheroid surface
σ_b	density of polarization charges (bound charges) on spheroid surface

CHAPTER I

INTRODUCTION

1.1 Overview of gas insulated systems

A half century has passed since a gas insulated system was first introduced in the electric power system. Nowadays, gas insulated systems are widely used in the transmission and substation systems due to their advantages over the atmospheric air insulated systems such as high operational reliability and safety, compactness, and non-flammability. Examples of gas insulated systems are gas insulated switchgears, gas insulated transmission lines, and gas insulated transformers. They are often used in urban areas due to their compactness. In practice, the gas insulated systems are now operating with rated voltage up to 1000 kV. The common gas pressure in the systems was from 0.3 to 0.5 MPa. Schematic diagram of a gas insulated system is shown in Figure 1.1.
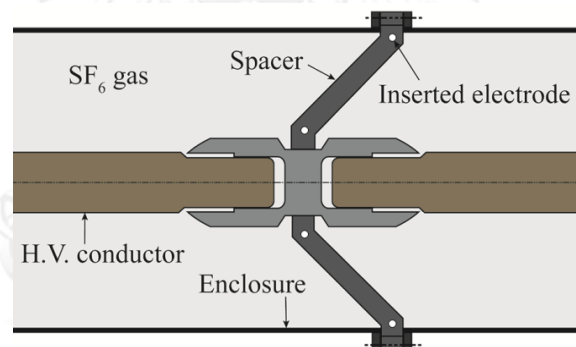
Figure 1.1. Schematic diagram of gas insulated systems.

Most gas insulated systems use SF_6. SF_6 has saliently insulating properties such as high dielectric strength, about 3 times greater than that of conventional air at the same pressure, good arc-interruption properties, and good characteristics of heat transfer. However, the dielectric strength of SF_6 is very sensitive to electric field concentration which possibly results from the roughness of electrode surface, contaminating conducting and non-conducting particles, or spacers. Also, SF_6 is a greenhouse gas with a long atmospheric life time. Relatively small leakage of SF_6 into atmospheric can cause a significant impact on the global climate change. However, a substituting gas or a gas mixture which has suitable characteristics compared to SF_6 has not yet been found. The optimal use of SF_6 achieved by minimizing the apparatus size is then preferable for the environmental aspect.

In general, the insulation strength of gas insulated systems is governed by the gaseous insulation and the structure of the systems. The main causes, which may contribute to the reduction of the insulation strength, are metallic particle contamination, spacers, electrode-surface roughness. The discharge may develop into a complete breakdown in gaseous dielectric. In operation, the partial discharges are detected by a monitoring system to observe if the discharge magnitude exceeds a threshold value.

It is found that most of the failures in gas insulated systems are caused by the particle contamination [1]. Its effect on the insulation performance of the systems depends on various factors such as particle size, shape, material, gas pressure, and the waveform of the applied voltage. The loss in the dielectric strength of the particle contaminated systems can exceed 50% and becomes more seriously with further increasing gas pressure [2, 3].

1.2 Particle contamination

Manufactures of gas insulated equipments ensure that before shipping, all components of the equipments are free from solid foreign particles. However, the particles are inevitably present in the practical equipments [4]. The most common causes are mechanical vibrations during shipment and service, thermal expansion, and contraction at expansion joints machined imperfectly, etc. The particles found in actual gas insulated systems are mostly smaller than 0.5 mm, however; particles longer than 2 mm were also collected [5]. They have a variety of geometrical profiles, rather elongated and needle. An increase in the length of the particles extremely reduces in the breakdown strength of the systems, whereas an increase in the particle width is not a dominant factor [6, 7].

The contaminating particles can be classified as conductor and dielectric ones. The behavior of conducting particles is simpler than that of dielectric ones under electric field. A conducting particle gains charges when it makes a contact with an electrode. The charged particle tends to move between electrodes by the Coulomb force. A dielectric particle is subject to the dielectrophoretic (DEP) force and the Coulomb force which exists when the particle is charged. The DEP force tends to drive a dielectric particle toward the region of higher field. The particles intensify electric field significantly in their vicinity, as generally explained for composite dielectric systems in [8]. Therefore, they may cause corona discharge or complete breakdown in the gaseous dielectric. In addition, the conducting particles may adhere to spacers, resulting in flashover along the spacer surface [4, 9]. Unlike the

conducting particles, the dielectric ones do not reduce significantly the dielectric strength of the gas insulated systems unless their surface accumulates charges from the gaseous medium [3, 10, 11].

Size reduction of the gas insulated systems is on the way. A stronger field strength accompanying with decreasing space for particle manipulation makes the control of the contaminating particles more important.

1.3 Literature review

As mentioned in the previous section, conducting particles have adverse effects on the gas insulated systems. To further increase the reliability of gas insulated systems, extensive laboratory investigations have been conducted on the effects of conducting particles on the insulation strength of the systems. The investigations can be classified as follows: (i) particle-initiated corona discharge and breakdown, (ii) behavior of the particle movement, and (iii) methods of particle deactivation. The investigations are mostly carried out in air and SF_6 with various pressures under the application of AC or DC voltage. In the investigations, sphere and cylinder (wire) were usually used to represent the profile of the actual particles in gas insulated systems. Some researchers used prolate spheroidal particles for the investigation on the particle-initiated discharge and breakdown. Material of the particles used in the investigations was aluminum, copper, or stainless steel. The used spherical particles usually had a radius between 0.25 mm and 1 mm. Other particles with width from 0.1 mm to 1 mm and length from 1 to 10 mm were usually used. The end of the wire particles might be in hemisphere, right cut, slanting cut, or conical profile.

1.3.1 Particle-initiated discharge

Corona discharge initiated by foreign conducting particles can cause the deterioration of spacers or develop into a complete breakdown in gaseous dielectric. Besides, the methods detecting the existence of the particles are generally based on the activity of the corona discharge. Thus, many studies have been done to clarify the characteristic and mechanism of the particle-initiated discharge. The studies might be divided into two categories based on the position of the particles.

First, the particles are in contact with an electrode or electrically floating in gaseous dielectric in the absence of spacer. The results from the studies indicate that the corona discharge depends strongly on the shape, the length, and the location of the particles. For the same distance of an electrode gap, the corona inception voltage is smaller for longer particles and sharper ending profiles [12, 13]. When the

particle is in contact with an electrode, the corona inception voltage is smaller in comparison with the case that it is separated from the electrode [14, 15]. If the particle exists in the vicinity of a negative electrode, the inception voltage increases considerably with the separation between the particle and the electrode. If the particle is near a positive electrode, a stable corona never occurs [14]. Hara et al. [15-18] investigated the mechanism of the corona discharge by increasing the applied voltage until the breakdown took place and observing the corona current waveform and light emission produced by the discharge. They found that for a floating particle, negative and positive coronas might appear simultaneously at both ends of the particle.

Second, the particles are near or on the spacer surface. For the former case, the effect of the distance between the particle and the spacer on the corona inception voltage is negligible [9]. For the latter case, the corona inception voltage depends on the shape of the spacer, the geometrical profile of the particles, and the location on the spacer of the particles [4, 19, 20]. The corona inception voltage reduces significantly with the particle length, and minimal when the particle is in contact with the electrode compared with other cases of the separation.

1.3.2 Behavior of particle movement

Movement of a conducting particle in gas insulated equipments may result in space changes which play an important role on the characteristics of the corona discharge and breakdown inside the equipments. Besides, the clear understanding of the particle movement is applicable to the investigation of methods deactivating the particles. Thus, considerable efforts have been made to study experimentally and theoretically the movement of conducting particles under electric field. However, most of the studies are restricted to the behavior after the particles are lifted from an electrode.

When a conducting particle lies on a grounded lower electrode of a parallel electrode configuration under an applied electric field, the particle is charged to be at the zero potential. The particle is lifted from the electrode surface by the electrostatic force when this force is greater than the gravitational force. The particle then moves to the upper electrode. When it makes an impact on the upper electrode, the charge polarity on the particle is reversed. Subsequently, the particle moves back the lower electrode. The configuration of a conducting particle in contact with a grounded plane under external field was examined as an important ground to determine the field strength, the lifting electric field, that lifts the particle

from the plane [21, 22]. Theoretically, the lifting electric field was determined from the balance between the electrostatic force and the gravitational force. For a spherical particle, the electrostatic force was analyzed by Felici [23] and by Hara and Akazaki [24]. For a wire particle, the force was estimated by using the model an infinitely long cylinder or a hemispheroid when the particle lies or stands on the plane, respectively [25].

The movement of conducting particles between two electrodes is greatly influenced by the waveform of the applied voltage [26, 27] and the particle shape [25, 28]. Under DC voltage, the particle crosses the electrode gap after lifting from the grounded electrode because the electric field direction does not change. However, under AC voltage, the particle plays a random-like behavior due to the interaction of the induced charge and the continuously changed field. The particle may repeat up-and-down movement on the lower electrode. The height of the particle movement increases with the applied voltage. If the applied voltage is sufficiently large, the particle can approach the upper electrode. Note that the particle movement is also affected by the applied voltage frequency [29]. For the effect of the particle shape, an elongated wire particle is more mobile than a spherical one due to larger charge-to-mass ratio. Also, the movement of the wire particles is more complicated than that of the spherical particles and depends heavily on the corona discharge at their ends [25, 30], . With presence of the corona discharge, a wire particle may exhibit either a precessional motion or a firefly phenomenon around a negative electrode. The processional motion consists of two kinds of rotation about its own axis and that about the vertical axis [31]. During this motion, there exists a microdischarge between the particle and the electrode [31]. The firefly phenomenon is the "dancing" about in dynamic equilibrium [32].

Hara and Sakai et al. investigated the movement of sphere and wire particles in nonuniform electric field produced by non-parallel plate electrode configurations without or with spacers. They found that the spherical particles may move along an electrode surface toward the higher-field region by the electrical gradient force and then lift from the electrode [27]. The wire particles in the precessional motion or the firefly phenomenon may also move toward the higher-field region and then trigger a complete breakdown [33]. Their results [21, 34] indicate that when approaching the spacers, the spherical particles hardly adhere to the spacer. For the wire particles, they can more easily adhere to the spacer for the case of without steady corona discharge on the particles than for that of presence of steady corona discharge.

The studies on the particle movement show that the different behaviors in the movement of elongated conducting wire particles result from the degree of the corona discharge on the particles. However, the mechanism of the behaviors has not been fully explained based on force and torque. In addition, conducting particles in practical gas insulated systems have a variety of geometrical profiles, not limited to be spherical or cylindrical. The movement of non-spherical particles under electric field is still unclear.

1.3.3 Methods of particle deactivation

The elimination of foreign conducting particles in actual gas insulated equipments is nearly impossible while even one particle can initiate a complete breakdown in gaseous dielectric. Hence, methods which prevent the harmful effect of the particles are necessary. Various methods have been proposed to deactivate the particles in gaseous dielectric, and some are in current use.

The common method that is currently employed by manufactures is electrostatic particle traps [35]. The philosophy of this method is to provide designated low field areas in the gaseous-dielectric volume. When the particles move and enter these areas, they can be safely trapped and contained. The goal in designing the trap consists of efficiently capturing the particles and preventing their subsequent escape. The popular type of the particle trap is slot traps on or above the inner surface of the enclosure. Figure 1.2 shows an example of the common particle trap that is slotted metallic cylinders mounted around a spacer above the enclosure surface [36, 37]. The effectiveness of a particle trap depends on the slot width and the number of slots per length unit. The movement of the particles in the electric field also affects the trapping [36]. The weak point of the particle trap is to allow that the particles move under electric field stress until they have been trapped [38]. Khan et al. [39] suggested a new configuration of particle deactivation based on the particle movement in the nonuniform field regions around various shaped spacers. The trapping methods are effective with spherical particles but not much ineffective with wire particles particularly elongated ones [39, 40]. Phansiri and Techaumnat [41] investigated theoretically and experimentally the trap of spherical particles by using the DEP force. The investigation results confirm the applicability of the DEP force for trapping; however, the performance deactivation still depended on the initial position of the particle. Not that, coated electrodes may be used to prevent the particle movement in gas insulated systems [42-45]. However, the field control becomes more complicated in the configurations of coated electrodes.
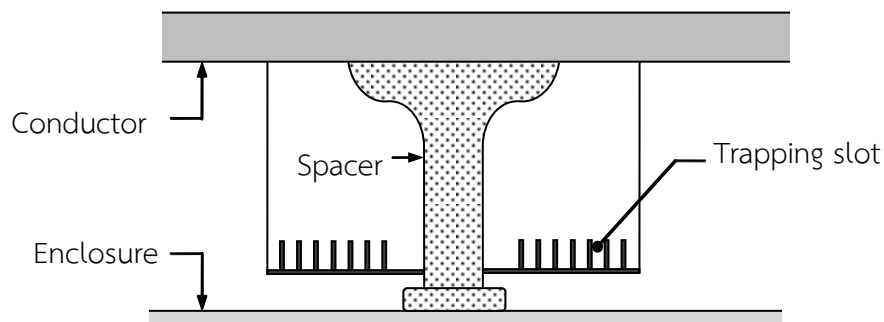
Figure 1.2. Schematic diagram of a common particle trap mounted around a spacer [36, 37].

1.4 Objectives and scope of dissertation

The objectives of this dissertation are (i) to analyze the electromechanics of conducting and dielectric non-spherical particles on a grounded plane under external electric field and (ii) to investigate the effects of the particle profile and corona discharge on the movement of non-spherical conducting particles under electric field.

The non-spherical particle is approximated as prolate spheroidal one for the analysis. Prolate spheroidal and wire particles are used for the experimental study. The particle size in the experiments was between 2 and 4 mm.

1.5 Dissertation outline

This dissertation is organized as follows:

Chapter II presents the theoretical background of the studies in this dissertation. This chapter first gives the formulae of the maximal field, induced charge, and electrostatic force for simple configurations of a cylinder, sphere, or hemispheroid. The formulae of the lifting electric field for conducting spherical and cylindrical (wire) particles are also given. Next, this chapter explains principle characteristics of positive and negative corona discharges in a typical point-to-plane electrode system.

Chapter III introduces the asymmetric (AS) and three-dimensional (3D) configurations of the analysis and the method of multipole images in prolate spheroidal coordinates, which is applied to the electric field calculation. The procedure of the calculation in an iterative manner and the calculation formulae of induced charge, force, and torque on the particles are presented. The analytical

solutions for isolated conducting and dielectric prolate spheroids under electric field are also given for reference.

Chapters IV and V present the analytical results for the AS and 3D configurations, respectively. The author focuses on the relationship of the electric field, induced charge, force, and torques on the geometrical and electrical parameters of the configurations. For the case of a conducting spheroid lying on an electrode in a 3D configuration, the effects of the material and geometry of the spheroid on the electromechanical behavior of the spheroid are considered in detail.

Chapter VI presents the details of the experimental setup, procedures, and test particles used in this dissertation.

Chapter VII presents and discusses experimental results of the lifting electric field and the movement behavior of spheroidal and wire particles. The experimental results are compared with the theoretical prediction. For the wire particles, the author considers the effect of applied voltage magnitude and initial orientation of the particles on the electrode on the movement of the particles. The effect of corona discharge on the particle movements is discussed based on the force and torque estimated by using the prolate spheroid model.

Chapter VIII summarizes the main results obtained from the analysis and the experiment in this dissertation.

CHAPTER II

THEORETICAL BACKGROUND

2.1 Electrostatic behaviors in simple configurations

Configurations of a conductor in contact with a grounded plane under electric field are useful in studying the movement of small particles and have various electrostatic applications. Felici [23] treated the configurations shown in Figure 2.1. Solutions of those configurations are explained here as a reference for the subsequent chapters. Figure 2.1a shows the configuration of a hemicylinder in the two-dimensional (2D) condition and a hemisphere in the axisymmetric (AS) condition. Similarly, Figure 2.1b presents the configuration of a cylinder or a sphere. The cylindrical and spherical conductors have radius R. Figure 2.1c shows the AS configuration of a hemispheroid with major semi-axis c and minor semi-axis b. The conductors are subject to external electric field $\mathbf{E_0}$. The background medium surrounding the conductor has permittivity ε_E (= ε_0 for vacuum or a gaseous dielectric).

(a) Hemicylinder or hemisphere   (b) Cylinder or sphere   (c) Hemispheroid
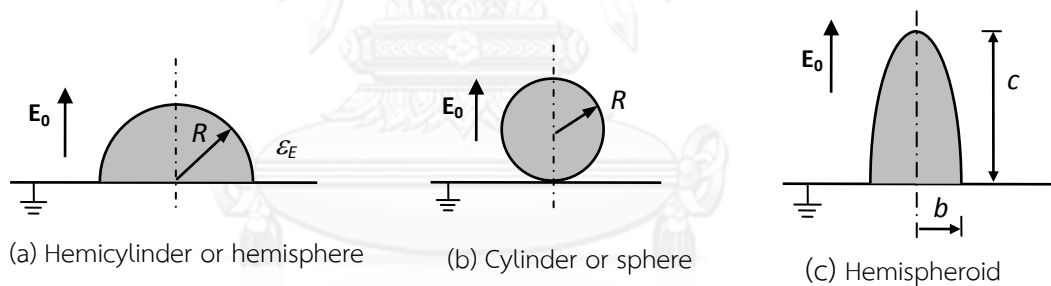
Figure 2.1. Configurations of a conductor in contact with a grounded plane under electric field.

The presence of the conductor distorts the electric field from $\mathbf{E_0}$. The field is highly intensified near the tip (the top pole) of the conductor. Under the external electric field, the conductor acquires charge Q from the plane. The interaction between Q and the electric field results in the Coulomb force F_e (the electrostatic force) on the conductor. This force tends to elevate the conductor from the plane, irrespective of the direction of the external field. The charge and force vary proportionally to the surface area of the conductor.

For the configurations in Figure 2.1a and 2.1c, the electric field can be simply obtained in the cylindrical, spherical, or prolate spheroidal coordinates by applying

the theory of images. The charge and force can be then calculated from the obtained values of the electric field. For the configuration in Figure 2.1b, Felici applies the classical image method which uses point and dipole charges (zero and first-order multipoles) to satisfy the boundary conditions on the grounded plane and the conductor surface. The electric field and force can be then determined from the charges. The following sections present the analytical solutions in a closed form for the configurations in Figure 2.1.

2.1.1 Hemicylinder or cylinder

For the 2D configurations, the charge and force are presented per unit length. For the configuration of a hemicylinder on a grounded plane, the expressions of the maximal field E_{max}, the induced charge Q, and the Coulomb force are [23]

$$E_{max} = 2E_0, \tag{2.1a}$$

$$Q = 4\varepsilon_E RE_0, \tag{2.1b}$$

$$F_e = \frac{8}{3}\varepsilon_E RE_0^2 = \frac{2}{3}QE_0 \tag{2.1c}$$

For the configuration of a cylinder on a grounded plane [23],

$$E_{max} = \frac{\pi^2}{4}E_0, \tag{2.2a}$$

$$Q = 2\pi\varepsilon_E RE_0, \tag{2.2b}$$

$$F_e = \left(\frac{\pi^2}{9} + \frac{1}{3}\right)\pi\varepsilon_E RE_0^2 \approx 1.43\pi\varepsilon_E RE_0^2 = 0.715QE_0. \tag{2.2c}$$

2.1.2 Hemisphere or sphere

For the configuration of a hemisphere on a grounded plane [23],

$$E_{max} = 3E_0, \tag{2.3a}$$

$$Q = 3\pi\varepsilon_E R^2 E_0, \tag{2.3b}$$

$$F_e = \frac{9}{4}\pi\varepsilon_E R^2 E_0^2 = 0.75QE_0. \tag{2.3c}$$

For the configuration of a sphere on a grounded plane [23],

$$E_{max} = \frac{7}{2}\zeta(3)E_0 \approx 4.208E_0, \tag{2.4a}$$

$$Q = \frac{2}{3}\pi^3\varepsilon_E R^2 E_0, \tag{2.4b}$$

$$F_e = \left(\zeta(3) + \frac{1}{6}\right)\left(4\pi\varepsilon_E R^2\right)E_0^2 \approx 0.832 Q E_0, \tag{2.4c}$$

where ζ is the Riemann zeta function defined as [46]

$$\zeta(x) = \sum_{n=1}^{\infty} \frac{1}{n^x}. \tag{2.5}$$

In term of the surface area $S = 4\pi R^2$, we may write $Q \approx 1.645\varepsilon_E S E_0$ and $F_e \approx 1.369\varepsilon_E S E_0^2$.

2.1.3 Hemispheroid

For the configuration of a hemispheroid on a grounded plane, the maximal field at the hemispheroid tip is [47]

$$E_{max} = \frac{E_0}{\left[\eta_0 \operatorname{arccoth}(\eta_0) - 1\right]\left[\eta_0^2 - 1\right]}, \tag{2.6}$$

where $\eta_0 = \dfrac{c}{\sqrt{c^2 - b^2}}$. \hfill (2.7)

For this configuration, Felici [23] gave approximate formulae to estimate the charge and force on the hemispheroid for $b \ll c$,

$$Q \approx \frac{\pi\varepsilon_E c^2 E_0}{\ln\left[\dfrac{2c}{b}\right] - 1}, \tag{2.8a}$$

$$F_e \approx \frac{\pi\varepsilon_E E_0^2 c^2 \left[\ln\left(\dfrac{c}{b}\right) - 0.5\right]}{\left[\ln\left(\dfrac{2c}{b}\right) - 1\right]^2}. \tag{2.8b}$$

Recently, K. Zhou and S. Boggs [48, 49] derived exact formulae for the charge and force on the hemispheroid. They are

$$Q = \frac{\pi\varepsilon_E (c^2 - b^2) E_0}{\eta_0 \operatorname{arccoth}(\eta_0) - 1}, \tag{2.9a}$$

$$F_e = \frac{\pi\varepsilon_E E_0^2 (c^2 - b^2)\left[\ln\left(\dfrac{c}{b}\right) - \dfrac{1}{2\eta_0^2}\right]}{\left[\operatorname{arccoth}(\eta_0) - \dfrac{1}{\eta_0}\right]^2}. \tag{2.9b}$$

Figure 2.2 shows the variation of the charge and force in equations (2.8) and (2.9) with the axis ratio c/b from 2 to 10. The charge and force are normalized by $\varepsilon_E S E_0$

and $\varepsilon_E SE_0^2$, where S is the surface area of the hemispheroid, respectively. We can see from the figure that the approximate values in equation (2.8) are greater than the exact ones in equation (2.9) when $c/b \geq 2$. The difference reduces with increasing in c/b. Note that the difference is smaller 10% as $c/b \geq 5$.

(a) Induced charge (b) Electrostatic force
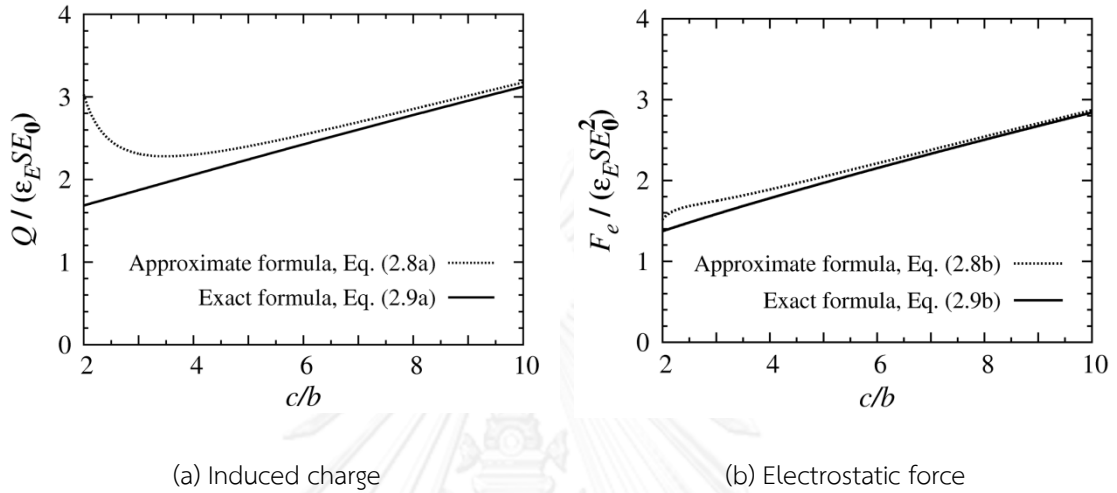
Figure. 2.2. Induced charge and electrostatic force on the hemispheroid.

2.2 Lifting electric field of spherical and wire particles

Let consider a conducting particle lying on an electrode under electric field. If the electrostatic force F_e overcomes the gravitational force F_g, the particle is lifted from the electrode. F_e depends on the magnitude of external field and the geometrical parameters of the particle whereas F_g is a function of material and volume of the particle. Thus, for a specific particle, we can determine the strength of external field which lift the particle from the condition

$$F_e = F_g .$$
(2.10)

This field strength is referred as the lifting electric field E_L.

2.2.1 Spherical particles

Consider a conducting spherical particle with radius R located on an electrode under electric field in a gaseous medium. The gravitational force of the particle is

$$F_g = \frac{4}{3}\pi R^3 \rho g ,$$
(2.11)

where ρ denotes the mass density of the particle, and g is the gravitational acceleration. The electrostatic force on the particle is determined by using equation (2.4c), where $\varepsilon_E = \varepsilon_0$. Therefore, the lifting field E_L can be determined as

$$E_L = \sqrt{\frac{g\rho R}{3 \times 1.369\varepsilon_0}} \approx 5.19 \times 10^5 \sqrt{\rho R} \, . \qquad (2.12)$$

The relevant quantities in equation (2.12) are in SI unit. The equation indicates that E_L varies as a function of square root of mass density and radius of the particle.

We consider aluminum, stainless steel, and copper, which have mass density of about 2700, 7850, 8960 kg/m^3, respectively, as materials of the particle. They represent three typical materials of metallic particles in gas insulated systems. Figure 2.3 presents the lifting field for the particles with radius varied from 0.01 to 1 mm on logarithmic scale. It is clear from the figure that the field strength of 5 kV/cm can lift the particles having radius smaller than 0.1 mm from the electrode.
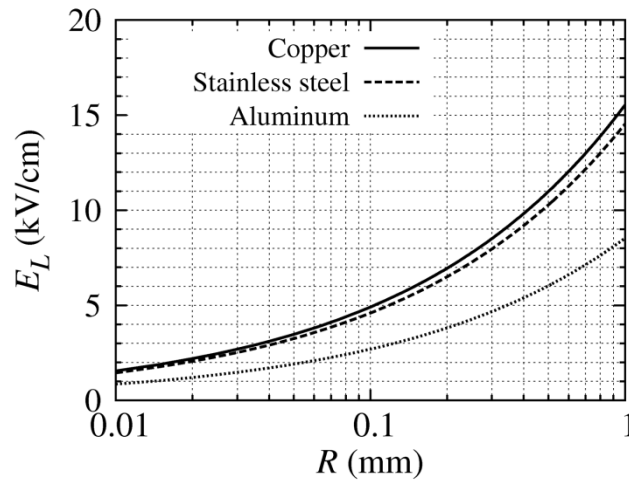
Figure 2.3. Lifting field of spherical particles as a function of the particle radius.

2.2.2 Wire particles

Consider a wire particle with radius R and length L on the electrode. The gravitational force of the wire particle is

$$F_g = \pi R^2 L \rho g \, . \qquad (2.13)$$

As the electrostatic force on the particle depends on its orientation with the electrode, two basic orientations are treated. First, when the particle lies horizontally on the electrode, the electrostatic force is estimated by using the model of an infinite cylinder in equation (2.2c) [50],

$$(F_e)_{ly} = 1.43\pi\varepsilon_0 R L E_0^2 \, . \qquad (2.14)$$

Second, when the particle stands vertically on the electrode, the model of a hemispheroid with the approximate solution in equation (2.8b) is applied to evaluate the force on the particle [50]. That is,

$$(F_e)_{stand} = \frac{\pi \varepsilon_0 E_0^2 L^2 \left[\ln\left(\dfrac{L}{R}\right) - 0.5 \right]}{\left[\ln\left(\dfrac{2L}{R}\right) - 1 \right]^2} .$$ (2.15)

Therefore, the lifting field corresponding to the two described orientations can be calculated as

$$(E_L)_{ly} = \sqrt{\frac{g\rho R}{1.43\varepsilon_0}} \approx 8.8 \times 10^5 \sqrt{\rho R} ,$$ (2.16a)

$$(E_L)_{stand} = \left[\ln\left(\frac{2L}{R}\right) - 1 \right] \sqrt{\frac{g\rho R^2}{\varepsilon_0 L \left[\ln\left(\dfrac{L}{R}\right) - 0.5 \right]}} .$$ (2.16b)

Equation (2.16a) implies that $(E_L)_{ly}$ varies as a function of $\sqrt{R}$, similar to the case of the spherical particles. The $\sqrt{R}$ relationship does not hold for $(E_L)_{stand}$ in equation (2.16b). Note that $(E_L)_{ly}$ is independent of the particle length. The lifting field in (2.16) is directly proportional to the square root of mass density. As an example, Figure 2.4 presents the values of $(E_L)_{ly}$ and $(E_L)_{stand}$ for aluminum particles. The particles have radius in range from 0.01 to 1 mm, and length of 2 and 4 mm. The dotted line in Figure 2.4 represents the lifting field of spherical particles for comparison. It can be seen from the figure that $(E_L)_{stand}$ is always smaller than $(E_L)_{ly}$, i.e., $(F_e)_{stand} > (F_e)_{ly}$. $(E_L)_{stand}$ increases with increasing in radius but with decreasing in length. However, the effect of the radius is more dominant in comparison with that of the length.
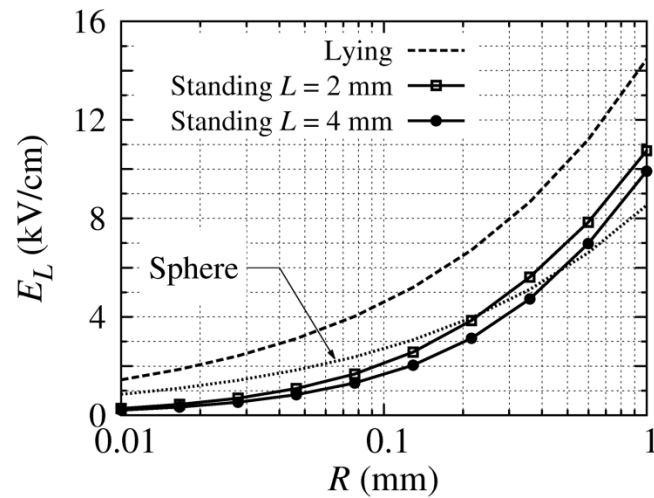
Figure 2.4. Lifting field for lying and standing aluminum wire particles with different lengths.

Theoretically, a wire particle lying on an electrode will be departed from the electrode in the horizontal orientation when $(F_e)_{ly} > F_g$. However, due to the difference of ending profiles of a wire particle, the stresses at two ends are not homogeneous. Therefore, either end of the particle may raise first. For this respect, Higashiyama et al. [22] observed the initial movement of wire particles with different ending shapes. That is, one end was cut perpendicularly, whereas the other end might be in conical or angle-cut shape. The particles were cut from copper wires having 0.1 and 0.25 mm in diameter. The length of the particles varied in a range from 1 to 4 mm. For the angle-cut particles, the authors changed their initial placement condition on the electrode to make different field strength at the particle ends. The results from observation are shown in Figure 2.5. We can see from the figure that the particles usually moved initially at a sharper end. They believed that the shaper end generally experienced a stronger lifting force than the other end.
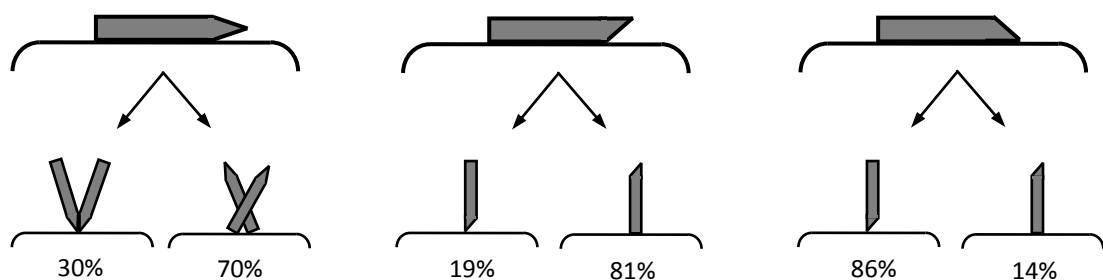
Figure 2.5. Probability of initial stand-up from different lying conditions [22].

For the lifting electric field, the authors compared the experimental results with theoretical values estimated by equation (2.16a) for a lying wire particle. The comparison indicated that the experimental values were always greater than theoretical ones. The difference was about 6% and 40% for the particles having 0.25-mm and 0.1-mm diameters, respectively.

2.3 Characteristics of corona discharge

Corona discharge is generally an electrical discharge phenomenon in a gaseous medium at a nonuniform electric field region [51-53]. The corona discharge occurs when the field strength in the region is higher than the critical field for collisional ionization of the gaseous medium, but not high enough to cause a complete breakdown or an electric arc to nearby objects. It is usually observed at conductors having small radius of curvature such as long power transmission lines, protrusions on electrode surface, or floating metallic filamentary wires. The corona discharge belongs to the general class of the glow discharge. Corona discharge is used in many various applications, however, it has unwanted effects on electric power systems. For example, power losses, audible and radio-frequency noises near transmission lines, and insulation damages of gas insulated apparatuses may result from corona discharge.

The volume involved in a corona discharge can be generally subdivided into an ionization region and drift regions. The former relates to the high electric field region around a conductor, which is known as a discharge electrode [54] or an active electrode [55]. The latter is the lower electric field regions between the former and nearby objects. Figure 2.6 shows the volume of the corona discharge of a typical point-to-plane geometry. In the ionization region, the initial free electrons, produced generally by ultraviolet radiations and cosmic rays, obtain high kinetic energy by the high electric field. The energy is strong enough to ionize neutral atoms and molecules of gaseous medium by collision, which results in new electrons and positive ions. The new electrons are then accelerated and collide with other neutral particles to generate further electron and positive ions. The repetitive ionization process forms electron and ion avalanches. Charged particles in this region move towards electrodes and are neutralized at the electrodes. In the drift regions, due to the low electric field the collisional ionization does not occur.
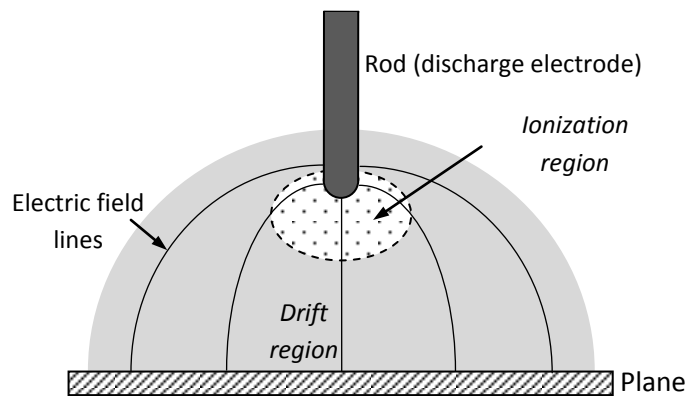
Figure 2.6. Ionization and drift regions of a typical point-to-plane corona discharge.

The characteristic of corona current is dependent on movement of ions produced in the ionization region through the drift region. The corona discharge is also associated with glows (light emission) and sounds. We can detect the corona discharge from current pulses by using current transformers or detecting resistors, light pulses by using photomultipliers, sound by applying ultrasonic detectors, or electromagnetic noise.

Corona discharge is usually classified according to its polarity, positive or negative. The polarity is referred to that of the charge on the discharge electrode. The characteristics of the positive and negative corona discharges are significantly different from each other because of the unequal mobilities of the electron and positive ions. The mobilities lead to different space-charge and field distribution, as to be explained in the following sections.

2.3.1 Positive corona

For the positive corona discharge, the electrons produced in the ionization region move towards the discharge electrode and form electron avalanches, as shown in Figure 2.7a. By contrast, the positive ions move away from the discharge electrode. Due to their high mobility, the electrons rapidly approach the electrode and are neutralized here. Thus, positive-ion clouds are formed in front of the electrode, and move slowly towards the drift region, as illustrated in Figure 2.7b. The electric field E_+ produced by the positive ions reduces the electric field in the discharge-electrode side and increases the field in the opposite side. Therefore, the ionization process in front of the discharge electrode is weakened by the positive ion clouds. This causes the difficulty for positive corona inception.

In general, when the voltage applied to the discharge electrode exceeds a critical (onset) value, the positive corona discharge starts burst pulses. With increasing the voltage, there is a transition of the burst pulses to onset streamer, glow corona, and finally to spark discharge [56, 57].

2.3.2 Negative corona

For the negative corona discharge, the electrons move away from the discharge electrode, forming electron avalanches with the head towards the nearby electrodes, as shown in Figure 2.8a. The electrons rapidly leave the ionization region. The electrons may attach to molecules to form negative ions in the drift region or drift to the nearby electrodes and are neutralized there. On the other hand, the positive ions in the ionization region move towards the discharge electrode. Because of their low mobility, positive-ion clouds having high density are formed in front of the discharge electrode (see Figure 2.8b). These ions distort considerably electric field. The electric field between the positive-ion and electron clouds decreases significantly, resulting in the restriction of the ionization region. By contrast, the electric field near the discharge electrode increases, enhancing ion generation by collision. This creates favourable conditions for the inception of the negative corona. Therefore, in the same electrode configuration the inception voltage is lower for the negative corona than for the positive corona.

The current waveform of the negative corona is a series of Trichel pulses, characterized by very short rise times (as short as 1.3 ns [58]), short durations (tens of ns [59]), and separated by much longer inter-pulse periods (tens of μs [59]). The first pulse in the series is always greater than that of subsequent pulses [54, 60]. The time interval between the first two pulses is usually longer than that between other pulses in the steady state. The characteristics of the Trichel pulses are very regular in oxygen and air but irregular in other electronegative gases (attaching) such as SF_6. P. Sattari et al. [54] carried out experimental and numerical studies on negative corona discharge of point-to-plane configuration in air under various conditions. The results show that the average value of corona current does not much depend on external resistance. The period of Trichel pulses decreases with increasing the applied voltage magnitude. The Trichel pulse corona changes to the continuous negative glow corona and finally to spark discharge when the applied voltage increases [56].

(a) Electron avalanches   (b) Positive-ion clouds
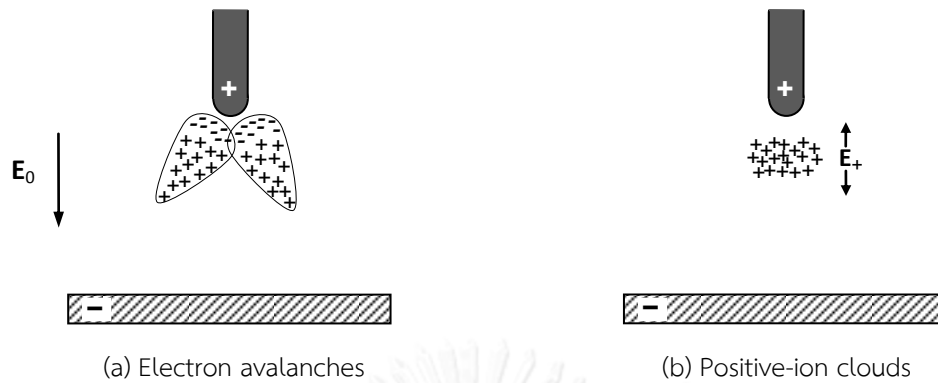
Figure 2.7. Mechanism of positive corona.

(a) Electron avalanches   (b) Positive-ion and electron clouds
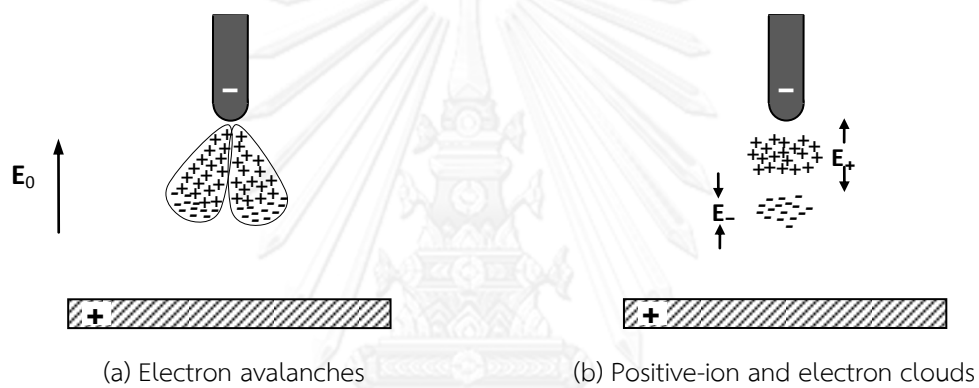
Figure 2.8. Mechanism of negative corona.

2.4 Corona discharge in the presence of elongated particles

Conducting particles in gas insulated systems are small and have irregular shapes. They are major sources producing corona discharge in the systems as the electric field significantly enhances around the particles, especially near their ends. To investigate experimentally the characteristics of corona discharge in the presence of the particles, the configuration of a conducting elongated particle located within parallel-plate electrodes has been usually used. The lower electrode is grounded while the other is connected to high voltage. The particle may be a wire particle or a prolate spheroidal one. The particle is placed parallel to the electric field with various positions in the electrode gap. The corona discharge on the particle is observed under the condition that the applied voltage increases gradually or is fixed.

When the particle is in contact with an electrode in Figure 2.9, it acts as a protrusion of the electrode. Thus, at the upper end of the particle in Figure 2.9, the negative corona occurs under positive voltage application and vice versa. For a

floating particle between two electrodes, as shown in Figure 2.10, the particle is polarized under the external field. Positive and negative charges are induced on the tip facing the cathode and the anode, respectively. Thus, bipolar corona discharges may take place on the particle.

(a) Positive   (b) Negative

Figure 2.9. Monopolar corona discharge on particles in contact with the lower electrode for different voltage polarities applied to the upper electrode.

(a) Positive   (b) Negative
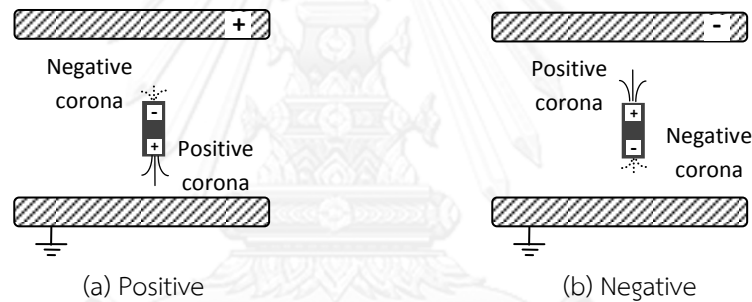
Figure 2.10. Bipolar corona discharge on floating particles between electrodes for different applied voltage polarities.

2.4.1 Corona current and inception voltage

Higashiyama's group [14] observed corona discharge on a copper wire particle under the positive DC voltage in atmospheric air. The wire particle had 0.25 mm in diameter and 6 mm in length. Both ends were rounded to hemisphere. The particle was separated from the lower electrode by distance δ in an electrode gap of 20 mm. When δ = 0 and 14 mm, the particle was in contact with the lower and upper electrodes, respectively. The experimental results of the magnitude of corona current flowing through the lower electrode and the corona inception voltage for different distances δ are shown in Figure 2.11.
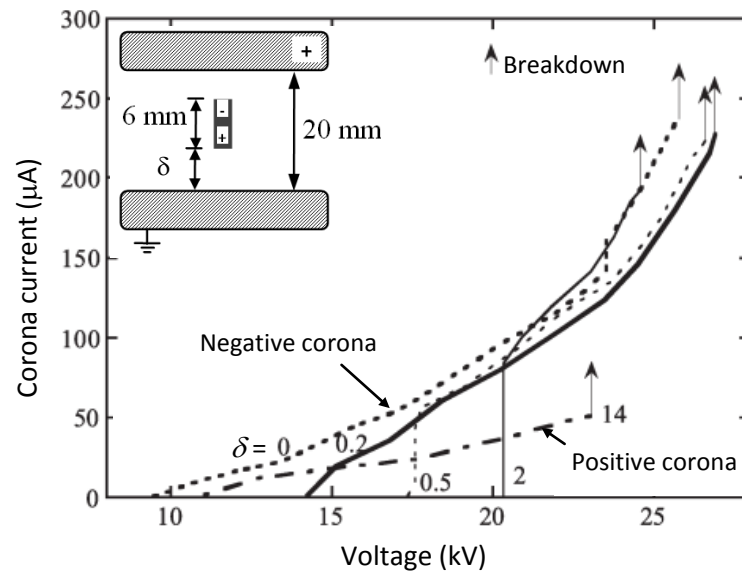
(a) Corona current versus applied voltage.
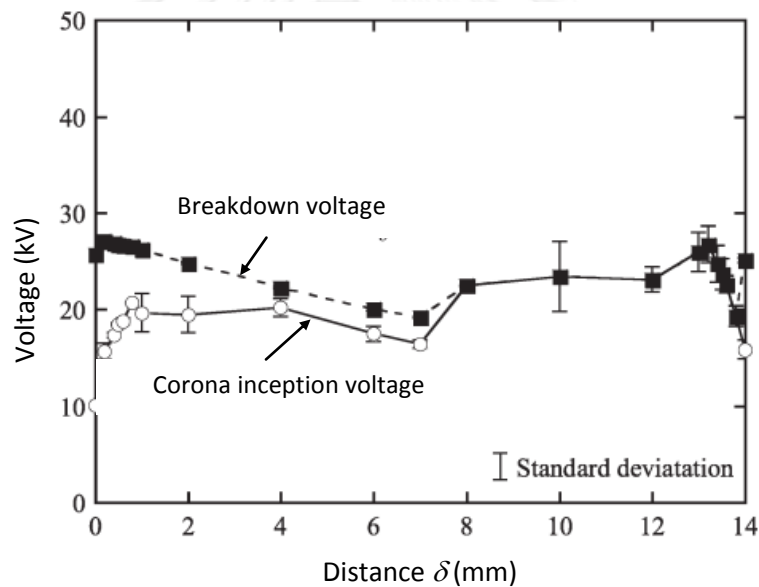
(b) Corona inception and breakdown voltage.

Figure 2.11. Corona discharge of a copper wire having 6 mm in length and 0.25 mm in diameter for different distances δ between the particle and lower electrode[14].

As shown in Figure 2.11a, the corona inception voltage was lower when δ = 0 (negative corona) than when δ = 14 mm (positive corona). The corona current increased gradually after the corona onset. The negative corona current (δ = 0) was much greater than positive one (δ = 14 mm) at the same voltage. When δ = 0.2, 0.5, and 2 mm, the corona current increased suddenly at the corona onset. This was a result of the superposition of the Trichel pulses and positive streamer pulses

occurring simultaneously at both ends. For Figure 2.11b, when the particle was closer to the lower electrode (or the cathode electrode), the corona inception voltage increased considerably with δ. When the particle was closer to but not in contact with the anode (8 mm < δ < 14 mm), the stable corona never occurred. Instead, a complete breakdown through the particle took place without the corona. This means that a particle near a positive electrode can promote a spark discharge or breakdown between electrodes.

2.4.2 Corona discharge mechanism

Hara et al. [15] investigated experimentally the corona discharge on aluminum elongated particles under a 60 Hz AC voltage in atmospheric air. Two kinds of the particles were used in the experiment. The first was a particle of 10 mm in length with an end in conical profile and other end in hemispherical profile. The radius of the conical and hemispherical ends was 0.1 mm and 0.5 mm, respectively. The second was prolate spheroidal particles having the same major-to-minor axis ratio of 10. The spheroidal particles had the major axis varied in the range from 5 mm to 12 mm. The particles were placed parallel to the electric field in the experiment. For the conical-hemispherical particle, the conical tip was set to be faced the grounded electrode. The authors observed the pulses of the corona current and light emission for various values of the distance δ and the applied voltage in an electrode gap of 45 mm. From the observation, the authors classified the mechanism of the corona discharge on the particles under the floating condition into three types.

For the conical-hemispherical particle, when the applied voltage was near the corona inception voltage, corona discharges occurred only at the conical tip. In each half cycle, only positive corona or negative corona appeared when the polarity of the conical tip became the positive or negative, respectively. Therefore, for each full cycle of the applied voltage, the charge on the particle was neutralized. This discharge mechanism was referred as Mechanism I. When the applied voltage increased, in the positive half cycle, the positive corona developed at the conical tip while the negative corona took place simultaneously at the hemispherical tip. Hence, the resultant current waveform was a superposition of the positive streamer pluses and the Trichel pulses. On the other hand, in the negative half cycle, only the negative corona occurred at the conical tip. In this case, the discharge mechanism was referred as Mechanism II. When the applied voltage further increased, the positive and negative corona discharges appeared simultaneously at both tips in both half cycles of the applied voltage, referred as Mechanism III.

For the prolate spheroidal particles, the simultaneous existence of positive and negative corona discharges at both ends was always observed in both half cycles of the applied voltage when the corona discharge appeared. This was known as the Mechanism III.

Figure 2.12 presents the corona discharge mechanism of the particles for different δ distances. For the conical-hemispherical particle in Figure 2.12a, the Mechanism I seemed to be dominant when the particle was near the grounded electrode. The Mechanism III is dominant when the particle at the middle of the electrode gap for both particle types.
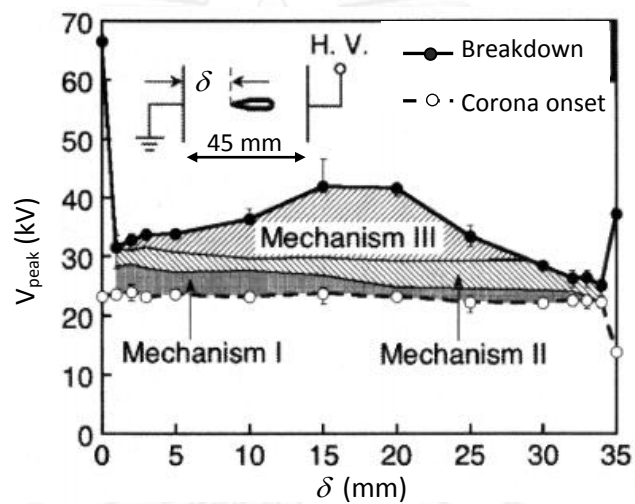
(a) Conical-hemispherical particle
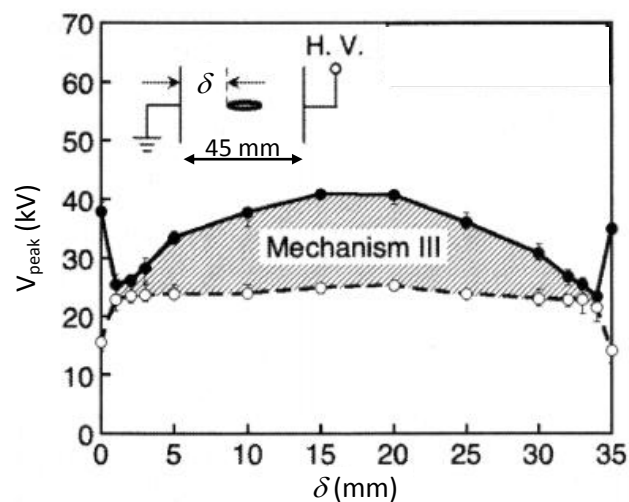
(b) Prolate spheroidal particle

Figure 2.12. Corona discharge mechanism of conical-hemispherical and prolate spheroidal particles with the length of 10 mm [15].

To understand the particle-initiated corona mechanism in the interference of monopolar corona discharges at both tips of the particles, the authors evaluated quantitatively the electric field change due to the flow of space charges into the particles. They used only the prolate spheroidal particle for the evaluation. The electric field E_x along the major axis of the particle with charge Q_i under external field $\mathbf{E_0}$, as shown in Figure 2.13, was given by following expression [15],

$$E_x = E_{\rho 0} + E_{\rho i}, \tag{2.17}$$

where

$$E_{\rho 0} = E_0 \left[1 - \frac{\tanh^{-1}\sqrt{\dfrac{c^2-b^2}{x^2}} - \sqrt{\dfrac{c^2-b^2}{x^2}}\left\{\dfrac{x^2}{x^2-(c^2-b^2)}\right\}}{\tanh^{-1}\sqrt{\dfrac{c^2-b^2}{x^2}} - \sqrt{\dfrac{c^2-b^2}{x^2}}} \right], \tag{2.18}$$

$$E_{\rho i} = \frac{Q_i}{4\pi\varepsilon_E (x^2 - c^2 + b^2)}. \tag{2.19}$$

$E_{\rho 0}$ was the electric field when $Q_i = 0$, $E_{\rho i}$ was the electric field component produced by Q_i, and x was the distance along the major axis defined in Figure 2.13. Q_i represented the charge amount of the electron flow produced by the positive corona or that of the positive-ion flow produced by the negative corona into the particle. Q_i was estimated by integrating the corona current pulses.
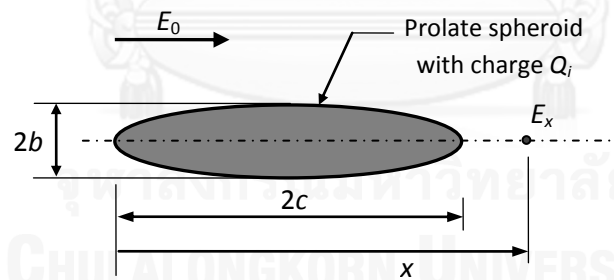
Figure 2.13. Charged prolate spheroidal particle parallel to the external field $\mathbf{E_0}$.

It was found from the field evaluation that the positive corona occurring at a positive end increased significantly the electric field at the other negative end. This might trigger a negative corona there. On the other hand, the increase of the electric field by the negative corona was rather insignificant. Therefore, the consecutive occurrence of many negative corona discharges might be necessary to neutralize the electrons produced by the positive corona in the particle.

CHAPTER III

ANALYTICAL METHOD FOR PROLATE SPHEROIDAL PARTICLES

This chapter presents a three-dimensional configuration of a conducting or dielectric prolate spheroid under external electric field and calculation method for the analysis of this dissertation. In the configuration, the spheroid is in contact with or separated from a grounded plane. The method of multipole images and the multipole re-expansion for the prolate spheroidal coordinates are applied to the electric field calculation. The induce charge, electrostatic force, and electrostatic torque on the spheroid are then determined from the calculated field. For the special case in which the configuration is axisymmetric about the major axis of the spheroid, the formulae of the re-expansion coefficient and the force can be derived directly from the multipole images and are expressed in a closed form.

3.1 Prolate spheroidal coordinates

Prolate spheroidal coordinates (η, ξ, φ) are a three-dimensional orthogonal coordinate system that results from rotating the elliptic coordinates about the major (longer) axis of the ellipses, as shown in Figure 3.1. With the focal points of ellipses located at $\pm a$ on the z-axis, the relationship between the prolate spheroidal coordinates and the Cartesian coordinates (x, y, z) is expressed as follows:

$$x = a\sqrt{\eta^2 - 1}\sqrt{1 - \xi^2}\cos\varphi$$
$$y = a\sqrt{\eta^2 - 1}\sqrt{1 - \xi^2}\sin\varphi \,, \qquad (3.1)$$
$$z = a\eta\xi$$

where $\eta \geq 1$, $-1 \leq \xi \leq 1$, $0 \leq \varphi < 2\pi$. When a approaches 0, the spheroidal coordinates becomes the spherical ones. In the spheroidal coordinates, η = constant corresponds to the surface of a prolate spheroid whose major semi-axis c and minor semi-axis b are equal to $a\eta$ and $a\sqrt{\eta^2 - 1}$, respectively. The surface of this spheroid is expressed in the Cartesian coordinates by

$$\frac{x^2 + y^2}{b^2} + \frac{z^2}{c^2} = 1 \,, \qquad (3.2)$$

where $c^2 - b^2 = a^2$.

The scale factors (metric coefficients) in the spheroidal coordinates can be calculated from (3.1) as [47]

$$h_\eta = a\sqrt{\frac{\eta^2 - \xi^2}{\eta^2 - 1}} \;,\quad h_\xi = a\sqrt{\frac{\eta^2 - \xi^2}{1 - \xi^2}} \;,\quad h_\varphi = a\sqrt{(\eta^2 - 1)(1 - \xi^2)} \;, \tag{3.3}$$

where the subscripts indicate the coordinates. The unit vectors are [61]

$$\mathbf{a}_\eta = \eta\sqrt{\frac{1 - \xi^2}{\eta^2 - \xi^2}}\cos\varphi\,\mathbf{a}_x + \eta\sqrt{\frac{1 - \xi^2}{\eta^2 - \xi^2}}\sin\varphi\,\mathbf{a}_y + \xi\sqrt{\frac{\eta^2 - 1}{\eta^2 - \xi^2}}\mathbf{a}_z, \tag{3.4a}$$

$$\mathbf{a}_\xi = -\xi\sqrt{\frac{\eta^2 - 1}{\eta^2 - \xi^2}}\cos\varphi\,\mathbf{a}_x - \xi\sqrt{\frac{\eta^2 - 1}{\eta^2 - \xi^2}}\sin\varphi\,\mathbf{a}_y + \eta\sqrt{\frac{1 - \xi^2}{\eta^2 - \xi^2}}\mathbf{a}_z, \tag{3.4b}$$

$$\mathbf{a}_\varphi = -\sin\varphi\,\mathbf{a}_x + \cos\varphi\,\mathbf{a}_y. \tag{3.4c}$$

In addition, the gradient operator ∇ and Laplacian ∇^2 can be written as [62]

$$\nabla = \frac{1}{a}\left[\mathbf{a}_\eta\sqrt{\frac{\eta^2 - 1}{\eta^2 - \xi^2}}\frac{\partial}{\partial\eta} + \mathbf{a}_\xi\sqrt{\frac{1 - \xi^2}{\eta^2 - \xi^2}}\frac{\partial}{\partial\xi} + \mathbf{a}_\varphi\sqrt{\frac{1}{(\eta^2 - 1)(1 - \xi^2)}}\frac{\partial}{\partial\varphi}\right], \tag{3.5}$$

$$\nabla^2 = \frac{1}{a^2(\eta^2 - \xi^2)}\left[\frac{\partial}{\partial\eta}\left\{(\eta^2 - 1)\frac{\partial}{\partial\eta}\right\} + \frac{\partial}{\partial\xi}\left\{(1 - \xi^2)\frac{\partial}{\partial\xi}\right\} + \frac{\eta^2 - \xi^2}{(\eta^2 - 1)(1 - \xi^2)}\frac{\partial^2}{\partial\varphi^2}\right]. \tag{3.6}$$

(a) Planes of constant η, ξ, and φ (b) Variation of η and ξ
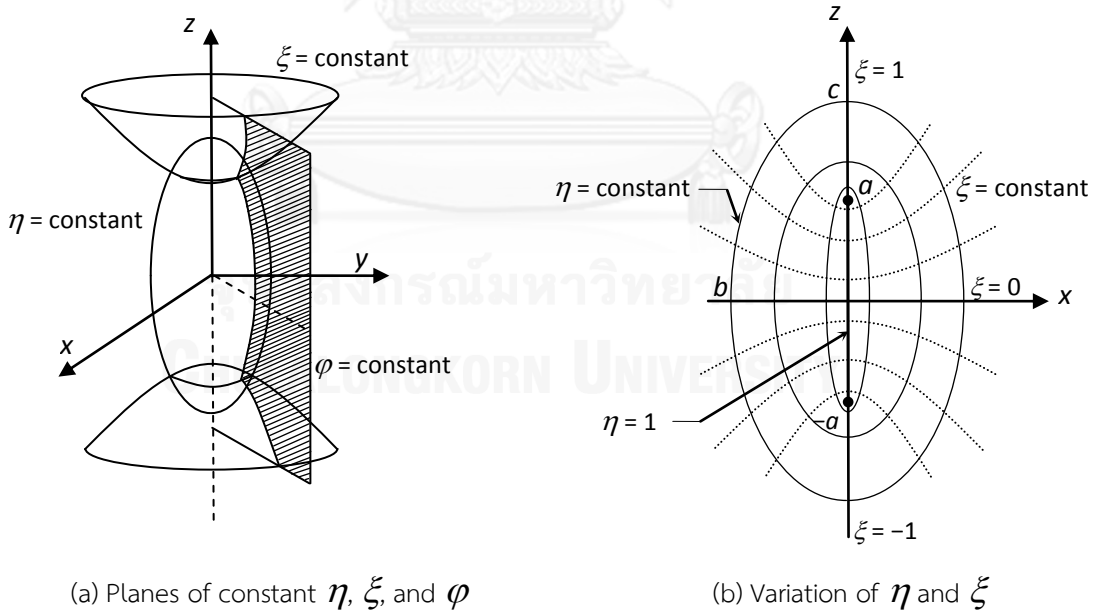
Figure 3.1. Prolate spheroidal coordinates.

3.2 Configuration of analysis

Figure 3.2a shows a three-dimensional configuration of a prolate spheroid for the analysis. The configuration is a conducting or dielectric prolate spheroid centered at **o** above a grounded plane under external electric field **E$_0$**. The major axis of spheroid makes tilt angle α with the grounded plane. When α = 90°, the configuration is geometrically symmetric about the major axis, as shown in Figure 3.2b. The separation between the lowest point **p** on the spheroid surface and the grounded plane is defined as δ. That means that when δ = 0 the spheroid is in contact with the plane at **p**. For a conducting spheroid, it is at a grounded potential when δ = 0 and electrically floating when δ > 0. Both uncharged and charged conditions are considered for the electrically floating spheroid. For a dielectric spheroid with permittivity ε_S, an uncharged condition is applied.
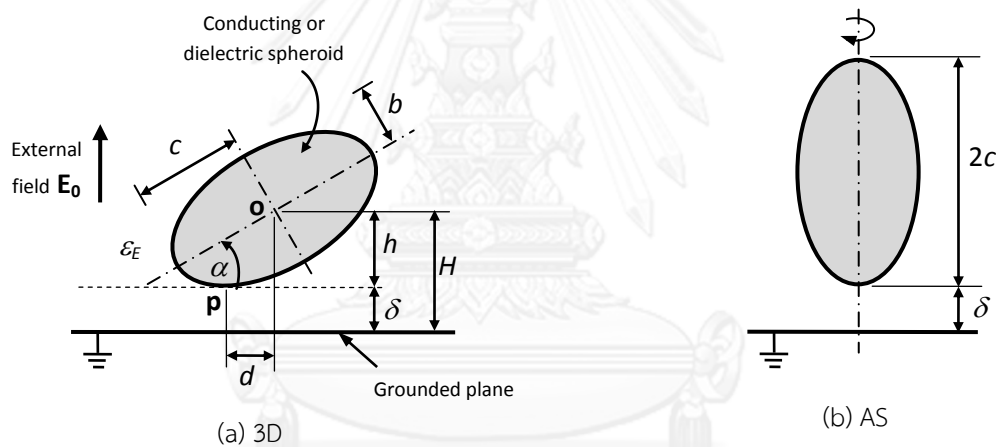
Figure 3.2. Conducting or dielectric prolate spheroid above a grounded plane under external electric field **E$_0$**.

The surface area *S* and the volume *V* of the spheroid are determined by [63]

$$S = 2\pi b^2 \left[1 + \frac{c}{b} \frac{\arccos(b/c)}{\sqrt{1-(b/c)^2}} \right],$$ (3.7)

$$V = \frac{4}{3}\pi c b^2 .$$ (3.8)

For the configurations in Figure 3.2, the electric field on the spheroid is independent of *b* and *c* values, provided the axis ratio *c/b* and the ratio δ/c are constant. By contrast, the induced charge, electrostatic force, and electrostatic torque vary

proportionally to the surface area and the volume, respectively, for the same ratio c/b.

The horizontal distance d and vertical distance h between the lowest point **p** and the center **o** are a function of b, c, and α as follows:

$$d = \frac{(c^2 - b^2)\sin\alpha}{\sqrt{b^2 + c^2 \tan^2 \alpha}},$$
(3.9)

$$h = \sqrt{b^2 + c^2 \tan^2 \alpha}\cos\alpha.$$
(3.10)

Two Cartesian coordinates having the origin at **o** shown in Figure 3.3a are used for the calculation. First, (X, Y, Z) are the global coordinates where the external field is in the $+Z$ direction. Next, (x, y, z) are the local coordinates in which the z axis is the major axis of the spheroid. (x, y, z) are obtained by rotating (X, Y, Z) about the Y (or y) axis by 90°−α. That is,

$$\begin{bmatrix} X \\ Y \\ Z \end{bmatrix} = \begin{bmatrix} \sin\alpha & 0 & \cos\alpha \\ 0 & 1 & 0 \\ -\cos\alpha & 0 & \sin\alpha \end{bmatrix}\begin{bmatrix} x \\ y \\ z \end{bmatrix}.$$
(3.11)

Prolate spheroidal coordinates (η, ξ, φ) are applied to (x, y, z) to present the spheroid surface where $\eta = \eta_0$ (=c/a), as shown in Figure 3.3b.

(a) Cartesian coordinates   (b) Prolate spheroidal coordinates
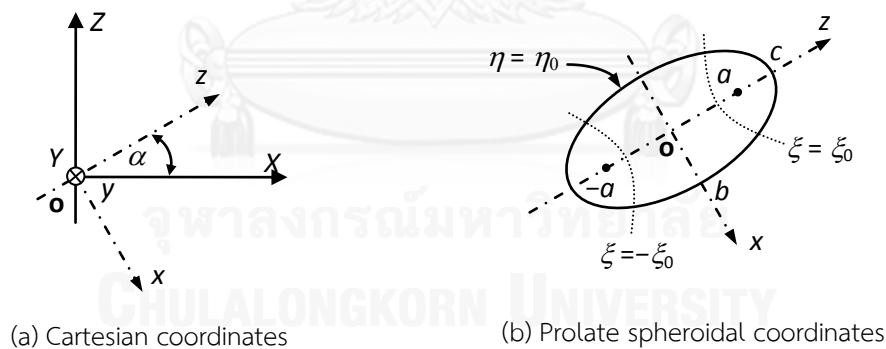
Figure 3.3. Coordinates used for the calculation.

3.3 Potential harmonics

General harmonic solutions to the Laplace equation in the prolate spheroidal coordinates are a sum of prolate spheroidal harmonics. For a spheroid whose surface is defined by $\eta = \eta_0$, we can express potential ψ_{ext} produced by any charges outside the spheroid in the form of local expansion as

$$\psi_{ext} = \sum_{n=0}^{\infty}\sum_{m=0}^{n} P_{n,m}(\eta)P_{n,m}(\xi)\left[L_{n,m}^{c}\cos m\varphi + L_{n,m}^{s}\sin m\varphi\right], \qquad (3.12)$$

where $P_{n,m}$ is the associated Legendre function of the first kind of order n and degree m. $L_{n,m}^{c}$ and $L_{n,m}^{s}$ are real-number potential coefficients. The potential ψ_{ext} induces charges on the spheroid surface. The induced potential ψ_{ind} due to these charges can be expressed in the form of multipole expansion,

$$\psi_{ind} = \sum_{n=0}^{\infty}\sum_{m=0}^{n} Q_{n,m}(\eta)P_{n,m}(\xi)\left[B_{n,m}^{c}\cos m\varphi + B_{n,m}^{s}\sin m\varphi\right], \qquad (3.13)$$

where $Q_{n,m}$ is the associated Legendre function of the second kind of order n and degree m. Note that $Q_{n,m}(\eta)$ vanishes as $\eta \to \infty$. Therefore, the resultant potential in the exterior of the spheroid ($\eta \geq \eta_0$) is

$$\psi = \psi_{ext} + \psi_{ind}. \qquad (3.14)$$

For the configuration in Figure 3.2, the field is symmetric with respect to the plane φ = 0°. Hence, all $L_{n,m}^{s}$ and $B_{n,m}^{s}$ are zero, and we may simplify the potential expression as

$$\psi_{ext} = \sum_{n,m} L_{n,m}P_{n,m}(\eta)P_{n,m}(\xi)\cos m\varphi, \qquad (3.15a)$$

$$\psi_{ind} = \sum_{n,m} B_{n,m}Q_{n,m}(\eta)P_{n,m}(\xi)\cos m\varphi. \qquad (3.15b)$$

where $B_{n,m}$ is an (n, m)th-order spheroidal multipole at the origin.

3.4 Image schemes of a prolate spheroidal multipole

3.4.1 Grounded plane

Consider a multipole $B_{n,m}$ at the point **o**, which is at height H above a grounded plane, as shown in Figure 3.4. The multipole direction (z axis) makes angle α with the plane. The potential due to $B_{n,m}$ is

$$\psi_{B} = B_{n,m}Q_{n,m}(\eta)P_{n,m}(\xi)\cos m\varphi \qquad (3.16)$$

To satisfy the zero potential condition on the grounded plane, we place a multipole image $B'_{n,m}$ at **o**′ corresponding to coordinates (x', y', z') below the plane by the same distance H (see Figure 3.4). The magnitude $B'_{n,m}$ of the image is

$$B'_{n,m} = (-1)^{m+1}B_{n,m}. \qquad (3.17)$$
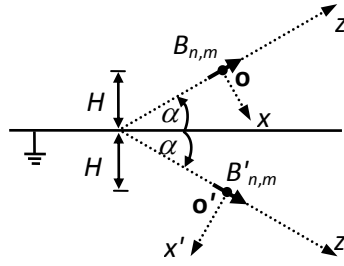
Figure 3.4. Image $B'_{n,m}$ of a multipole $B_{n,m}$ by a grounded plane.

3.4.2 Conducting prolate spheroid

Let consider a multipole $B_{n,m}$ outside a conducting prolate spheroid centered at **o**. We re-expand ψ_B about **o** in coordinates (η, ξ, φ) associated with the spheroid in the form of local expansion as

$$\psi_B = \sum_{i,j} L_{i,j} P_{i,j}(\eta) P_{i,j}(\xi) \cos(j\varphi), \tag{3.18}$$

where $L_{i,j}$ is the re-expansion coefficient. $L_{i,j}$ can be determined from [47],

$$L_{i,0} = \frac{2i+1}{4\pi P_{i,0}(\eta)} \int_{-1}^{1}\int_{-\pi}^{\pi} \psi_B P_{i,0}(\xi)\, \mathrm{d}\varphi \mathrm{d}\xi, \tag{3.19a}$$

and for $j \neq 0$,

$$L_{i,j} = \frac{(2i+1)(i-j)!}{2\pi(i+j)! P_{i,j}(\eta)} \int_{-1}^{1}\int_{-\pi}^{\pi} \psi_B P_{i,j}(\xi)\cos(j\varphi)\, \mathrm{d}\varphi \mathrm{d}\xi. \tag{3.19b}$$

Define multipole $B'_{i,j}$ located at the spheroid center **o** as the images of the multipole $B_{n,m}$. The resultant potential ψ outside the spheroid ($\eta \geq \eta_0$) is

$$\psi = \sum_{i,j} \left[L_{i,j} P_{i,j}(\eta) + B'_{i,j} Q_{i,j}(\eta) \right] P_{i,j}(\xi) \cos(j\varphi). \tag{3.20}$$

If the spheroid is grounded, the magnitude of the multipole images is calculated from the condition $\psi = 0$ at $\eta = \eta_0$,

$$B'_{i,j} = -\frac{P_{i,j}(\eta_0)}{Q_{i,j}(\eta_0)} L_{i,j} \text{ for } i \geq 0. \tag{3.21}$$

If the spheroid is electrically floating and has total charge Q, equation (3.21) holds for $i \geq 1$ and the relationship between Q and $B'_{0,0}$ is used for $i = 0$ as [64]

$$B'_{0,0} = \frac{Q}{4\pi\varepsilon_E a}. \tag{3.22}$$

3.4.3 Dielectric prolate spheroid

Consider a multipole $B_{n,m}$ outside a dielectric prolate spheroid centered at **o**. Similarly to the case of a conducting prolate spheroid, we first re-expand the potential of $B_{n,m}$ about **o** in the form of local expansion of equation (3.18). The electric field produced by $B_{n,m}$ induces polarization on the spheroid, resulting in surface charges. We use $B'_{i,j}$ located at the spheroid center **o** as the images of these charges. Resultant potential outside the spheroid surface is a sum of the potentials resulting from $B_{n,m}$ and $B'_{i,j}$.

The potential ψ outside the spheroid can be expressed in the form of equation (3.20), i.e.,

$$\psi = \sum_{i,j}\left[L_{i,j}P_{i,j}(\eta) + B'_{i,j}Q_{i,j}(\eta)\right]P_{i,j}(\xi)\cos(j\varphi) \cdot$$

The potential ϕ inside the spheroid can be written in the form of local expansion about the spheroid center **o**,

$$\phi = \sum_{i,j}M_{i,j}P_{i,j}(\eta)P_{i,j}(\xi)\cos(j\varphi), \tag{3.23}$$

where $M_{i,j}$ are the potential coefficients.

The boundary conditions on the spheroid surface ($\eta = \eta_0$) are

$$\phi = \psi, \tag{3.24a}$$

$$\varepsilon_S\left[\frac{\partial\phi}{\partial\eta}\right] = \varepsilon_E\left[\frac{\partial\psi}{\partial\eta}\right], \tag{3.24b}$$

where ε_S and ε_E are permittivity of the spheroid and the ambient medium, respectively. $B'_{i,j}$ and $M_{i,j}$ can be determined from $L_{i,j}$ as follows:

$$B'_{0,0} = 0$$
$$M_{0,0} = L_{0,0} \tag{3.25}$$

and for $i > 0$

$$B'_{i,j} = (\varepsilon - 1)\left[\frac{Q'_{i,j}(\eta_0)}{P'_{i,j}(\eta_0)} - \varepsilon\frac{Q_{i,j}(\eta_0)}{P_{i,j}(\eta_0)}\right]^{-1}L_{i,j}, \tag{3.26a}$$

$$M_{i,j} = \left[\frac{Q'_{i,j}(\eta_0)}{P'_{i,j}(\eta_0)} - \frac{Q_{i,j}(\eta_0)}{P_{i,j}(\eta_0)}\right]\left[\frac{Q'_{i,j}(\eta_0)}{P'_{i,j}(\eta_0)} - \varepsilon\frac{Q_{i,j}(\eta_0)}{P_{i,j}(\eta_0)}\right]^{-1}L_{i,j}, \tag{3.26b}$$

where $\mathcal{E} = \mathcal{E}_S/\mathcal{E}_E$, and the prime notation denotes the first order derivative of the associated Legendre functions.

3.5 Calculation procedure

The method of multipole images in the prolate spheroidal coordinates is applied to the electric field calculation in an iterative manner [64] for the configurations in Figure 3.2. The calculation procedure is presented in Figure 3.5. The calculation begins with the expression of the potential ψ_0 due to E_0 in the prolate spheroidal coordinates about the spheroid center $\mathbf{o}$ ($\eta = 1$ and $\xi = 0$).

$$\psi_0 = -(H+Z)E_0 = \sum_{n,m} L_{n,m} P_{n,m}(\eta) P_{n,m}(\xi)\cos(m\varphi), \quad (3.27)$$

where $H = h + \delta$ (see Figure 3.2a), and

$$\begin{aligned} L_{0,0} &= -HE_0, \\ L_{1,0} &= -a\sin\alpha E_0, \\ L_{1,1} &= a\cos\alpha E_0. \end{aligned} \quad (3.28)$$

From the boundary condition on the spheroid surface, we determine the induced multipole $B_{n,m}$ located at $\mathbf{o}$ from $L_{n,m}$. For a grounded conducting spheroid, we use equation (3.21). That is,

$$\begin{aligned} B_{0,0} &= \left[P_{0,0}(\eta_0)/Q_{0,0}(\eta_0) \right] HE_0, \\ B_{1,0} &= \left[P_{1,0}(\eta_0)/Q_{1,0}(\eta_0) \right] a\sin\alpha E_0, \\ B_{1,1} &= -\left[P_{1,1}(\eta_0)/Q_{1,1}(\eta_0) \right] a\cos\alpha E_0. \end{aligned} \quad (3.29)$$

When $\delta > 0$ (electrically floating spheroid), both equations (3.21) and (3.22) are applied. For a dielectric spheroid, we use equation (3.26a) to compute $B_{n,m}$. To calculate the electric field inside the spheroid, equation (3.26b) can be used to determine $M_{i,j}$.

Next, image $B'_{n,m}$ by the grounded plane is applied at $\mathbf{o}'$ to satisfy the zero-potential condition on the plane by using equation (3.17). Then, we re-expand potential by $B'_{n,m}$ about $\mathbf{o}$ by using equations (3.19a) and (3.19b). Numerical quadratures are used to evaluate these equations.

Afterward, we calculate image multipoles to satisfy again the boundary condition on the spheroid surface. The image application and the re-expansion are repeated until the potential on the spheroid converges. After the convergence, we

have two series of multipole images which represent the induced charge on the spheroid and that on its image with respect to the grounded plane.
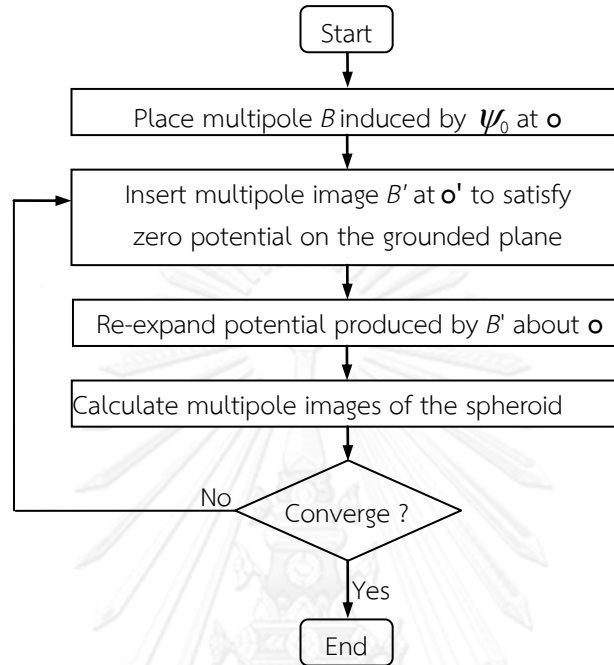
Figure 3.5. Iterative calculation scheme.

3.6 Calculation of charges, electrostatic force, and torque

Induced charge and electrostatic force are determined from the electric field on the spheroid surface. For the potential in equations (3.14) and (3.15), the electric fields on the surface in the η and ξ directions are

$$E_\eta^{out} = -\frac{1}{h_\eta} \sum_{n,m} \left[L_{n,m} P'_{n,m}(\eta_0) + B_{n,m} Q'_{n,m}(\eta_0) \right] P_{n,m}(\xi) \cos(m\varphi), \tag{3.30a}$$

$$E_\xi^{out} = -\frac{1}{h_\xi} \sum_{n,m} \left[L_{n,m} P_{n,m}(\eta_0) + B_{n,m} Q_{n,m}(\eta_0) \right] P'_{n,m}(\xi) \cos(m\varphi), \tag{3.30b}$$

The derivative of the associated Legendre functions can be determined from the recurrence formula as [47]

$$P'_{n,m}(x) = \frac{1}{x^2 - 1} \left[nx P_{n,m}(x) - (n+m) P_{n-1,m}(x) \right], \tag{3.31a}$$

$$Q'_{n,m}(x) = \frac{1}{x^2 - 1} \left[nx Q_{n,m}(x) - (n+m) Q_{n-1,m}(x) \right]. \tag{3.31b}$$

3.6.1 Induced charge

Density σ_f of the free charges induced on the surface of a conducting spheroid is determined as

$$\sigma_f = \varepsilon_E E_\eta^{out}. \tag{3.32}$$

For a dielectric spheroid, density σ_b of the polarization charges (bound charges) on the spheroid surface is determined from [65],

$$\sigma_b = \varepsilon_0 \left(E_\eta^{out} - E_\eta^{in} \right), \tag{3.33}$$

where E_η^{in} is taken inside the spheroid.

The total charge Q on the spheroid can be calculated directly from the monopole $B_{0,0}$ of the image multipoles by [64]

$$Q = 4\pi\varepsilon_E a B_{0,0}. \tag{3.34}$$

Q is always equal to zero for the dielectric spheroid.

3.6.2 Electrostatic force

The electrostatic force F_e is determined by integrating the Maxwell stress over the surface S of the spheroid,

$$\mathbf{F}_e = \varepsilon_E \oiint_S \left[\mathbf{E}^{out} E_\eta^{out} - \frac{1}{2}(E^{out})^2 \mathbf{a}_\eta \right] dS, \tag{3.35}$$

where $\mathbf{E}^{out} = E_\eta^{out}\mathbf{a}_\eta + E_\xi^{out}\mathbf{a}_\xi + E_\varphi^{out}\mathbf{a}_\varphi$. Note that for a conducting spheroid, equation (3.35) reduces to

$$\mathbf{F}_e = \frac{\varepsilon_E}{2} \oiint_S (E_\eta^{out})^2 \mathbf{a}_\eta dS. \tag{3.36}$$

As the electric field energy is invariant with respect to the X and Y positions of the spheroid in the configuration of Figure 3.2a, $\mathbf{F}_e$ vanishes in the X and Y directions. For $\delta = 0$, $\mathbf{F}_e$ is always in the upward direction for a conducting spheroid but in the downward direction for a dielectric spheroid, regardless of electric field direction. Therefore, the force tends to lift a conducting spheroid from the grounded plane but attach a dielectric spheroid to the plane.

The force per unit area $\mathbf{f}$ on the surface of conducting and dielectric spheroids is determined as

$$\mathbf{f} = \frac{\varepsilon_E}{\varepsilon_0}\sigma\left(\mathbf{E}^{out} - \mathbf{E}_\sigma^{out}\right),$$ (3.37)

where $\sigma = \sigma_f$ for the conducting spheroid and $\sigma = \sigma_b$ for the dielectric spheroid, and $\mathbf{E}_\sigma^{out}$ is the electric field produced by the charge at the current position,

$$\mathbf{E}_\sigma^{out} = \frac{\sigma}{2\varepsilon_0}\mathbf{a}_\eta.$$ (3.38)

We can also calculate $\mathbf{F}_e$ from $\mathbf{f}$ as

$$\mathbf{F}_e = \oiint_S \mathbf{f}\,\mathrm{d}S.$$ (3.39)

3.6.3 Torque

Torques on the spheroid about the spheroid center $\mathbf{o}$ and the lowest point $\mathbf{p}$ (contact point when $\delta = 0$) are considered in the dissertation. The electrostatic torque $T_{e,\mathbf{o}}$ about $\mathbf{o}$ is determined from the force per unit area $\mathbf{f}$ as

$$T_{e,\mathbf{o}} = \oiint_S \left(-Zf_X + Xf_Z\right)\mathrm{d}S,$$ (3.40)

where the subscripts X and Z indicate the components of $\mathbf{f}$. Positive torque is referred to the $+\alpha$ direction, as shown in Figure 3.6. Similarly, the electrostatic torque $T_{e,\mathbf{p}}$ about $\mathbf{p}$ is

$$T_{e,\mathbf{p}} = \oiint_S \left[-(Z+h)f_X + (X+d)f_Z\right]\mathrm{d}S.$$ (3.41)

As the line of the gravitational force F_g passes through $\mathbf{o}$, the torque of F_g about $\mathbf{o}$ is equal to zero and the gravitational torque $T_{g,\mathbf{p}}$ about $\mathbf{p}$ is

$$T_{g,\mathbf{p}} = -F_g d.$$ (3.42)

Therefore, the total torques on the spheroid about $\mathbf{o}$ and $\mathbf{p}$ are

$$T_{tot,\mathbf{o}} = T_{e,\mathbf{o}},$$ (3.43a)

$$T_{tot,\mathbf{p}} = T_{e,\mathbf{p}} + T_{g,\mathbf{p}}.$$ (3.43b)

Note that when the spheroid is in contact with the plane ($\delta = 0$), there is also a normal force at the contact point $\mathbf{p}$, but it does not produce torque about $\mathbf{p}$.
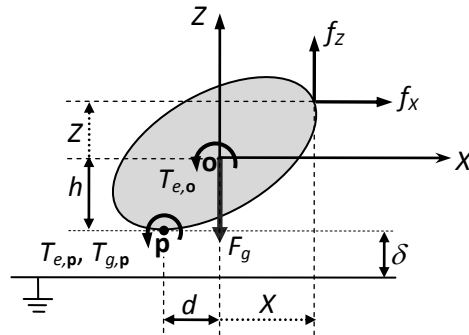
Figure 3.6. Calculation of torques on the spheroid.

3.7 Axisymmetric calculation

For the special case of α = 90°, the configuration in Figure 3.2 becomes axisymmetric about the major axis of the spheroid and the $m \neq 0$ harmonics vanish [47]. In this case, the formulae of the re-expansion coefficient and electrostatic force on the spheroid can be expressed in a closed form.

3.7.1 Re-expansion coefficient

Consider an nth-order unit harmonic

$$\overline{\psi}_n(\mathbf{r}') = Q_n(\eta')P_n(\xi') \tag{3.44}$$

expanded in the coordinates (x', y', z'), where the position vector is denoted as $\mathbf{r}'$. The image charge representing $\overline{\psi}_n(\mathbf{r}')$ is a line charge at η' = 1 having charge density $2\pi\varepsilon_E P_n(\xi')$ [64]. Thus, the harmonic may be written as an integral of the image line charge on the line η' = 1,

$$\overline{\psi}_n(\mathbf{r}') = \frac{a}{2}\int_{-1}^{1} P_n(\xi'_s)\frac{1}{\|\mathbf{r}'-\mathbf{z}'_s\|}d\xi'_s. \tag{3.45}$$

where $\mathbf{z}'_s$ is the position vector of the charge (η' = 1, $\xi' = \xi'_s$) on the image line.

We want to re-expand $\overline{\psi}_n(\mathbf{r}')$ about the origin $\mathbf{o}$ of the coordinates (x, y, z), which is at distance $2H$ above $\mathbf{o}'$, as shown in Figure 3.7, in the following form:

$$\overline{\psi}_n(\mathbf{r}') = \sum_{k=0}^{\infty} L_{k,n}P_k(\eta)P_k(\xi), \tag{3.46}$$

where $L_{k,n}$ is the coefficient of the re-expansion.

Using the orthogonal property of the Legendre polynomials, it can be concluded from (3.46) that

$$L_{k,n} = \frac{2k+1}{2} \frac{a}{2} \int\limits_{-1}^{1}\int\limits_{-1}^{1} P_n(\xi'_s)P_k(\xi_s) \frac{1}{\|\mathbf{r}' - \mathbf{z}'_s\|} d\xi'_s d\xi_s . \qquad (3.47)$$

In equation (3.47), $\|\mathbf{r}' - \mathbf{z}'_s\|$ is the vertical distance along the axis. Hence,

$$\frac{1}{\|\mathbf{r}' - \mathbf{z}'_s\|} = \frac{1}{2H + a\xi_s - a\xi'_s} = \frac{1}{a}\left[\frac{1}{(2H/a) + \xi_s - \xi'_s} \right]. \qquad (3.48)$$

By expanding equation (3.48) in term of (ξ_s, ξ'_s) about ($\xi_s = 0$, $\xi'_s = 0$), we obtain

$$\frac{1}{\|\mathbf{r}' - \mathbf{z}'_s\|} = \frac{1}{a}\left[\sum_{i=0}^{\infty}\sum_{j=0}^{\infty} \frac{(-1)^i}{(2H/a)^{i+j+1}} \frac{(i+j)!}{i!\,j!} \xi_s^i \xi_s'^j \right]. \qquad (3.49)$$

Substituting equation (3.49) into equation (3.47), we can obtain the re-expansion coefficient as a sum,

$$L_{k,n} = \frac{2k+1}{4}\left(\sum_{i=0}^{\infty}\sum_{j=0}^{\infty} \frac{(-1)^i}{(2H/a)^{i+j+1}} \frac{(i+j)!}{i!\,j!} I_{k,i} I_{n,j} \right), \qquad (3.50)$$

where

$$I_{n,j} = \int\limits_{-1}^{1} \xi^j P_n(\xi)d\xi . \qquad (3.51)$$

I_{n_j} is nonzero if $n + j$ is even and $j \geq n$ [66]:

$$I_{n,j} = \frac{2j!}{(j-n)!!(j+n+1)!!} . \qquad (3.52)$$
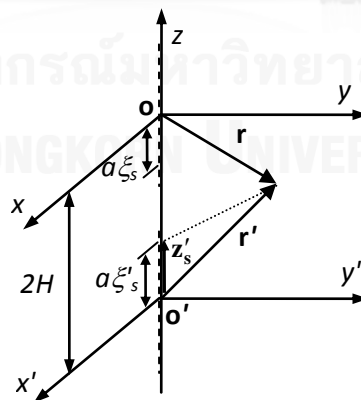
Figure 3.7. Origins of two coordinates (x, y, z) and (x', y', z') separated by distance $2H$.

3.7.2 Electrostatic force

The electrostatic force F_e can be calculated directly from multipole images based on the interaction between electric field and the multipoles in spherical coordinates [67]. The spheroidal multipoles B_n are transformed into spherical multipoles B_j^{sph} as [47],

$$B_j^{sph} = \frac{a^{j+1}}{2} \sum_{n=0}^{\infty} I_{n,j} B_n .$$

(3.53)

ϕ^{sph} is defined as the external potential, which is the sum of ψ_0 and $\psi_{B'}$. It can be expressed in the spherical coordinates (r, θ) as

$$\phi^{sph} = \sum_j L_j^{sph} r^n P_j(\cos\theta),$$

(3.54)

where L_j^{sph} is the potential coefficient. ϕ^{sph} in (3.54) is obtained by transforming multipoles B'_n into B'^{sph}_n by using equation (3.53) and re-expanding their potentials about the spheroid center **o** in the form of local expansion [68]. F_e can be expressed as [67]

$$F_e = -4\pi\varepsilon_E \sum_{j=0}^{\infty} (j+1) B_j^{sph} L_{j+1}^{sph} .$$

(3.55)

3.8 Isolated prolate spheroid under external electric field

This section considers the case in which the separation between the spheroid and the plane is so large that the influence of the plane is negligible. Figure 3.8 shows the configurations in which the major axis of the spheroid is parallel or normal to $\mathbf{E_0}$. The analytical solutions of the maximal field for these configurations are well known [8, 69-71].

(a) Parallel to $\mathbf{E_0}$ (b) Normal to $\mathbf{E_0}$
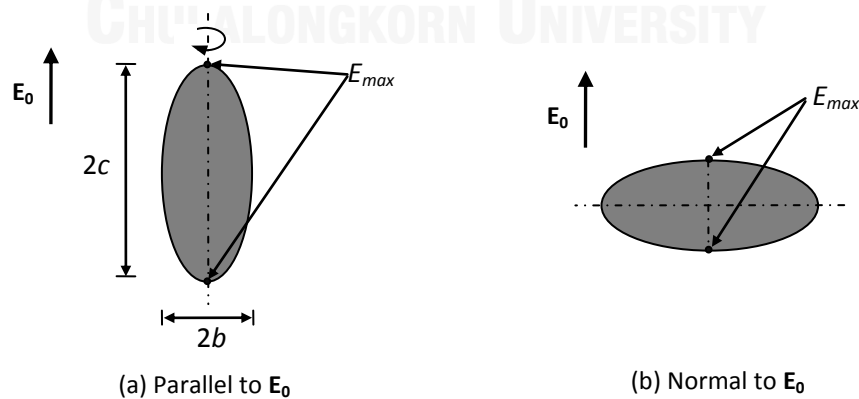
Figure 3.8. Two principal orientations of spheroid with reference to $\mathbf{E_0}$.

The position of the field maximum E_{max} on the spheroid surface is indicated in Figure 3.8. For the conducting spheroid parallel to E_0,

$$E_{max} = \frac{E_0}{[\eta_0 \text{arccoth}(\eta_0) - 1][\eta_0^2 - 1]}, \text{ and} \qquad (3.56a)$$

for the conducting spheroid normal to E_0,

$$E_{max} = \frac{2E_0}{\eta_0 [(1 - \eta_0^2)\text{arccoth}(\eta_0) + \eta_0]}, \qquad (3.56b)$$

where $\eta_0 = \dfrac{c}{\sqrt{c^2 - b^2}}$ defined in equation (2.7). Note that equation (3.56a) is also the maximal field for a hemispheroid on a grounded plane under external field. When $c/b \to 1$, E_{max} in equation (3.56) converges to $3E_0$, which is the solution for a conducting sphere. When $c/b \to \infty$, E_{max} becomes singular in equation (3.56a) but $2E_0$ in equation (3.56b) which corresponds to the case of a conducting cylinder.

For the dielectric spheroid, E_{max} is in the form [71]

$$E_{max} = \frac{\varepsilon E_0}{1 + (\varepsilon - 1)K}, \qquad (3.57)$$

where K is a function of η_0. When the major axis is parallel to E_0,

$$K = (\eta_0^2 - 1)\left[\frac{1}{2}\eta_0 \ln \frac{\eta_0 + 1}{\eta_0 - 1} - 1\right]. \qquad (3.58a)$$

When the major axis is normal to E_0,

$$K = \frac{1}{4}(\eta_0^2 - 1)\eta_0 \ln \frac{\eta_0 - 1}{\eta_0 + 1} + \frac{1}{2}\eta_0^2. \qquad (3.58b)$$

When $c/b \to 1$, E_{max} in both orientations converges to $[3\varepsilon/(\varepsilon + 2)]E_0$. When $c/b \to \infty$, K becomes 0 in equation (3.58a) and 0.5 in equation (3.58b). From equation (3.57), the maximal field becomes εE_0 and $[2\varepsilon/(\varepsilon + 1)]E_0$ for the spheroid parallel and normal to E_0, respectively.

Figure 3.9 shows the maximal field normalized by E_0 as a function of c/b from 1 to 10 for the parallel and normal orientations. The field is given for the dielectric-constant ratio ε = 2, 5, and 10 in the cases of the dielectric spheroid. The maximal field on the conducting spheroid is presented by the dashed line in the figures. It is clear from Figure 3.9 that the maximal field increases with c/b in the parallel

orientation but decreases with *c/b* in the normal orientation. For the same axis ratio *c/b*, the maximal field is greater for higher ε.
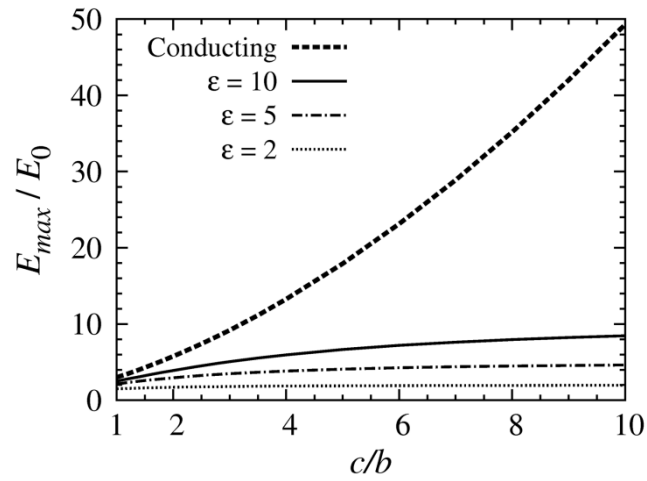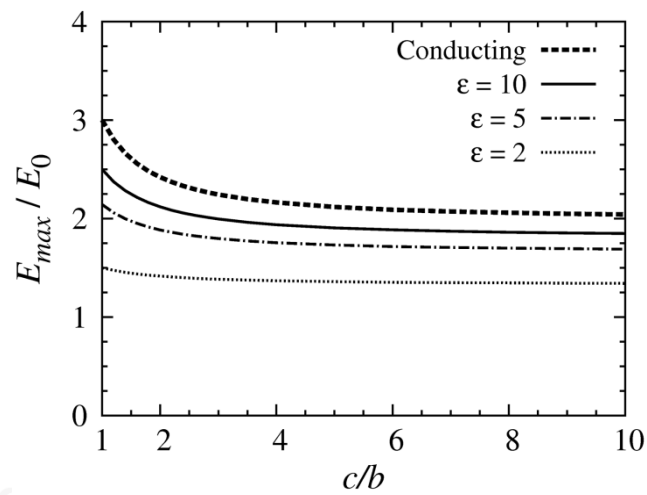
(a) Parallel to E$_0$

(b) Normal to E0

Figure 3.9. Maximal electric field on an isolated spheroid parallel or normal to external field E$_0$.

CHAPTER IV

ANALYTICAL RESULTS OF AXISYMMETRIC CONFIGURATION

This chapter presents the analytical results of the axisymmetric configuration in Figure 3.2b. The configuration is a conducting or dielectric spheroid, which may be in contact with or separated from a grounded plane under external electric field. The major axis of the spheroid is parallel to the external field. The charged condition is taken into account for the conducting spheroid separated from the plane. The multipole image method described in Chapter III is applied to the field analysis. The closed-form formula in equation (3.55) is used for the calculation of the electrostatic force on the spheroid. For the conducting spheroid, the calculation results are presented for the wide range of the axis ratio c/b between 1 and 32. The characteristic of the calculation accuracy with the order of harmonics has investigated. In this dissertation, the author utilizes up to 200th harmonics for the conducting spheroid with $1 \leq c/b \leq 32$ and 500th harmonics for the dielectric spheroid with $1 \leq c/b \leq 4$ and $1 \leq \varepsilon \leq 6$. Note that it is more difficult to realize high accuracy in the cases of dielectric spheroid than conducting spheroid. Details of the calculation accuracy are given in Appendix A.

For presenting calculation results, we define l as the arc length measured from the top pole of the spheroid and L as the arc length between the top and bottom poles, as shown in Figure 4.1. Figure 4.2a plots the normalized l/L, as a function of $\Delta\xi$ from the pole for the spheroids having different c/b values. The area obtained by rotating l around the z-axis is defined as S_l. Figure 4.2b presents the ratios of S_l to the total surface area S, which are independent of the spheroid size, as a function of the normalized arc length l/L for different c/b values.
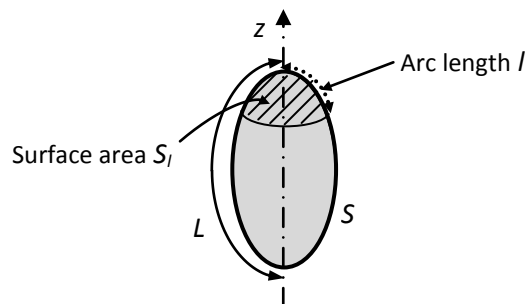
Figure 4.1. Arc from the top pole having length l and forming surface area S_l of revolution.
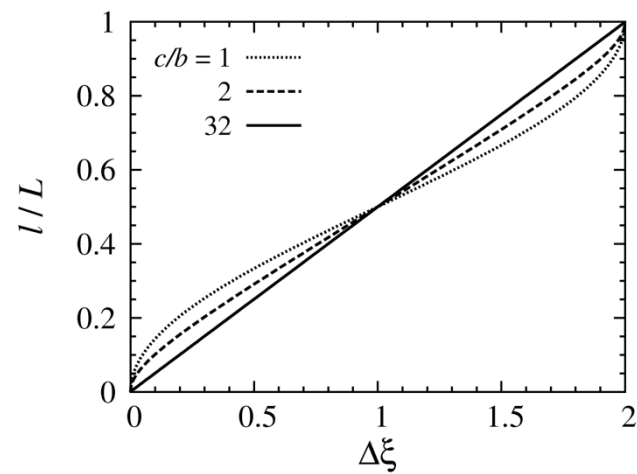
(a) Arc length l
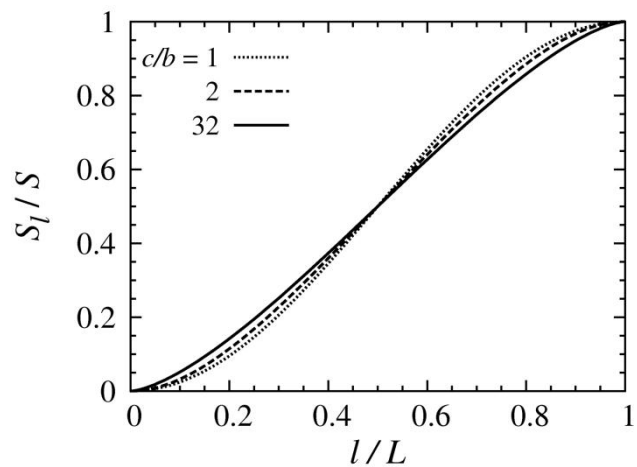
(b) Surface area S_l

Figure 4.2. Normalized arc length and surface area of spheroids having different c/b values.

4.1 Conducting spheroid

4.1.1 Spheroid in contact with a grounded plane

a) Electric field

Figure 4.3 shows the distribution of electric field along the spheroid surface for c/b = 1, 2, and 4. In the figure, the electric field is maximal at the top pole (l/L = 0) and zero at the bottom pole (l/L = 1). Since the field is very high on the upper half of the spheroid, almost all of the induced charge and electrostatic force on the spheroid are distributed on the upper half. Figure 4.4 shows the variation of the

maximal field E_{max} for c/b = 1 to 32. The maximal field is significantly intensified with increasing c/b.
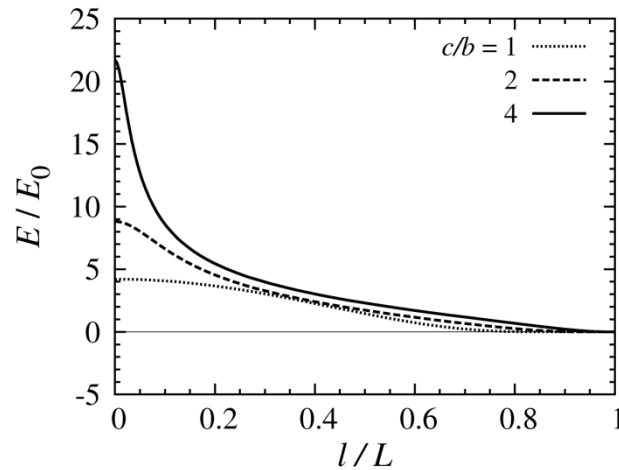
Figure 4.3. Distribution of electric field along the spheroid surface.
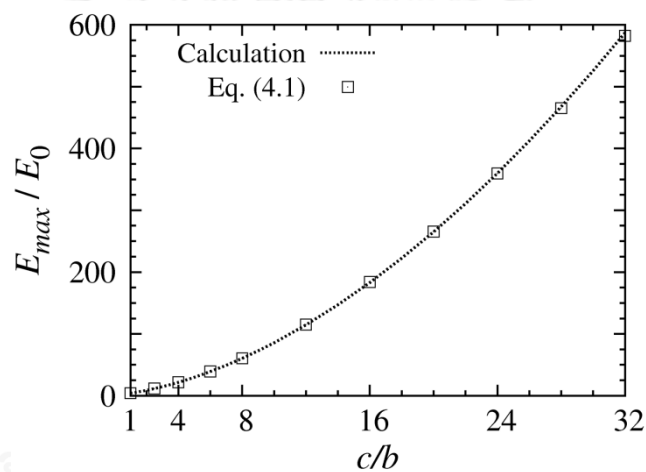
Figure 4.4. Maximal field as a function of the axis ratio c/b.

The following empirical formula, obtained by curve fitting, may be used for estimating the maximal field magnitude:

$$\frac{E_{max}}{E_0} = 1.37\left(0.92 + \frac{c}{b}\right)^{\sqrt{3}}.$$

(4.1)

This expression has a similar form to the approximation of the electric field at the contact point of an uncharged conducting spheroid on a solid dielectric [72]. The estimation by equation (4.1) is presented by the symbols in Figure 4.4. Table 4.1 shows the error of the estimated values in comparison with the maximal field by the

calculation results. It can be seen from Table 1 that the error is smaller than 1% for the *c/b* ratio up to 32.

Table 4.1. Comparison of the maximal field with the approximation by equation (4.1).

c/b	E_{max}/E_0		Error
	Calculation	Equation (4.1)	(%)
1	4.21	4.24	0.71
4	21.7	21.6	0.46
8	60.4	60.6	0.33
16	183	184	0.55
32	587	582	0.85

b) Induced charge and electrostatic force

Figures 4.5a and 4.5b present the charge Q_l and force F_l on the surface S_l as a function of *l/L*. Q_l and F_l are calculated by using numerical quadratures, and normalized by the total charge Q and total force F_e on the whole spheroid, respectively. As shown in Figure 4.5a, about 80% of the net induced charge resides on the upper half of the sphere and spheroid, for example, 77% for *c/b* = 32. For higher *c/b*, a higher portion of the induced charge is located around the top pole. It is clear from Figure 4.5b that the force on the lower half is negligible for all cases of *c/b*. For high *c/b*, the force in the vicinity of the top pole becomes predominant. For instance, 90% of the total force acts on 5% surface area around the top pole (at *l/L* ≈ 0.1, see Figure 4.2b) when *c/b* = 32.

The calculation results of the total charge Q and total force F_e are presented by the curves in Figure 4.6 as a function of the axis ratio *c/b*. The charge and force are normalized respectively by $Q_0 = \mathcal{E}_E S E_0$ and $F_0 = \mathcal{E}_E S E_0^{2}$. Figure 4.6 indicates that the charge and force increase with *c/b*. When *c/b* increases from 1 to 8, the charge and force increase by about two times. It is worth noting that the characteristics of the normalized charge and force are very similar to each other. Based on the calculation results, the following empirical formulae are proposed to evaluate the normalizing factors of the total charge and force on a spheroid in range *c/b* = 1 to 32:

$$\frac{Q}{Q_0} = 0.917\left(1.33 + \frac{c}{b}\right)^{\frac{1}{\sqrt{2}}}, \qquad (4.2)$$

$$\frac{F}{F_0} = 0.88\left(0.92 + \frac{c}{b}\right)^{\frac{1}{\sqrt{2}}}.$$

(4.3)

The approximated charge and force values by equations (4.2) and (4.3) are presented by symbols in Figure 4.6. Table 4.2 shows the errors of the approximated charge and force with the calculation results. We can see from the table that the error by the approximation is smaller than 2% for the considered range of c/b.
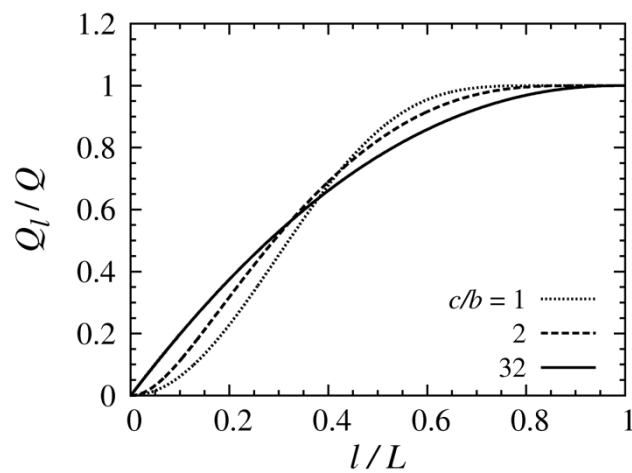
(a) Induced charge
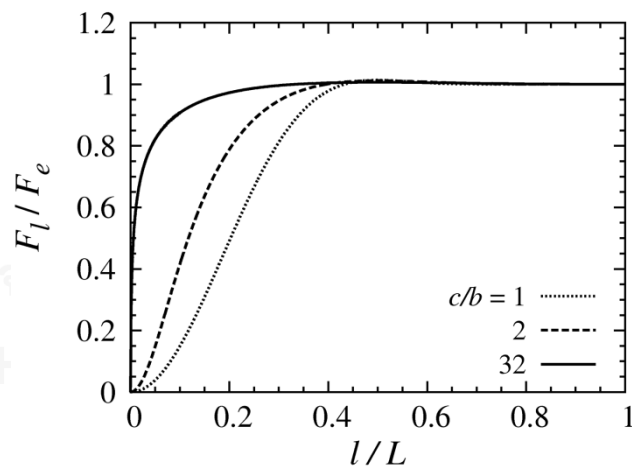
(b) Electrostatic force

Figure 4.5. Induced charge and electrostatic force on the surface area S_l as a function of l/L.
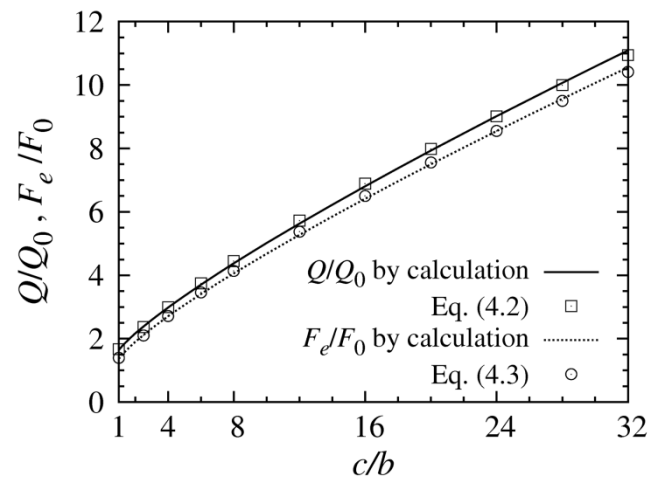
Figure 4.6. Total charge and force on the spheroids having the same surface area.

Table 4.2. Errors of the total charge and total force by the approximation in equations (4.2) and (4.3).

c/b	Q/Q_0		F_e/F_0	
	Calculation	Error (%) by equation (4.2)	Calculation	Error (%) by equation (4.3)
1	1.65	1.09	1.37	1.90
4	2.98	0.47	2.71	0.18
8	4.38	1.55	4.06	1.85
16	6.81	1.20	6.42	1.25
32	11.1	1.41	10.6	1.78

Figure 4.6 confirms the dependence of the charge and force on a spheroid on its axis ratio and surface area. To examine the effect of the shape and size of spheroids, the author compares the charge and force between spheroids having the same minor axis $2R_0$ (Figure 4.7a) and those having the same major axis $2R_0$ (Figure 4.7b). The spheroid is longer in the former case and slender in the latter case with increasing c/b. The charge and force are normalized by

$$Q_1 = 4\pi\varepsilon_E R_0^2 E_0 \text{ and}$$

$$F_1 = 4\pi\varepsilon_E R_0^2 E_0^2, \text{ respectively.}$$

Figure 4.7a shows that for the same minor axis, the charge and force increases significantly with increasing c/b. For instance, the charge and force on the spheroid

with $c/b = 4$ is approximately six times of that on the sphere ($c/b = 1$). On the other hand, for the same major axis in Figure 4.7b, the charge and force decrease with increasing c/b. The decreasing rates of the charge and force are remarkable for c/b between 1 and 4, about 60%.

Figure 4.8 presents the ratio F_e/QE_0, which is independent of the spheroid size. The figure shows that the force ratio on the spheroid is greater than that on the sphere, $F_e = 0.832QE_0$, and increases with c/b. This is because that for higher c/b the attractive force between the induced charge on the spheroid and its image with respect to the grounded plane is smaller (since the induce charge tends to distribute more near the top pole). Figure 4.8 also indicates that the force is still smaller than QE_0 by about 5% for the axis ratio up to 32.
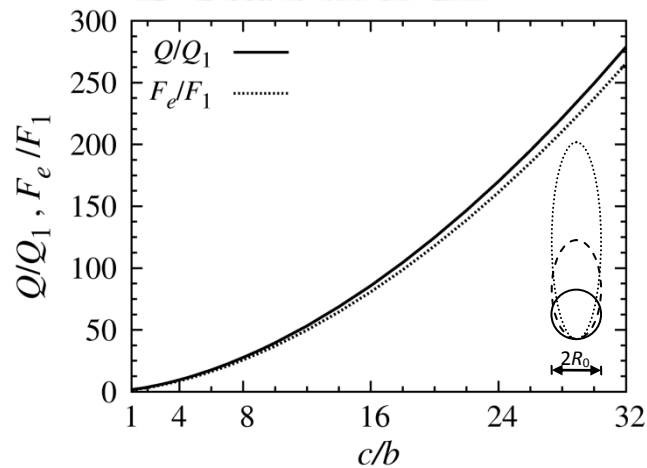
(a) In the same minor axis
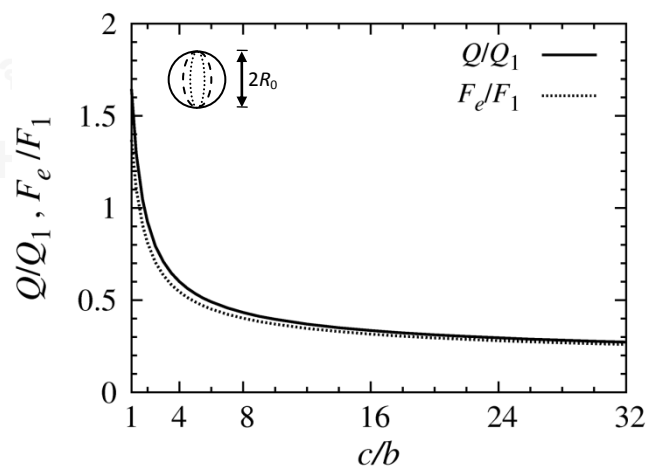
(b) In the same major axis

Figure 4.7. Total charge and total force on the spheroids having the same minor axis and major axis a function of c/b.
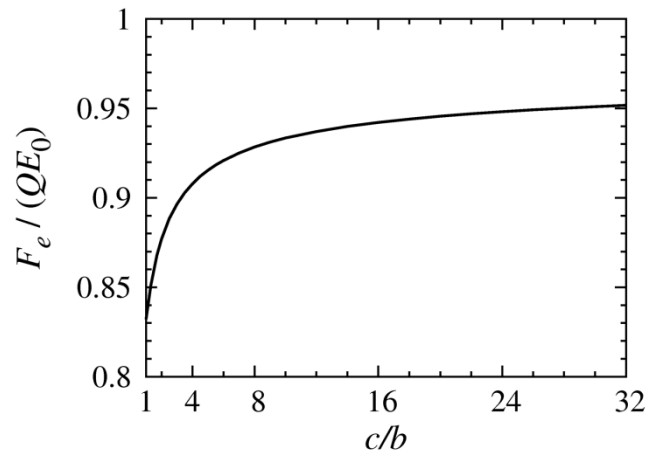
Figure 4.8. Ratio of the force to QE_0 as a function of c/b.

c) Hemispheroid approximation

The force on a prolate hemispheroid standing on a grounded plane under an external electric field has been studied analytically and numerically [49]. The exact solution of the charge for the hemispheroid was also presented and compared with an approximate formula [48]. This section compares my calculation results with those approximated by using a hemispheroid model. The hemispheroidal model is presented in Figure 4.9, where the major semi-axis is $2c$. Two cases of the minor semi-axis b_H, $b_H = b$ and $2b$, are considered. The author expects that the former model works for slender spheroids because the results in the previous section show that the electric field is very small on the lower-half surface of these spheroids.
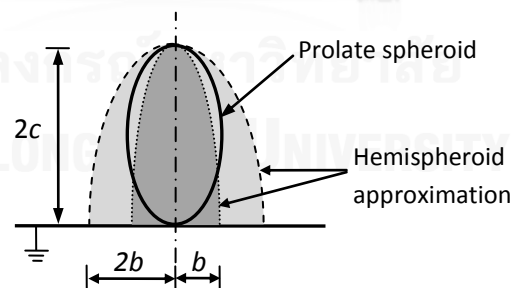
Figure 4.9. Hemispheroidal approximation for a prolate spheroid.

The difference of the maximal electric field by the approximation is given in Figure 4.10. For $b_H = b$, the approximation is always greater than the analytical values. The difference is larger than 37% for $c/b = 1$ and increases with c/b. On the other hand, for $b_H = 2b$, the approximation is always smaller than the actual values. The

difference is between 20% and 40% for the range of c/b. Therefore, neither case of b_H is appropriate for evaluating of the maximal field.

Figure 4.11 presents the differences of Q and F_e by the hemispheroid approximation when $b_H = b$. The differences are smaller than 15% for $c/b = 1$ and decrease with c/b. This approximation can estimate Q and F_e with a difference smaller than 10% for $c/b > 3$. The charge and force by the approximation are smaller than the analytical results. With increasing c/b, the difference of E_{max} increases in Figure 4.10; however, the region of high electric field is more restricted. Therefore, the difference of Q and F_e becomes smaller with increasing c/b in Figure 4.11. Note that the comparison when $b_H = 2b$ is not presented here because the differences of Q and F_e (with the analytical results) are much larger than those when $b_H = b$.
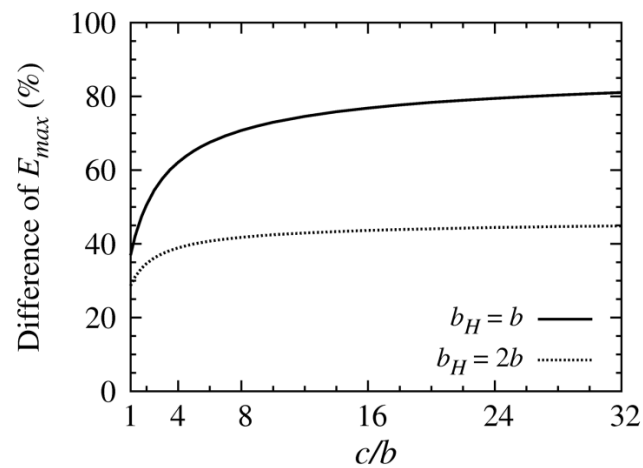
Figure 4.10. Difference of E_{max} by the hemispheroidal approximation in comparison with the results by the multipole image method.
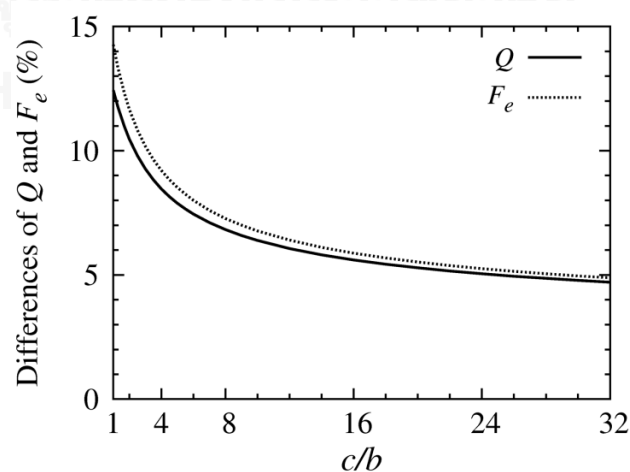
Figure 4.11. Differences of Q and F_e by hemispheroidal approximation when $b_H = b$ in comparison with the results by the multipole image method.

4.1.2 Uncharged spheroid above a grounded plane

In this section, a spheroid located above the grounded plane by distance or separation δ is considered. The spheroid is assumed to be uncharged. Under the external field, a potential difference exists between the spheroid and the grounded plane. With decreasing δ, the electric field can be highly intensified at the bottom pole of the spheroid.

a) Electric field

Figure 4.12 presents the distribution of electric field along the spheroid surface when δ/c = 0.1. The positive field magnitude is referred to the direction outward from the spheroid. It is clear from the figure that the electric field is stronger for higher c/b. The field enhances significantly at the two poles. The field maximum is always at the bottom pole (l/L = 1). Figure 4.13 presents the maximal field magnitude E_{max} at the bottom pole as a function of the normalized distance δ/c from 0.01 to 10. The figure indicates that the maximal field increases significantly with decreasing δ/c from 0.1 to 0.01.
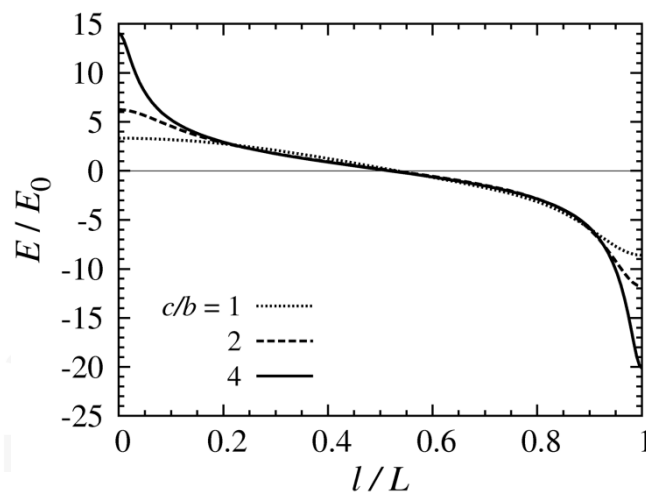
Figure 4.12. Distribution of electric field along the spheroid surface for different c/b ratios when δ/c = 0.1.
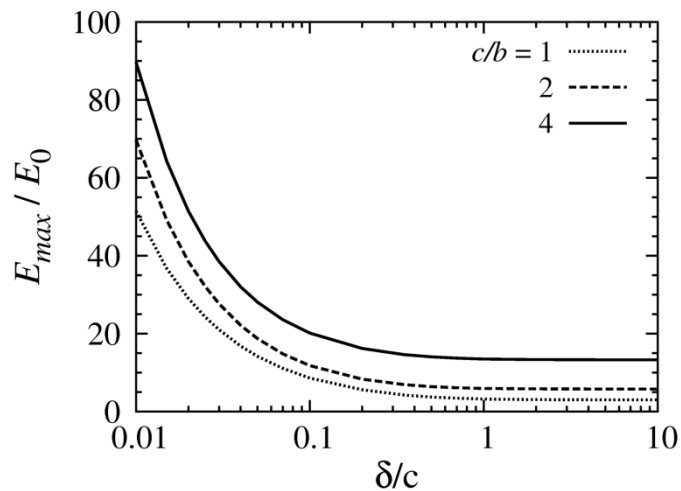
Figure 4.13. Magnitude of maximal field at the bottom pole as a function of δ/c.

b) Critical separation

As mentioned in the previous section, the electric field at the bottom pole of the spheroid is enhanced significantly on an uncharged spheroid located near the grounded plane. This may result in the partial discharge inception near the bottom pole. For the case of a sphere, the discharge threshold in the gap was estimated by using the Paschen curve for a uniform field [73]. For the spheroid, due to the field nonuniformity in the gap, the application of the Paschen curve may be inappropriate. For approximation, the author compares the maximal field E_{max} on a spheroid with the critical field stress E_c of a gaseous medium surrounding the spheroid to observe the variation of the critical separation δ_c of the partial discharge onset. This estimation is applied to different axis ratio c/b values.

As an example, E_c = 30 kV/cm is used for the atmospheric air. Figure 4.14 illustrates the determination of δ_c when E_0 = 4 kV/cm. Three curves in Figure 4.14 represent the maximal field on the spheroid for c/b = 1, 2, and 4 from Figure 4.13 and the horizontal line represents E_c. δ_c is determined from the intersection between the E_{max} curves and the E_c line. For example, δ_c = 0.12c and 0.26c for c/b = 1 and 2, respectively. For c/b = 4, δ_c becomes infinite because E_{max} is always higher than E_c. This means that the partial discharge occurs at the bottom pole for any separation under this E_0 value. (For c/b = 4, the partial discharge also occurs at the top pole as the top-pole field is greater than E_c.)
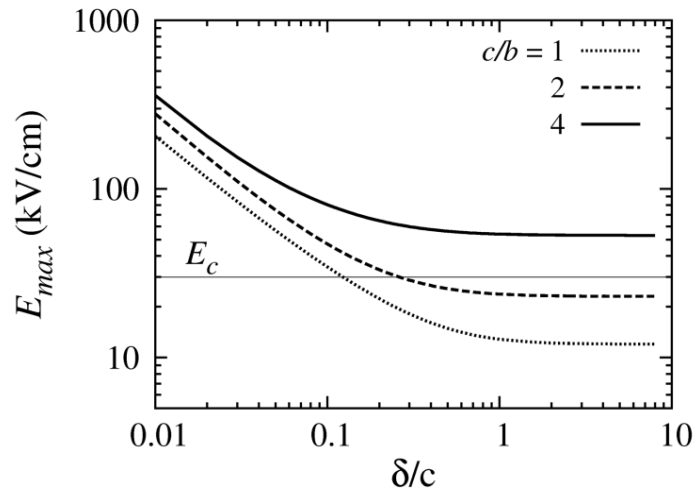
Figure 4.14. Variation of the maximal field on the spheroids under $E_0 = 4$ kV/cm and the critical field stress E_c with separation δ.

Figure 4.15 presents the relationships of the critical separation δ_c for the partial discharge onset and the external field E_0, varied from 0.1 kV/cm to 10 kV/cm, for c/b = 1, 2, 4, and 8. Needless to say that with decreasing E_0, δ_c becomes smaller. For $\delta_c/c > 1$, the influence of the plane is negligible; hence, the external field E_0 for the partial discharge hardly depends on δ_c. For smaller δ_c/c ratio, the relationships in Figure 4.15 become approximately linear in the logarithmic scale. That is,

$$\frac{\delta_c}{c} \propto E_0^k, \tag{4.4}$$

where k = 1.16, 1.19, 1.21, and 1.59 for c/b = 1, 2, 4 and 8, respectively. We can modify Figure 4.15 for other background medium by scaling the abscissa with the ratio of the critical field strength E_c corresponding to the medium. For example, E_0 in the figure is scaled by 9 times when the medium is SF_6 at 0.3 MPa whose E_c is about 270 kV/cm. However, it should be noted that the estimation based on E_c does not consider the physical discharge mechanisms. For a very small gap, the microdischarge process may play an important role on the determination of the discharge onset [74].
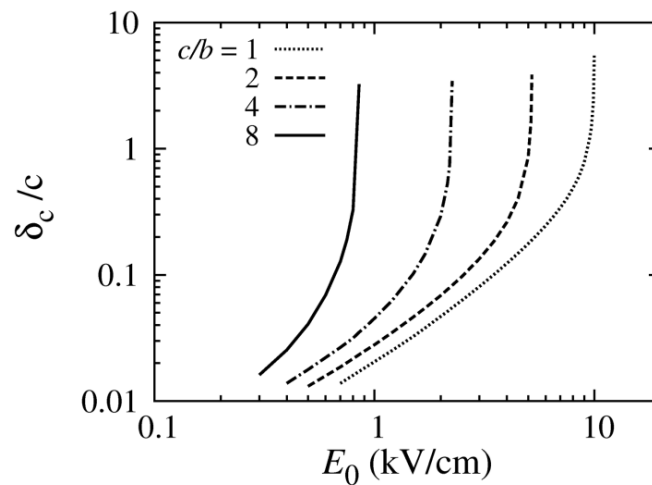
Figure 4.15. Relationship between the critical separation for the partial discharge onset and the external field for different axis ratios.

4.1.3 Charged spheroid above a grounded plane

This section considers a charged spheroid located above the grounded plane. Q_i is defined as the charge amount on the spheroid. The spheroid possibly acquires Q_i by the contact treated in Section 4.1.1 or by the discharge explained in Section 4.1.2. In the former case, the spheroid is fully charged to mount Q which is the total induced charge on the spheroid in contact with the grounded plane. The value of Q varies with the axis ratio, as already presented in Figure 4.6.

a) Fully charged spheroid $Q_i = Q$

As an example, Figure 4.16 presents the electric field distribution along the spheroid surface of the axis ratio $c/b = 2$ for different δ/c values. It is clear from Figure 4.16 that the field magnitude near the bottom pole ($l/L = 1$) increases with increasing δ. This increase reflects the redistribution of charges to the area. However, the electric field hardly changes with δ on the upper half. The maximum field is at the top pole ($l/L = 0$), similarly to the case of the grounded spheroid in Section 4.1.1, as the electric field direction due to charge Q is in the same direction with the external field E_0 at the top pole but in the opposite direction with E_0 at the bottom pole.

Figure 4.17 shows the electrostatic force on the spheroid for the variation of δ/c from 0.01 to 10. The force is normalized by the product QE_0. The figure implies that the normalized force increases with δ/c and is greater for higher c/b. The force converges well to QE_0 when $\delta/c \geq 10$.
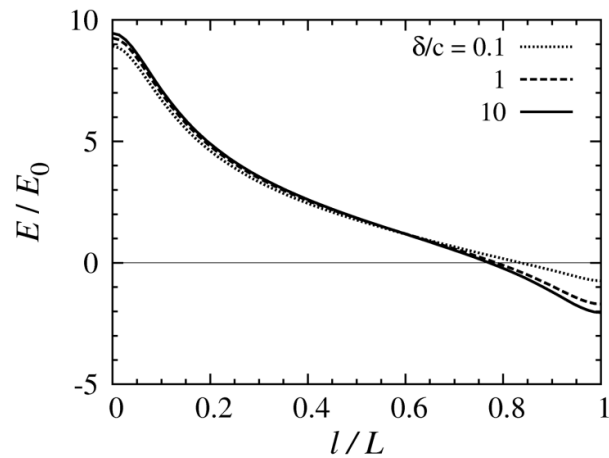
Figure 4.16. Electric field distribution on the surface of a fully charged spheroid with $c/b = 2$.
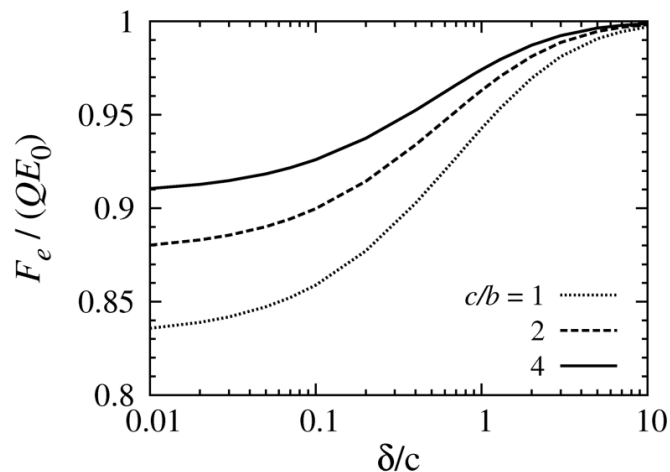
Figure 4.17. Force on the fully charged spheroid as a function of δ/c.

b) Spheroid with $Q_i \leq Q$

As mentioned in Section 4.1.2, when an uncharged ($Q_i = 0$) spheroid approaches the grounded plane, the significant enhancement of the electric field at the bottom pole may trigger a partial discharge at the pole. When the discharge occurs, space charges flow into the spheroid, as described in Chapter II. These charges increase the electric field at the top pole but reduce that at the bottom pole. This results in that the position of the maximal field transfers to the bottom pole to the top pole when the charge amount increases. In addition, the partial discharge at the bottom pole becomes more difficult to sustain with increasing charge because the electric field is reduced at the bottom pole. ΔE is defined as the field reduction at the bottom pole in comparison with the uncharged condition,

$$\Delta E = \frac{E_i(Q_i = 0) - E_i(Q_i)}{E_i(Q_i = 0)} \times 100\% \,, \tag{4.5}$$

where E_i is the field strength at the bottom pole when the spheroid has the charge amount Q_i.

Figures 4.18a and 4.18b present the field reduction ΔE as a function of Q_i/Q varied from 0 to 1 for the spheroids with c/b = 2 and 4, respectively. The results in the figures are given for the cases of δ/c = 0.01, 0.1, 1, and 10. It can be seen from the figures that the reduction increases linearly with Q_i/Q for all values of δ/c and c/b. The reduction is larger for smaller δ/c and does not depend much on the axis ratio c/b. For Q_i/Q = 1, the reduction is greater than 60% when δ/c = 10 and approximately 100% when δ/c = 0.01.
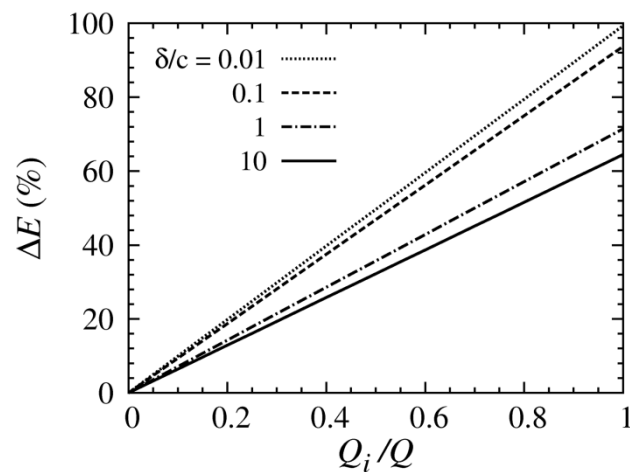
(a) c/b = 2
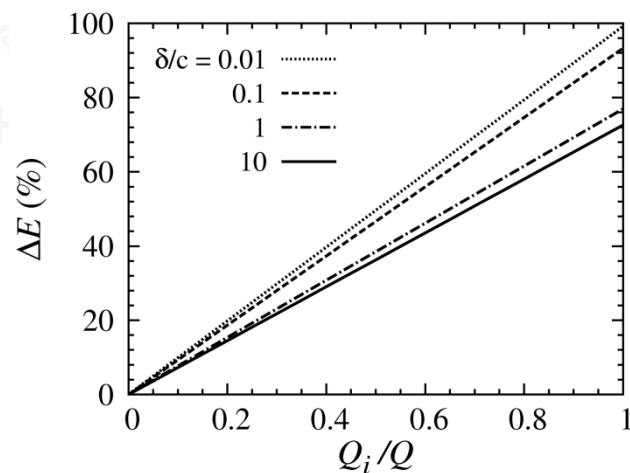
(b) c/b = 4

Figure 4.18. Reduction of the electric field at bottom pole for different δ/c values.

Figure 4.19 presents the result of the electrostatic force on the spheroids with variation of Q_i at different δ/c values. The positive force is referred to the force repulsing the spheroid from the plane. As shown in Figure 4.19, when $\delta/c > 1$, the force is positive for the considered range of Q_i, except $Q_i = 0$. This means that charged spheroids tend to move away the plane when $\delta/c > 1$. When $\delta/c \leq 1$, the force changes from positive value to negative one with decreasing Q_i. For example, at $\delta/c = 0.1$, the force is negative when $Q_i/Q < 0.18$ for $c/b = 2$ and when $Q_i/Q < 0.12$ for $c/b = 4$. In other word, at this δ/c if the charge loss is greater than 82 and 88% for $c/b = 2$ and 4, respectively, the spheroids are still attracted to the plane by F_e. Hence, when a spheroid is near the plane, it may move up or down with charge Q_i less than Q.
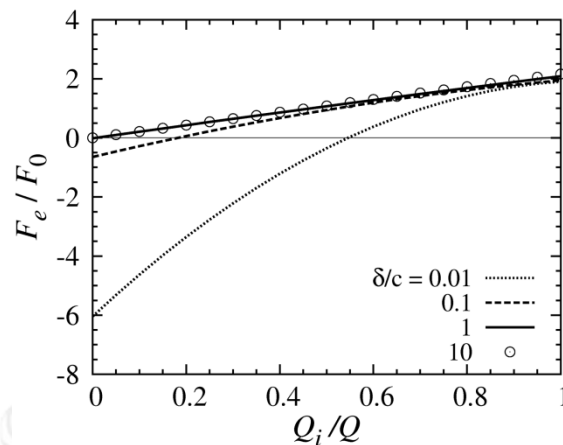
(a) $c/b = 2$
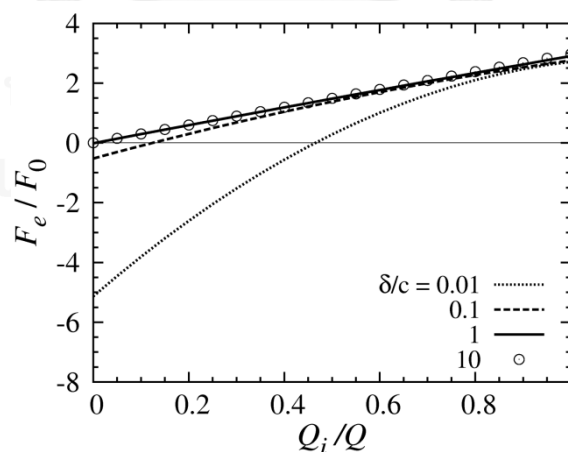
(b) $c/b = 4$

Figure 4.19. Force on the spheroids at different δ/c values as a function of Q_i/Q.

4.2 Uncharged dielectric spheroid

4.2.1 Spheroid in contact with a grounded plane

Figures 4.20a and 4.20b show the distribution of the normal electric field along the spheroid surface as a function normalized arc length l/L for $\mathcal{E}$ = 2 and 4, respectively. The figures show that the behavior of the electric field along the surface of a dielectric spheroid is similar to that of an uncharged conducting spheroid near the plane in Figure 4.12. That is, the field strength enhances considerably at the two poles and is always maximal at the bottom pole (l/L = 1). The top-pole field is slightly greater than the maximal field of an isolated spheroid presented in Section 3.8. In Figure 4.20, with increasing $\mathcal{E}$, the field distribution becomes more nonuniform near the bottom pole.
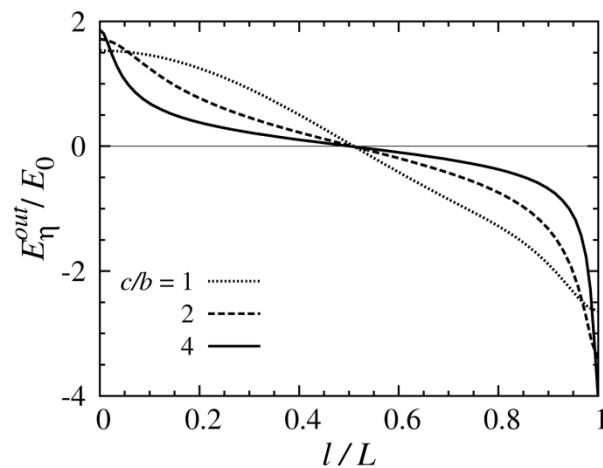
(a) $\mathcal{E}$ = 2
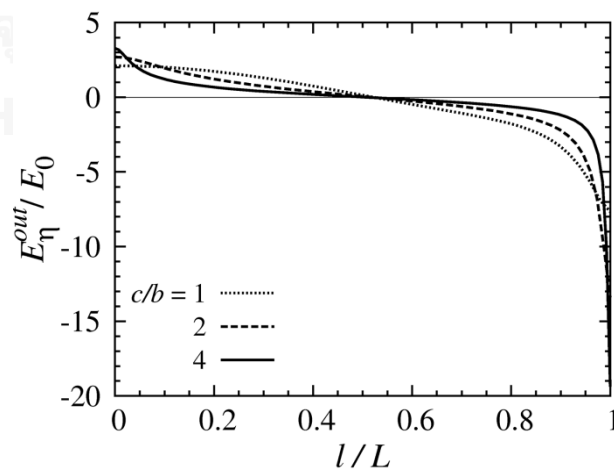
(b) $\mathcal{E}$ = 4

Figure 4.20. Normal electric field along the spheroid surface.

Figure 4.21 presents the maximum of the electric field at the bottom pole as a function of c/b from 1 to 4 for ε = 2, 4, and 6. It is clear from the figure that the maximal field increases with the axis ratio c/b. The increase is more remarkable for larger ε. Figure 4.21 indicates that the maximal field for ε = 2 and 4 may approach a limiting value when $c/b > 4$. Note that for the case of the isolated dielectric spheroid (without the grounded plane), the maximal field converges to εE_0 as $c/b \rightarrow \infty$.
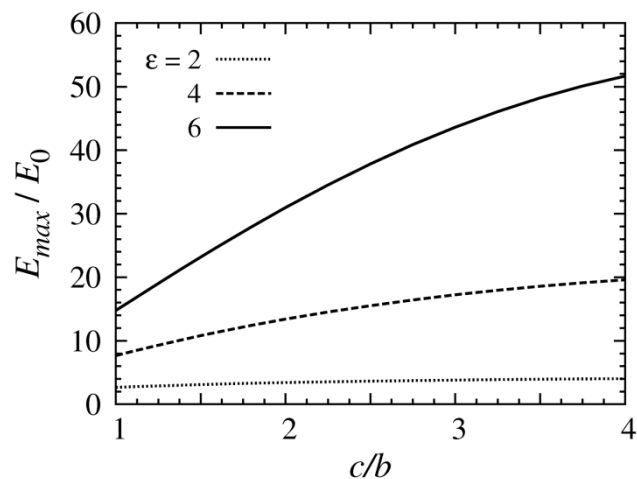
Figure 4.21. Electric field maximum at the bottom pole as a function of c/b.

Figure 4.22 shows the magnitude of the attractive fore between the dielectric spheroid and the grounded plane. The force in the figure is normalized by $\varepsilon_E S E_0^2$. It is obvious from the figure that the effect of ε on the normalized force is similar to that on the maximal field. That is, for the same c/b, the force is greater than for larger ε. For ε = 2 and 4, the normalized force reduces gradually with increasing c/b from 1. For ε = 6, the normalized force increases slightly with c/b to the maximum and reduces rapidly when $c/b \geq 2$.
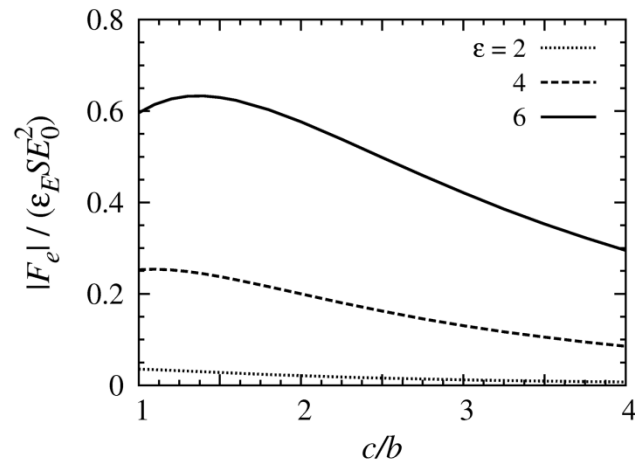
Figure 4.22. Normalized electrostatic force on the dielectric spheroids for different ε values as a function of c/b.

4.2.2 Spheroid above a grounded plane

This section considers the configuration of an uncharged dielectric spheroid located at a distance δ above the grounded plane. This configuration is identical in electric field to that of two identical dielectric spheroids separated by a distance 2δ. When δ approaches 0, the calculation result in this section converges to that in the previous one.

Figures 4.23a and 4.23b present the maximal field E_{max} at the bottom pole of the spheroid with c/b = 1, 2, and 4 for ε = 2 and 4, respectively. The field is plotted as a function of the normalized separation δ/c varied from 10^{-4} to 10 on the logarithmic scale. Figure 4.23 indicates that E_{max} is nearly constant with δ/c decreasing from 10 to 1 but increases significantly with decreasing δ/c from 0.1 to 0.001. Theoretically, as $\delta/c \rightarrow 0$, E_{max} in Figure 4.23 converges to the maximal field at the contact point between the spheroid and the plane presented in Figure 4.21. However, even at $\delta/c = 10^{-4}$, E_{max} is still considerably lower than the limiting value, especially for c/b = 4 and ε = 4 in Figure 4.23b (E_{max}/E_0 = 20 when δ = 0).
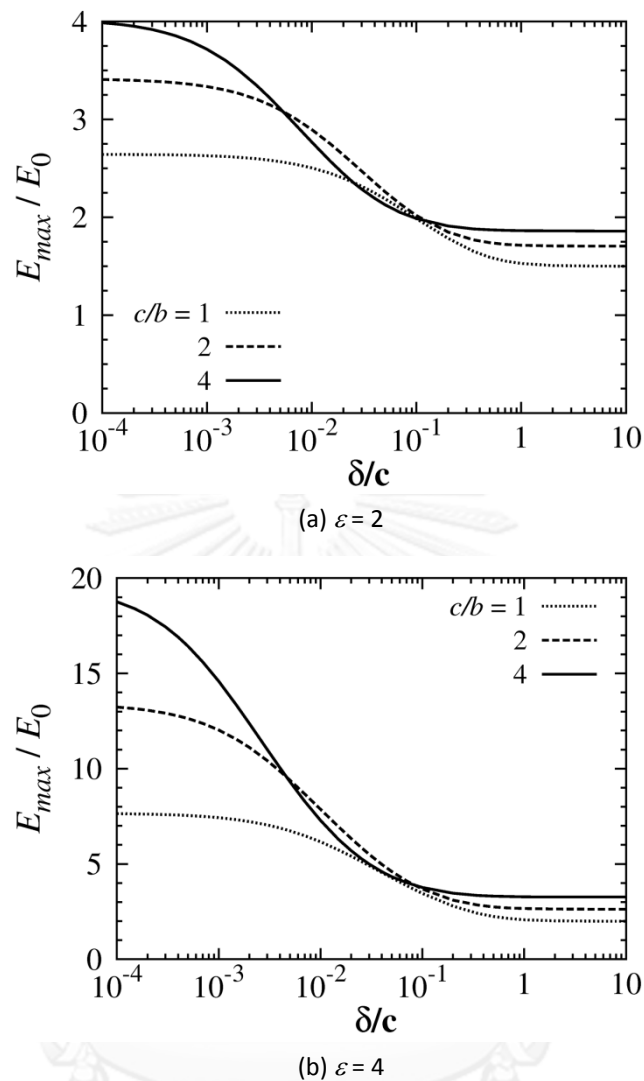
Figure 4.23. Maximal electric field at the bottom pole as a function of δ/c for two ε values.

The variation of the electrostatic force on the spheroids with the separation δ is presented in Figure 4.24. We can see from the figure that for the same δ/c the normalized force is greater for smaller c/b and higher ε. The force on the sphere (c/b = 1) approximately zero when $c/b \geq 3$. This means that the effect of the grounded plane on the force is negligible in this c/b range. The force increases remarkably when the separation δ/c decreases from 1 to 0.01. With $\delta/c = 10^{-4}$, the force well reaches the limiting value for the ranges of c/b and ε. Hence, as $\delta/c \to 0$, the force more rapidly approaches the limit in comparison with the maximal field.
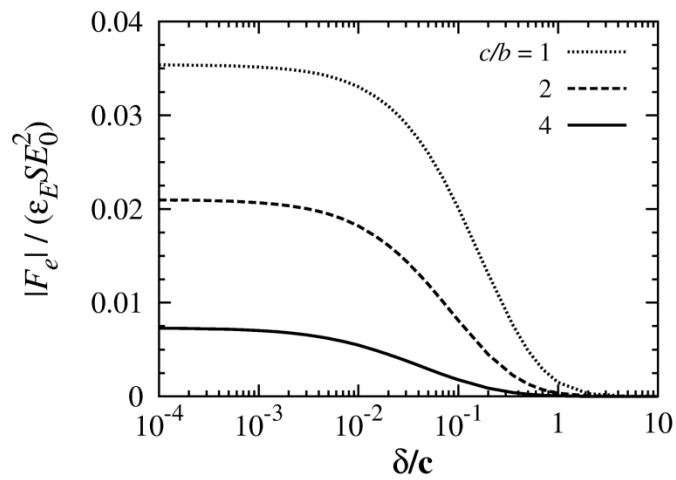
(a) $\mathcal{E} = 2$
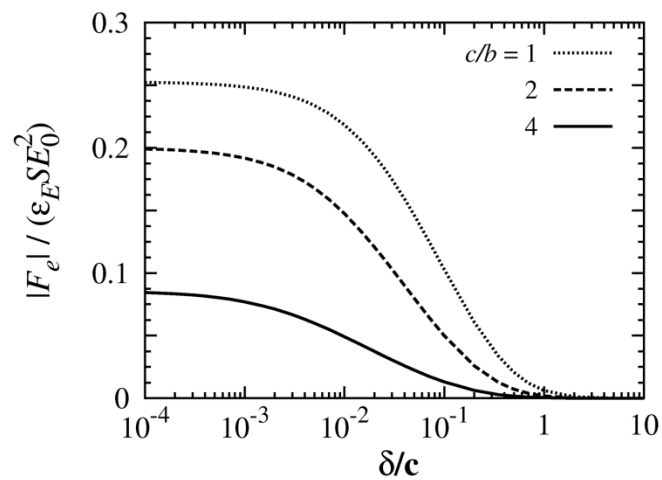
(b) $\mathcal{E} = 4$

Figure 4.24. Magnitude of the electrostatic force on the spheroids as a function of δ/c.

4.3 Summary

In this chapter, the multipole image method is applied to the analysis on electrostatic behavior of the conducting and dielectric spheroids in the axisymmetric configuration. The main results are summarized in the following paragraphs.

For a conducting spheroid on the grounded plane, the maximal field at the top pole increases nonlinearly with the axis ratio of the spheroid. The charge and the force are compared between the spheroids of the same surface area, the same minor axis, or the same major axis. Empirical formulae are proposed to approximate

the maximal field, charge and force with the errors smaller than 2% for the axis ratio between 1 and 32. It is found that the hemispheroidal model can estimate the charge and force on the spheroid with a difference smaller than 10% when $c/b > 3$.

For an uncharged conducting spheroid separated from the grounded plane, the maximal field at the bottom pole increases significantly with decreasing δ/c from 0.1. The relationship between the external electric field and the critical separation of the spheroid where the partial discharge takes place is investigated. This relationship is approximately linear on the logarithmic scales when the normalized separation δ/c approaches zero.

For a charged conducting spheroid above the grounded plane, under the fully charged condition, the maximal field at the top pole hardly varies with the separation from the plane. The force on the spheroid increases gradually with the separation and converges well to the product of the charge and the external field when $\delta/c \geq 10$. The effect of the charge amount on the electric field at the bottom pole and the force is considered. It is found that the bottom-pole field reduces linearly with increasing the charge amount. When $\delta/c > 1$ the force tends to drive a spheroid away from the plane even the spheroid has a slight charge. When $\delta/c \leq 1$, the direction of the force depends on the charge amount.

For the dielectric spheroids having the same c/b, the maximal field at bottom pole and the normalized force are greater for larger ε. For the same ε, the slender spheroids have larger maximal field. However, the force reduces with c/b, except c/b close to 1 when $\varepsilon > 4$. The field and force increases significantly with decreasing δ/c less than 1. With decreasing δ/c close to 0, the force converges more rapidly than maximal field. The force magnitude is less than that on a conducting spheroid in the same configuration.

CHAPTER V

ANALYTICAL RESULTS OF THREE-DIMENSIONAL CONFIGURATION

This chapter presents the analytical results of the three-dimensional configuration in Figure 3.2a. The configuration is a conducting or dielectric spheroid which may be in contact with or separated from a grounded plane under external electric field. The major axis of the spheroid makes a tilt angle with the plane. The analysis focuses on the role of the tilt angle on the force and torque on the spheroid, which are the fundamentals of particle behavior in various applications. The method of multipole images is applied to the electric field calculation. The electrostatic force and torque are determined. For the conducting spheroid, the cases of the grounded and charged floating spheroid are considered. For the dielectric spheroid, only the case of the uncharged spheroid in contact with the plane is taken into account. The calculation results in this chapter are obtained by using the maximal harmonic order not higher than 20 and 40 for the conducting and dielectric spheroids, respectively.

5.1 Conducting spheroid in contact with a grounded plane

5.1.1 Electric field

Figures 5.1a and 5.1b show the distribution of electric field along the spheroid surface on the $y = 0$ plane when $\alpha = 0°$, 15°, 45°, and 90° for $c/b = 2$ and 4, respectively. The electric field is plotted as a function of the normalized arc length l/L, where l is arc length measured from the lower pole and L is the arc length between two poles. For $c/b = 2$ in Figure 5.1a, when $\alpha = 0°$, the electric field is more or less uniform on a wide range of l/L. With increasing α, the field distribution becomes more non-uniform on the surface. The field maximum E_{max} increases and takes place near the upper pole. The position of E_{max} moves to the top pole as α increases to 90°. For larger axis ratio $c/b = 4$, the field behavior in Figure 5.1b is similar to that for $c/b = 2$, but the field is more non-uniform and E_{max} is significantly higher for the same α. The position of E_{max} is clearly noticeable even when $\alpha = 0°$.
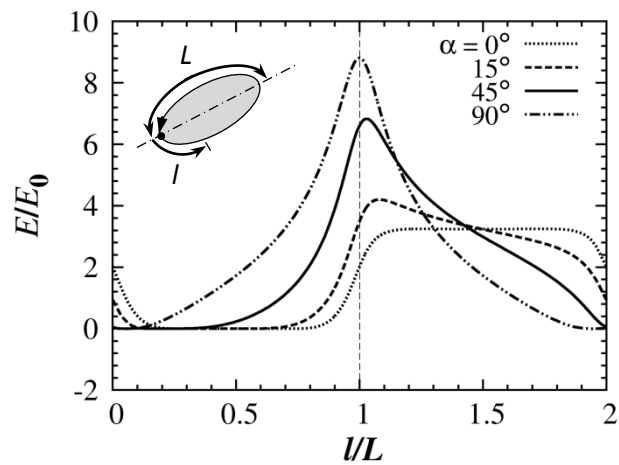
(a) *c/b* = 2
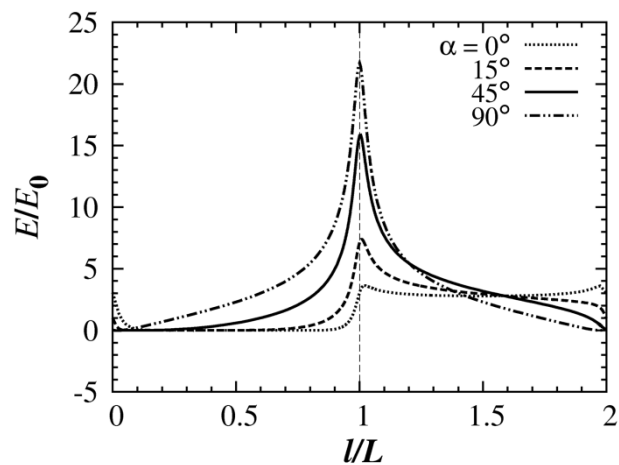
(b) *c/b* = 4

Figure 5.1. Distribution of electric field along the spheroid surface on the *y* = 0 plane with different tilt angles α for two *c/b* values.

Figure 5.2 presents the maximal field as a function of α for *c/b* = 1, 2, 4, and 6. As *c/b* = 1 corresponds to the case of a sphere, the calculation result is a constant of the tilt angle α. The figure clearly shows the field enhancement on the spheroids with increasing α. When the spheroid stands on the plane (α = 90°), the field is intensified by 3, 6.5, and 10 times from that in the lying position (α = 0°) for *c/b* = 2, 4, and 6, respectively.
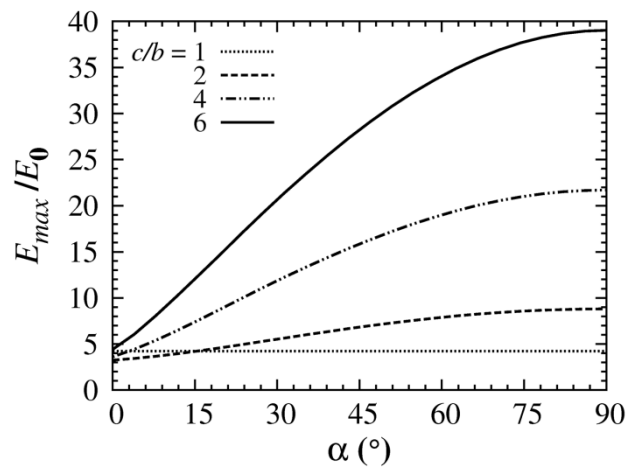
Figure 5.2. Maximal field as a function of angle α for different c/b ratios.

5.1.2 Induced charge

Figure 5.3 presents the variation of the net induced charge Q with the tilt angle α for the spheroids having the same minor semi-axis $b = b_0$. Q is normalized by

$$Q_2 = 4\pi\varepsilon_E b_0^2 E_0. \qquad (5.1)$$

As shown in Figure 5.3, at any angle α the charge is larger on the spheroid having higher c/b, i.e., longer one. The charge on the spheroid is minimal at α = 0°, and increases nonlinearly with α to the maximum at 90°. The ratio of the maximal to minimal charges is 1.5, 2.4, and 3.1 times when c/b = 2, 4, 6, respectively.
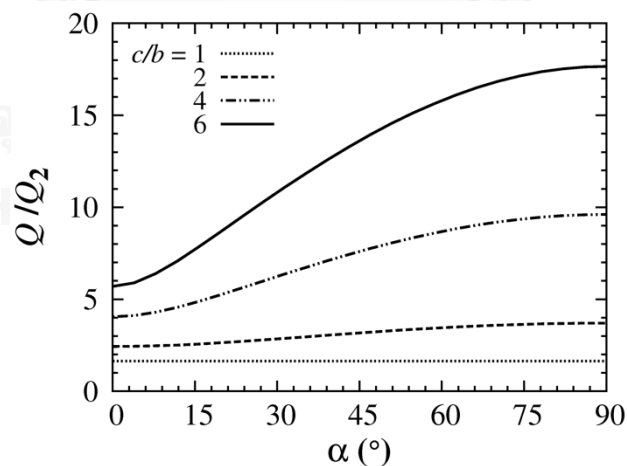
Figure 5.3. Induced charge on spheroid having the same minor semi-axis as a function of α.

5.1.3 Electrostatic force

Figure 5.4 shows the electrostatic stress along the spheroid surface on the $y = 0$ plane for $\alpha = 0°$, 15°, 45°, and 90° when $c/b = 2$. The stress vectors are presented on the same scale for Figures 5.4a-d. Figure 5.4 indicates that the force on the spheroid is governed by the stress on the upper half. The stress becomes concentrated near the higher pole when $\alpha > 0°$. Figures 5.4b and 5.4c imply that the force produces a torque rotating the spheroid about the contact point in the increasing-α direction.

(a) $\alpha = 0°$ (b) $\alpha = 15°$ (c) $\alpha = 45°$ (d) $\alpha = 90°$
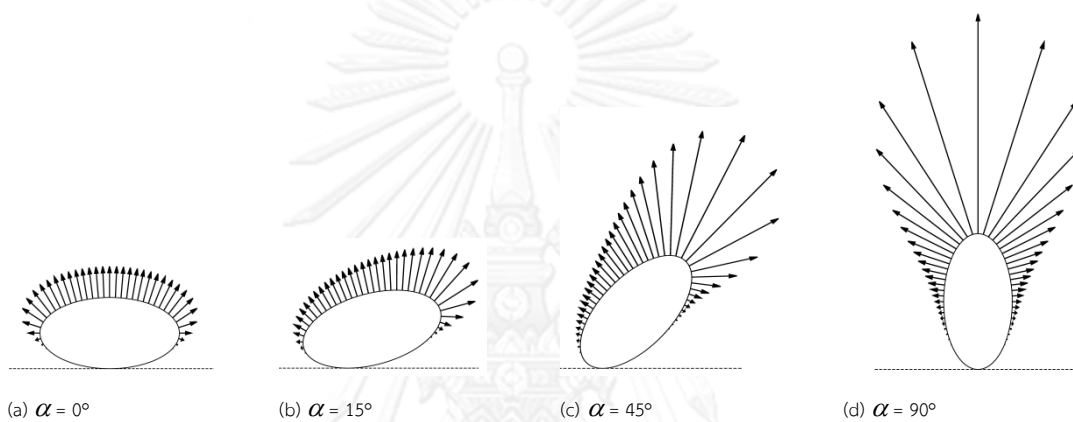
Figure 5.4. Electrostatic stress along the surface on the $y = 0$ plane of the $c/b = 2$ spheroid for different tilt angle α.

Figure 5.5 presents the normalized electrostatic force F_e on the spheroids having the same minor semi-axis $b = b_0$ as a function of the tilt angle α. F_e is normalized by

$$F_2 = 4\pi\varepsilon_E b_0^2 E_0^2. \tag{5.2}$$

It is clear from Figure 5.5 that the variation of the force with α is similar to that of the charge with α in Figure 5.3. That is, the force is minimal at $\alpha = 0°$ and increases nonlinearly with α to the maximum at 90°. The force is stronger on the longer spheroid.

Figures 5.6a and 5.6b show the minimal force F_{min} when $\alpha = 0°$ and the maximal force F_{max} when $\alpha = 90°$ in relation with c/b from 1 to 10, respectively. The minimal force in Figure 5.6a increases linearly with c/b. On the other hand, Figure 5.6b presents F_{max} on the logarithmic scales, as F_{max} is highly intensified with increasing c/b ratio. The following empirical formulae, obtained by curve fitting, may be used for estimating the minimal and maximal forces:
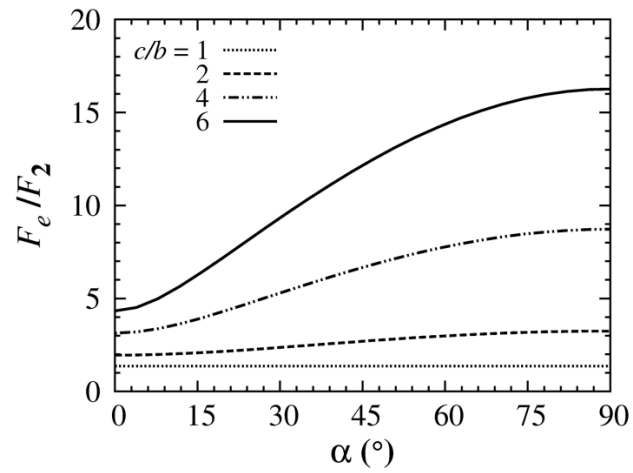
Figure 5.5. Electrostatic force on the spheroids having the same minor semi-axis.
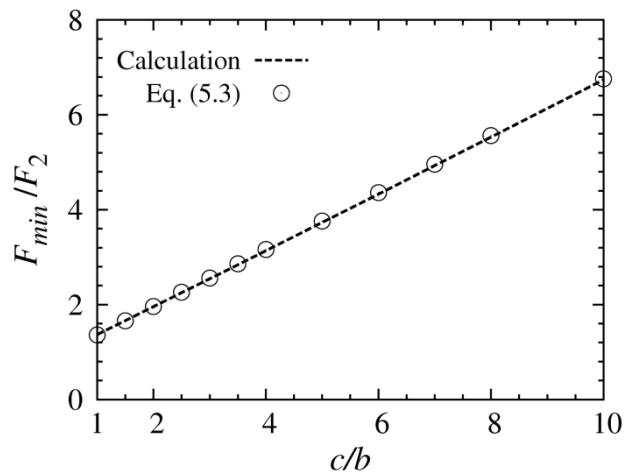
(a) Minimal force
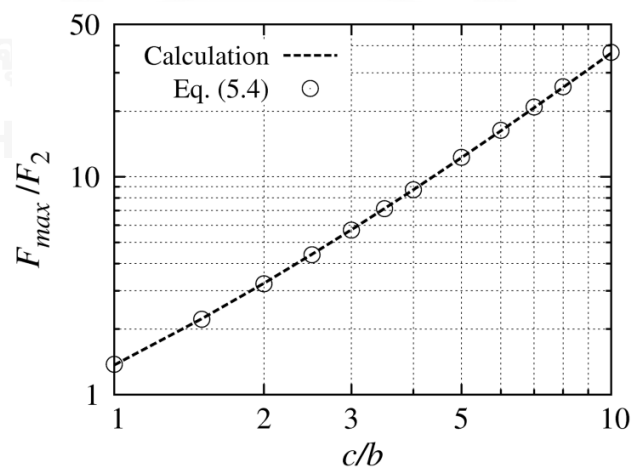
(b) Maximal force

Figure 5.6. Variation of the normalized minimal and maximal forces on the spheroids
having the same minor semi-axis with axis ratio c/b.

$$\frac{F_{min}}{F_2} = 0.6\frac{c}{b} + 0.76 \,, \tag{5.3}$$

$$\frac{F_{max}}{F_2} = 0.63\left(\frac{c}{b} + 0.58\right)^{\sqrt{3}} . \tag{5.4}$$

The approximated values are shown as the symbols in Figure 5.6. Equations (5.3) and (5.4) give F_{min} and F_{max} with error smaller than 1% for c/b between 1 and 10.

5.1.4 Electrostatic torque

Figure 5.7 shows the electrostatic torque $T_{e,\mathbf{p}}$ about the contact point $\mathbf{p}$ on the spheroids having the same minor semi-axis b_0 as a function of α. $T_{e,\mathbf{p}}$ is normalized by $T_0 = F_2 b_0$. $T_{e,\mathbf{p}}$ is zero at $\alpha = 0°$ and $90°$ due to the symmetry of configuration in Figure 3.2. Figure 5.7 shows that $T_{e,\mathbf{p}}$ is always positive for α between $0°$ and $90°$, i.e., in the increasing-α direction. Maximum of $T_{e,\mathbf{p}}$ is approximately at $\alpha = 45°$. Quadratic (parabolic) relationships are plotted in comparison with calculation results in Figure 5.7, and only small difference can be seen for $\alpha > 45°$. For the same α, the torque is greater on the spheroid having larger c/b (longer spheroid).

Figure 5.8 shows the variation of the maximal torque T_{max} with c/b from 1 to 10 on logarithmic scales. When $c/b \geq 2$, we may approximate T_{max} by

$$T_{max}/T_0 = 0.6(c/b)^{2.6} . \tag{5.5}$$

The approximated values by equation (5.5) are compared with the calculation results in Figure 5.8.
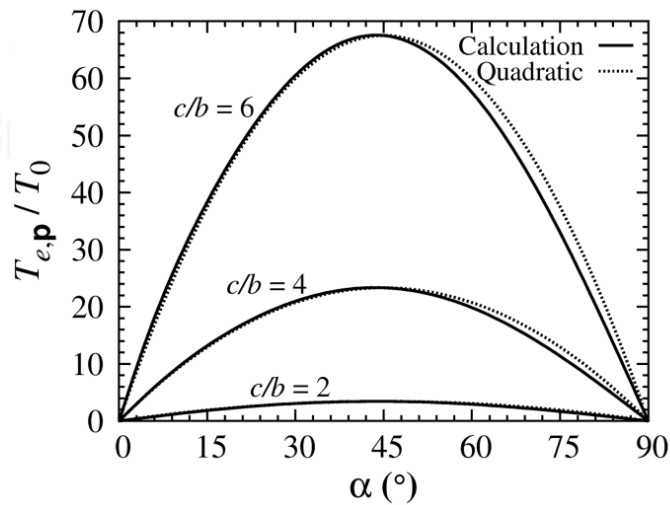
Figure 5.7. Electrostatic torque about $\mathbf{p}$ on the spheroids as a function of α.
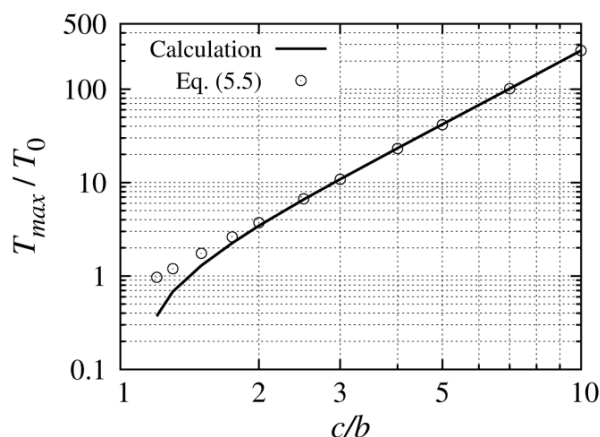
Figure 5.8. Maximal electrostatic torque about **p** on the spheroid in relation with *c/b*.

5.1.5 Electromechanical behavior with gravitational effects

This section deals with the electromechanical behavior of the conducting prolate spheroid in contact with the plane when the gravitational force F_g is taken into account. F_g does not only restrain the spheroid from lifting motion, but also contributes to torque $T_{g,\mathbf{p}}$ about the contact point **p**. For α = 0° or 90°, the spheroid is lifted from the grounded plane without rotation if F_e is greater than F_g. For other α values, the behavior of the spheroid is more complicated due to nonzero total torque $T_{tot,\mathbf{p}}$ that includes the gravitational torque.

a) Total torque on spheroid

As an example, consider aluminum spheroidal particles having the same *b* = 0.25 mm and different *c*. Figure 5.9 presents $T_{g,\mathbf{p}}$ on the aluminum particles as a function of α for *c* = 0.5, 1.0, and 1.5 mm. As F_g is constant for a particle, $T_{g,\mathbf{p}}$ magnitude follows the characteristic of *d* defined in equation (3.9). We can see from Figure 5.9 that $T_{g,\mathbf{p}}$ increases with increasing α from 0°, and reaches the peak at α considerably smaller than 45° and then decreases to zero at 90°. The angle of maximal $T_{g,\mathbf{p}}$ reduces with increasing the particle length.

Figure 5.10 shows the total torque $T_{tot,\mathbf{p}}$ on the aluminum particle of *b* = 0.25 mm and *c* = 1 mm for E_0 = 2, 3, 4, and 6 kV/cm. For small E_0 = 2 kV/cm, $T_{g,\mathbf{p}}$ is predominant over $T_{e,\mathbf{p}}$ for the range 0° < α < 90°, resulting in negative $T_{tot,\mathbf{p}}$ (reducing-α direction). On the other hand, for large E_0 = 6 kV/cm, $T_{e,\mathbf{p}}$ is predominant and $T_{tot,\mathbf{p}}$ is positive. For intermediate E_0 values, $T_{tot,\mathbf{p}}$ is negative at small α and becomes positive when α is greater than critical tilt angle α_c. The critical angle in Figure 5.10 decreases when E_0 increases from 3 to 4 kV/cm.
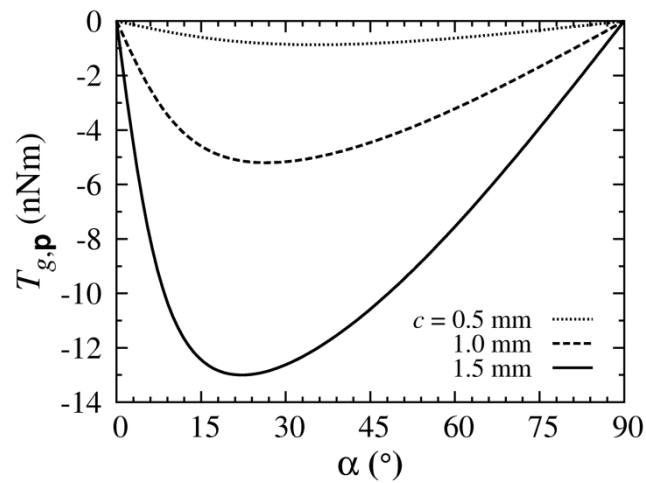
Figure 5.9. Gravitational torque about the contact point **p** on aluminum spheroidal particles having b = 0.25 mm.
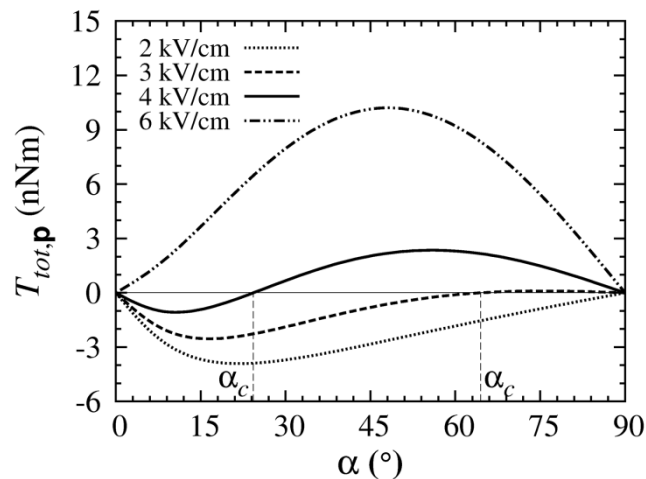
Figure 5.10. Total torque on an aluminum spheroidal particle of b = 0.25 mm and c = 1 mm as a function of α for different E_0 values.

b) Classification of electromechanical behavior

From the aforementioned results, we can deduce that for tilt angle 0° < α < 90°, the conducting spheroidal particle may be subject to (i) total torque about contact point whose direction depends on field strength and (ii) lifting force if the field is strong enough. Figure 5.11 presents the critical field E_R and E_L of the aluminum particle having b = 0.25 and c = 1 mm (c/b = 4) for the rotating ($T_{tot,\mathbf{p}}$ = 0) and lifting ($F_e = F_g$) conditions, respectively, as a function of α.

Assume that an aluminum particle is at angle α_0, possibly caused by mechanical operation or disturbance, the electromechanical behavior may be classified as follows:

1. $E_0 < E_R(\alpha_0)$: the particle is rotated by $T_{tot,\mathbf{p}}$ to the lying orientation ($\alpha = 0°$).
2. $E_R(\alpha_0) < E_0 < E_L(\alpha_0)$: the torque $T_{tot,\mathbf{p}}$ rotates to increase α.
   2a. If $E_0 < E_L(90°)$: the particle obtains the standing orientation ($\alpha = 90°$) without lifting.
   2b. If $E_0 > E_L(90°)$: the particle rotates and then lifts.
3. $E_0 > E_L(\alpha_0)$: the particle is lifted from the plane and may be rotated as $E_0 > E_R(\alpha_0)$.

The regimes of electromechanical behavior explained above are indicated in Figure 5.11 by the circle numbers. Note that the particle can be rotated from the lying position ($\alpha = 0°$) with little mechanical disturbance when $E_0 > E_R(0°)$, by which

$$\frac{dT_{tot,\mathbf{p}}}{d\alpha} > 0. \tag{5.6}$$

Moreover, if $E_R(0°)$ is greater than $E_L(90°)$, the particle is then lifted from the electrode when α reaches a critical angle between 0 and α_1, where $E_L(\alpha_1) = E_R(0°)$. It is noticed that the minimum field that can lift the particle is $E_L(90°)$. The E_R and E_L characteristics imply that this minimum field $E_L(90°)$ can lift a particle making angle $\alpha_0 \geq \alpha_2$, where $E_R(\alpha_2) = E_L(90°)$. Figure 5.11 shows α_1 and α_2 for the aluminum spheroidal particle ($b = 0.25$ mm and $c = 1$ mm).
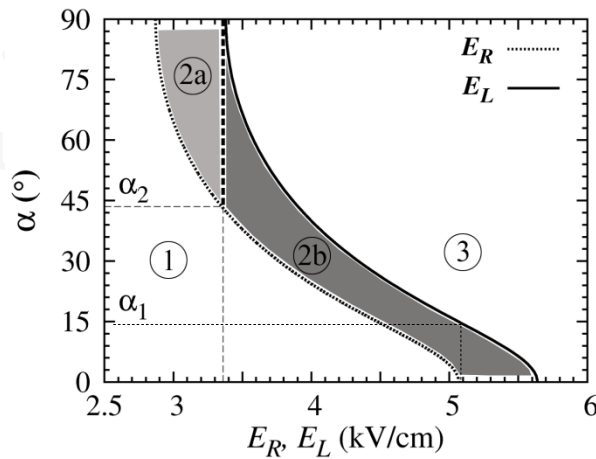
Figure 5.11. Critical electric field E_R for rotating and E_L for lifting the aluminum spheroidal particle having $b = 0.25$ mm and $c = 1$ mm.

c) Effect of the major-to-minor axis ratio of the spheroidal particle

Figure 5.12 presents the characteristics of E_R and E_L of an aluminum particle for b = 0.25 mm and different c/b values. The figure shows that $E_R(0°) < E_L(90°)$ for the small axis ratio $c/b < 1.45$ (sphere-like particle). For larger c/b values, $E_R(0°) > E_L(90°)$. That is, a wire-like particle tends to be lifted from the plane after rotated from the lying position by the electric field.

The critical angles α_1 and α_2 are calculated for the particles having b = 0.1, 0.25, and 0.5 mm. Figure 5.13 presents α_1 and α_2 as a function of c/b for the particles. It is clear from the figure that the angles mainly depend on the axis ratio not the minor axis. With c/b increasing from 1.45, α_1 decreases but α_2 increases.

(a) c/b = 1.2

(b) c/b = 1.45

(c) c/b = 2

(d) c/b = 6
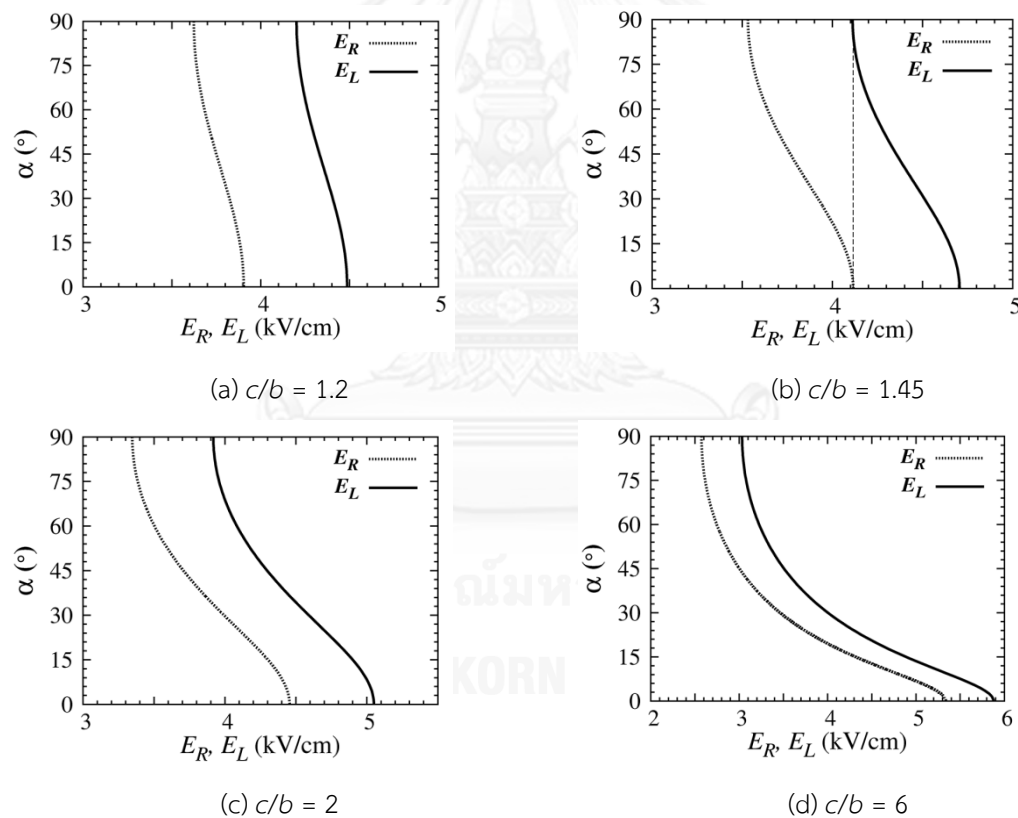
Figure 5.12. Rotating and lifting field of aluminum spheroidal particles having the same b = 0.25 mm for different c/b values.
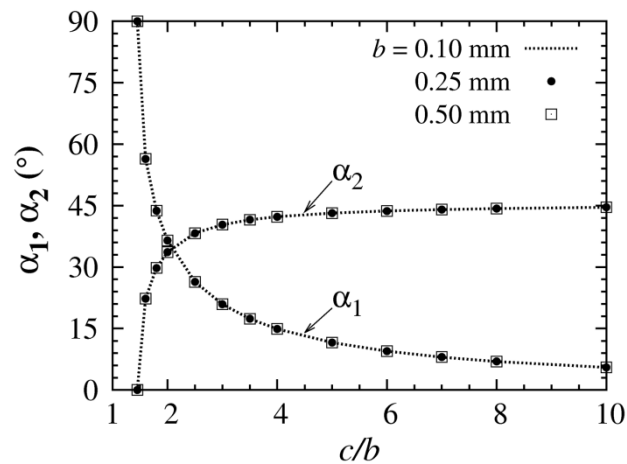
Figure 5.13. Angle α_1 and α_2 as a function of axis ratio c/b for the aluminum particles.

d) Effect of the material of the spheroidal particle

Next, consider the effect of the material of the particle on the characteristics of the rotating field E_R and the lifting field E_L. The stainless steel is considered here as an example. The calculation results of E_R and E_L for a particle having $b = 0.25$ mm and $c = 1$ mm ($c/b = 4$) are presented by symbols in Figure 5.14. The field in the figure is normalized by square root of mass density. The figure also shows the calculation results of E_R and E_L for an aluminum particle having the same size for comparison. It is obvious from Figure 5.14 that the characteristics of E_R and E_L with respect to α are independent of the mass density of the particle. This is because that E_R and E_L are a function of the square root of the mass density, as derived in Appendix B.

Figure 5.15 shows the α_1 and α_2 values calculated for the spheroidal particles having $b = 0.25$ mm for the aluminum and stainless-steel materials. We can conclude from Figures 5.13 and 5.15 that the critical angles α_1 and α_2 are independent of the mass density and the size of the particle, provided the axis ratio c/b is invariant.
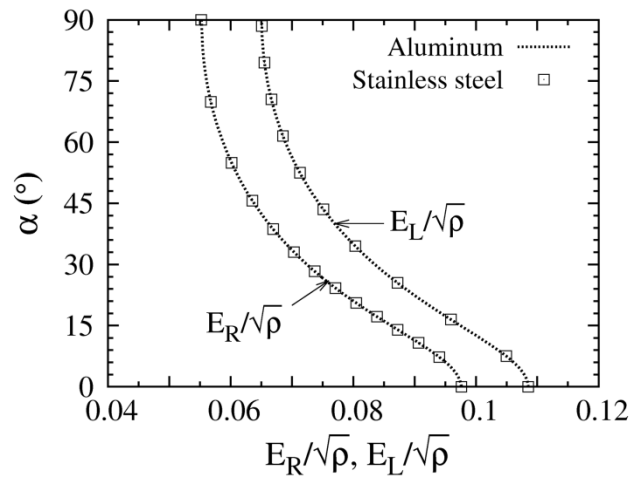
Figure 5.14. Rotating and lifting field of aluminum and stainless-steel spheroidal particles with b = 0.25 mm and c = 1 mm.
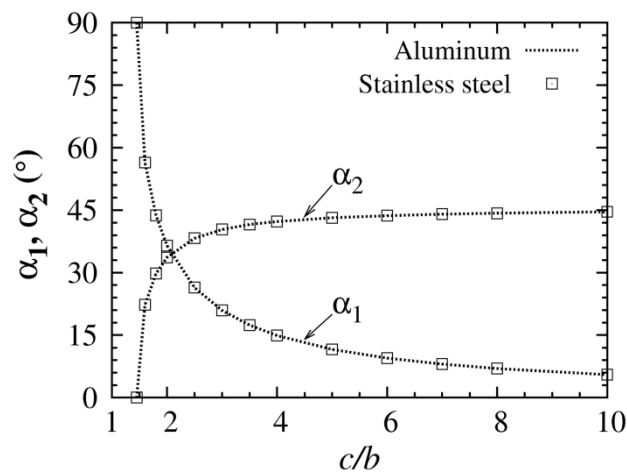
Figure 5.15. Angle α_1 and α_2 for spheroidal particles having b = 0.25 mm with different materials.

e) Lifting and rotating electric field for lying condition (α = 0°)

Figure 5.16 shows the lifting field E_L at α = 0° as a function of axis ratio c/b varied from 1 to 10 for aluminum particles having b = 0.1, 0.25, and 0.5 mm. As shown in Figure 5.16, E_L increases gradually with c/b. The lifting field increases by a factor of about 1.4 when c/b increases from 1 to 10 for all three b values. For $c/b >$ 10, E_L in Figure 5.16 apparently approaches an upper limit. E_L is greater for bigger particle. Note that we can modify Figure 5.16 for other material by scaling the ordinate with the square root of ratio of the particle mass density to 2,700 kg/m^3. Figure 5.17 shows the ratio E_R/E_L at α = 0° of the particles with c/b between 1 and

10. The ratio increases gradually with *c/b*, and is between 0.86 and 0.92 for the considered range *c/b*. The ratio in Figure 5.17 does not depend on the minor semi-axis *b*.
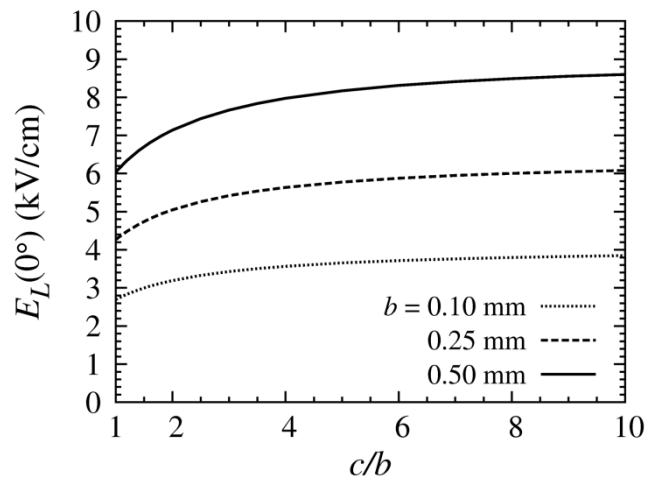
Figure 5.16. Lifting field E_L at α = 0° of aluminum particles with different *b*.
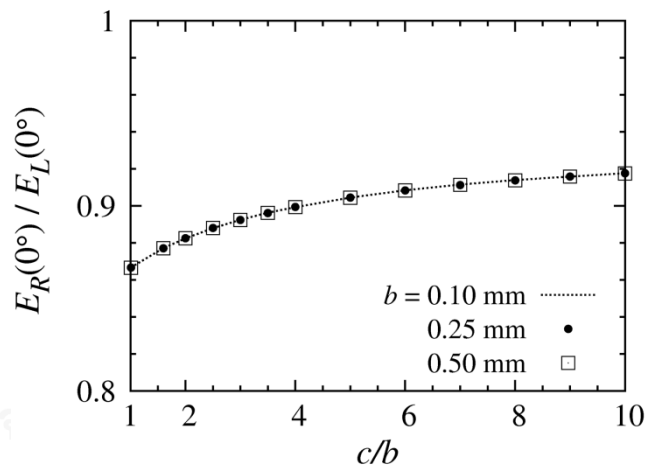
Figure 5.17. Ratio of E_R to E_L at α = 0° of aluminum particles with different *b*.

5.2 Fully charged conducting spheroid above a grounded plane

This section considers the variation of the electrostatic force and torque on a floating conducting spheroid with tilt angle α and separation δ. For any separation δ, the charge amount on a spheroid at tilt angle α_l is assumed to be that on the spheroid in contact with the grounded plane at the angle α_l, referred as "the fully charged condition". The variation of the charge amount on a grounded spheroid with α_l was already presented in Figure 5.3. As the spheroid is separated from the plane, the

torque about the spheroid center **o** (center of mass) is considered. Note the gravitational torque about **o** is zero; therefore, the total torque about **o** is contributed only from the electrostatic torque. The effect of the charge reduction on the force and torque is discussed in Chapter VII.

Figures 5.18a and 5.18b present the variation of the force with respect to α varied from 0° to 90° for c/b = 2 and 4, respectively. The force is normalized by F_2 in equation (5.2). The calculated force is given for normalized separation δ/c = 0.1, 1, and 10. Besides, the case of the grounded spheroid (δ = 0) is shown by the dotted line for comparison. As shown in Figure 5.18, the variation of the force with α for the floating spheroid ($\delta \neq 0$) is similar to that of the grounded spheroid (δ = 0). The difference between the curves in the figures does not depend much on α. Figure 5.18 indicates that the force enhances a little with the increase of the separation.
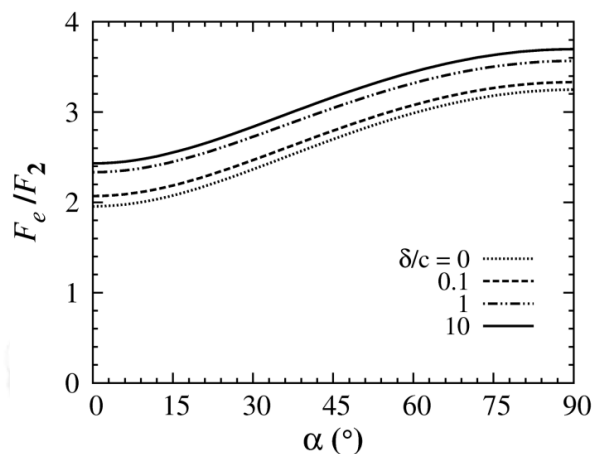
(a) c/b = 2
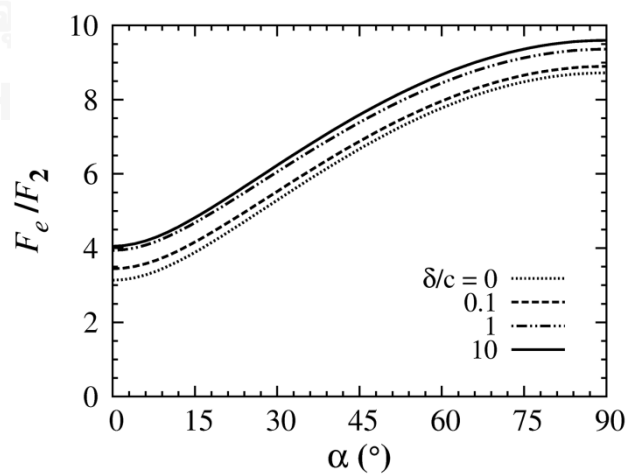
(b) c/b = 4

Figure 5.18. Electrostatic force on fully charged spheroids with different δ.

The calculation result of the torque $T_{e,\mathbf{o}}$ for c/b = 2 and 4 is shown in Figures 5.19a and 5.19b, respectively. The torque is normalized by $T_0 = F_2 b_0$. It is clear from Figure 5.19 that for any value of δ, $T_{e,\mathbf{o}}$ varies roughly as a parabolic function of tilt angle α and maximal at α about 45°. This behavior is similar to that of the torque $T_{e,\mathbf{p}}$ about the contact point $\mathbf{p}$ of a grounded spheroid presented in Figure 5.7. The maximum of $T_{e,\mathbf{o}}$ is much smaller than that of $T_{e,\mathbf{p}}$. As shown in Figure 5.19, the torque is greater for larger separation and higher c/b.
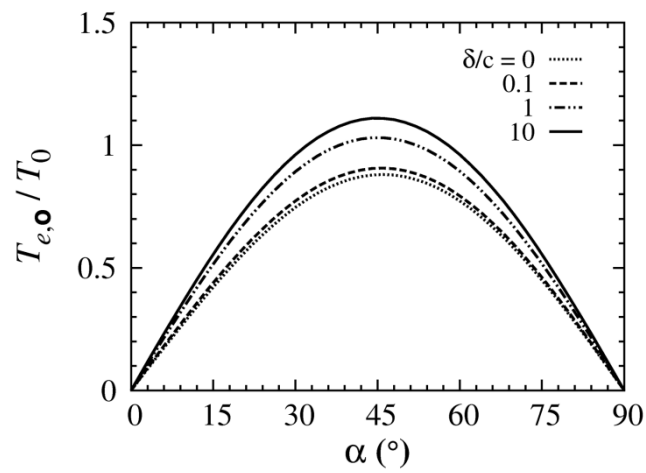
(a) c/b = 2
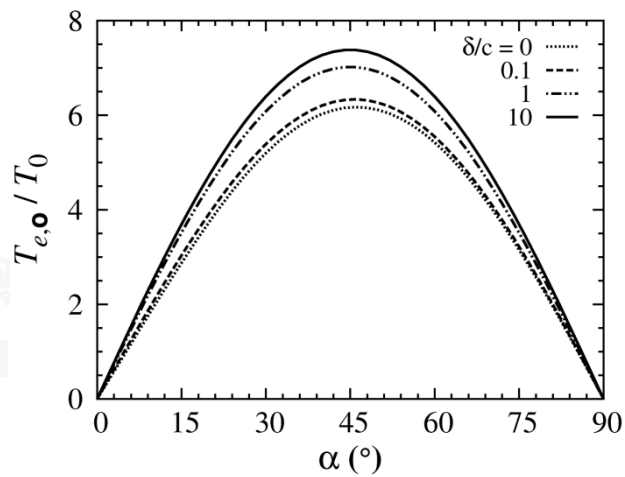
(b) c/b = 4

Figure 5.19. Electrostatic torque about the spheroid center $\mathbf{o}$ on fully charged spheroids with different separations for two c/b values.

5.3 Uncharged dielectric spheroid in contact with a grounded plane

As presented in Appendix A, the use of a large number N of harmonics is necessary to obtain the high accuracy in the calculation result for the dielectric spheroid, especially for high axis ratio c/b and dielectric-constant ratio ε. However, the 3D calculation for dielectric spheroids has been done by using N less than 50. Therefore, only the case of c/b = 2 and ε = 2, in which the results converge well with $N \leq 50$, is given here.

5.3.1 Electric field

Figure 5.20 shows the magnitude of the electric field E^{out} along the spheroid surface on the y = 0 plane in the exterior of the spheroid when α = 0°, 15°, 45°, and 90°. The electric field is plotted as a function of the normalized arc length l/L. The electric field in Figure 5.20 is maximal at l/L = 0.5, 0.3, 0.1, and 0 for α = 0°, 15°, 45°, and 90°, respectively, which are the contact point **p** between the spheroid and the plane. It is clear from Figure 5.20 that the maximal field increases with α. When α = 90°, E^{out} maximum is about 0.4 times of that for the grounded conducting spheroid having the same c/b ratio (in Figure 5.1a).
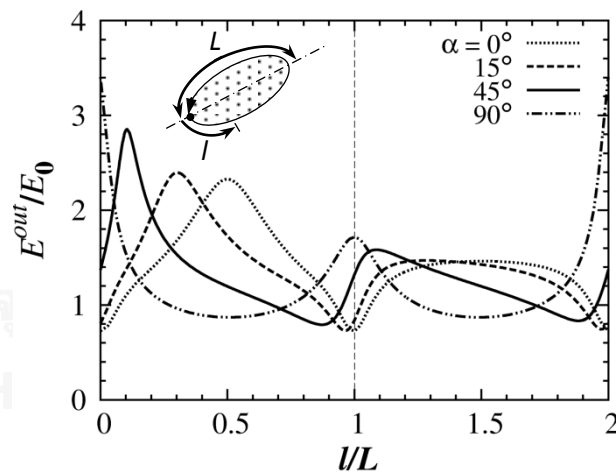
Figure 5.20. Distribution of electric field along the spheroid surface on the y = 0 plane in the ambient-medium side.

5.3.2 Electrostatic force

Figure 5.21 presents the distribution of the electrostatic stress along the spheroid surface on the y = 0 plane for α = 0°, 15°, 45° and 90°. We can see from Figure 5.21 that the force is governed by the stress on lower half. The force is considerably concentrated around the contact point **p**, especially for higher α.

In contrast to a conducting spheroid, a dielectric spheroid adheres to the grounded plane by the electrostatic force, irrespective of external field direction. The normalized electrostatic force on the dielectric spheroid is given in Figure 5.22. The force in Figure 5.22 is maximal at α = 0° and decreases with α to the minimum at 90°. This is opposite to the behavior of the force on a conducting spheroid (see Figure 5.5). In comparison with the conducting spheroid having the same size, the average magnitude of the force on the dielectric spheroid in Figure 5.22 is smaller by about 50 times. The maximal-to-minimal force ratio approximately has the same value, 1.7.

(a) α = 0°   (b) α = 15°   (c) α = 45°   (d) α = 90°
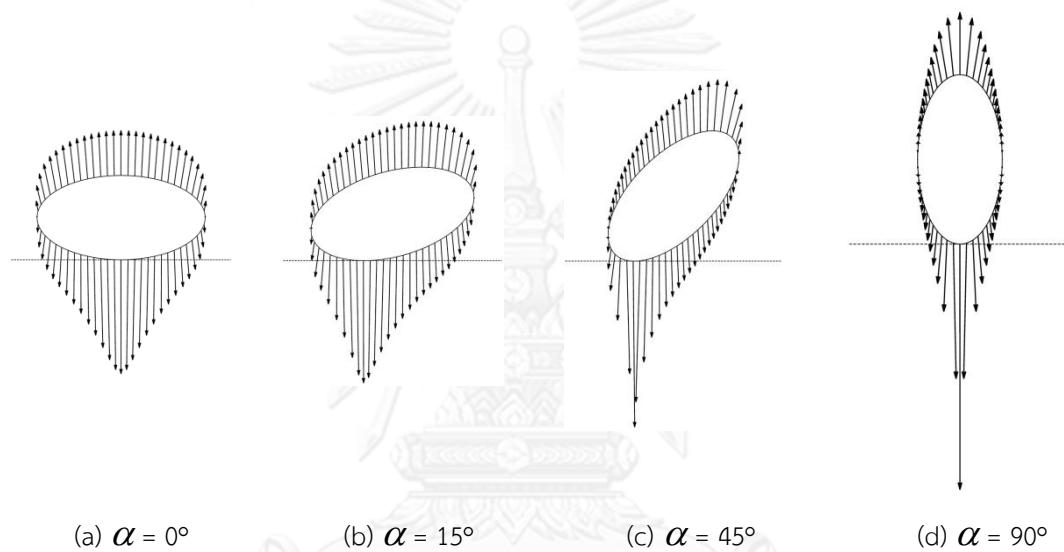
Figure 5.21. Electrostatic stress along the spheroid surface on the y = 0 plane for different tilt angles.
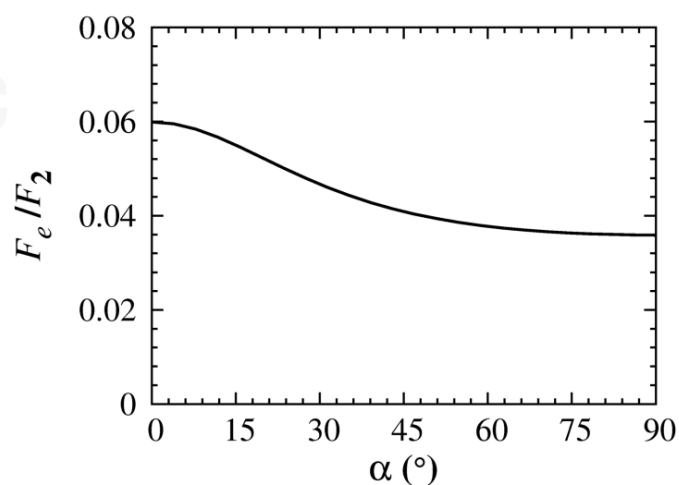
Figure 5.22. Variation of force magnitude on the dielectric spheroid with α.

5.3.3 Electrostatic torque

Figure 5.23 presents the normalized electrostatic torque $T_{e,\mathbf{p}}$ about the contact point $\mathbf{p}$ as a function of α. The torque in Figure 5.23 is positive. This means that the spheroid tends to rotate in increasing-α direction, similarly to the case of the conducting spheroids. The positive values of the torque can be verified by the distribution of the stress in Figure 5.21. That is, for α = 15° and 45° in Figure 5.21, the torque about $\mathbf{p}$ resulted from the stress near higher pole becomes predominant. The torque in Figure 5.23 is maximal at α about 45°. The maximal value is about 80 times smaller than that of the conducting spheroid with the same size.
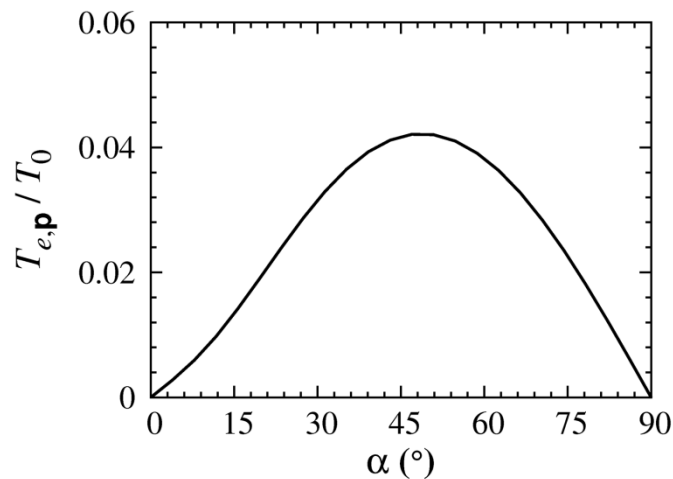
Figure 5.23. Electrostatic torque on the dielectric spheroid as a function of α.

To consider the effect of the gravitational force on the electromechanical behavior of the dielectric spheroid, a Teflon spheroidal particle with b = 0.5 mm and c = 1 mm is taken into account here as an example. The Teflon has the mass density of about 2,200 kg/m^3 and the permittivity of about 2. Figure 5.24 shows the total torque $T_{tot,\mathbf{p}}$ on the particle for E_0 = 20, 40, 60, and 100 kV/cm. Note that, 100 kV/cm is hardly to find in practical equipments. It is considered here for reference. We can see from the figure that the variation of the torque with α and E_0 is similar to that in Figure 5.10 for a conducting spheroid. $T_{tot,\mathbf{p}}$ in Figure 5.24 is negative for E_0 = 20 kV/cm, and positive for E_0 = 100 kV/cm. For E_0 values up to 60 kV/cm, the torque is negative when α is smaller than a critical tilt angle. Figure 5.25 presents the critical field E_R for the rotating condition ($T_{tot,\mathbf{p}}$ = 0). Hence, the stable orientation of the particle on the plane is either lying or standing position.
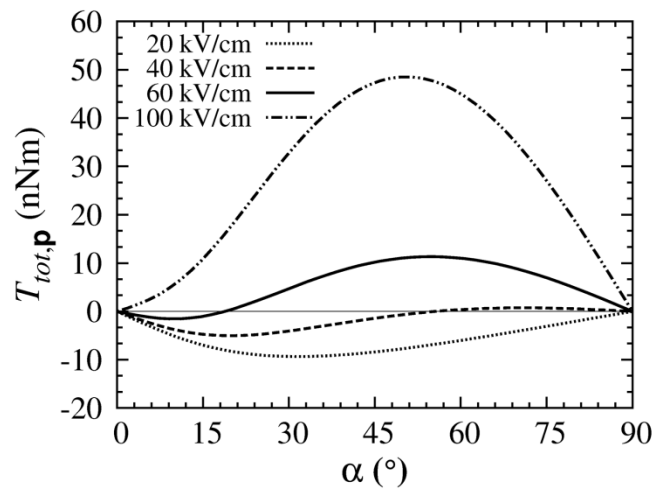
Figure 5.24. Total torque on a Teflon spheroidal particle with b = 0.5 mm and c = 1 mm as a function of α for different E_0 values.
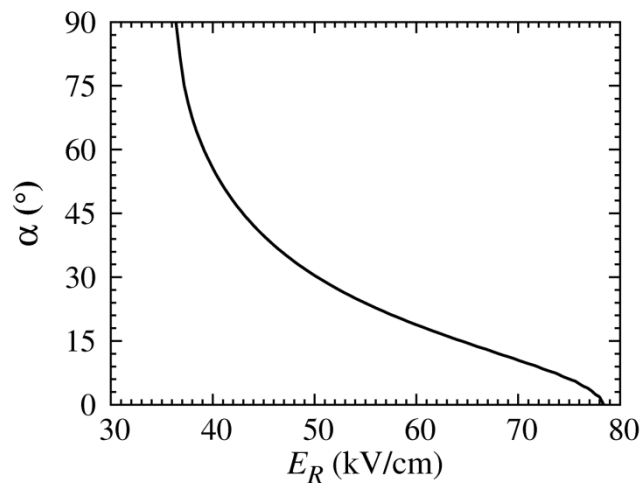
Figure 5.25. Critical electric field E_R for rotating the Teflon spheroidal particle having b = 0.5 mm and c = 1 mm.

5.4 Summary

This chapter applies the method of multipole images to the analysis on electromechanics of a conducting or dielectric spheroid in a three-dimensional configuration. The results obtained from the analysis can be summarized as follows:

For a grounded conducting spheroid, the maximal field takes place at or near the higher pole of the spheroid for nonzero tilt angles. The electrostatic force on the spheroids having the same minor axis increases nonlinearly with major axis and α. The force is minimal and maximal when the spheroid lies and stands on the plane,

respectively. Empirical formulae are proposed to estimate the minimal and maximal forces with error smaller than 1% for the major-to-minor axis ratio between 1 and 10. The electrostatic torque is in the increasing-α direction, and it is magnified with increasing α from 0 to about 45°, and then reduces to zero at α = 90°. The torque variation may be estimated by a quadratic relationship. When the gravitational force of a spheroidal particle is taken into account, its electromechanical behavior can be classified into three regimes, depending on the externally applied field and the tilt angle. The presence of the electrostatic torque enhances the probability of a spheroidal particle to be lifted from the grounded plane by the electric field.

For a fully charged conducting spheroid above the grounded plane, the variation of the electrostatic force and torque about the center **o** with respect to α is similar to that when the spheroid is in contact with the plane. The force and torque increase with increasing the separation between the spheroid and the plane. However, the increase is not quite significant. The torque about the center **o** of the floating spheroid is smaller than that about the contact point **p** of the grounded spheroid.

For the uncharged dielectric spheroid with c/b = 2 and ε = 2 in contact with the plane, the electric field is maximal at the contact point **p** for all α values. The force is maximal at α = 0°, and reduces nonlinearly with α to the minimum at α = 90°. The torque about **p** always tends to rotate the spheroid to the standing position. The magnitude of the force and torque is significantly smaller in comparison with the conducting spheroid having the same size.

CHAPTER VI

EXPERIMENTAL SETUP AND APPARATUS

In this dissertation, the author experimentally studied the movement behavior of conducting prolate spheroidal and wire particles with different ending profiles under a uniform electric field. Besides, the lifting electric field and the corona discharge triggered by the particles were also measured. This chapter presents the experimental setup, apparatus, and samples. The experimental procedure is also explained in this chapter.

6.1 Test particles

Metallic particles in actual gas insulated equipments have a variety of sizes and shapes. These particles are possibly produced in the manufacturing process or in the operation. The shape of the conducting particles commonly found in the equipments was non-spherical, rather elongated or needle. In this dissertation, prolate spheroidal and cylindrical (wire) particles are used in the experiments. The experimental results on the prolate spheroidal particles were used for comparison with the analytical results in Chapter V. The wire particles are supposed to produce a higher degree of field intensification than the spheroidal ones. Therefore, they are more susceptible to corona discharge.

6.1.1 Prolate spheroidal particles

Prolate spheroidal particles were made to a special order (Mitsuwa Science Factory). The particles were made from aluminum. Two sizes of the particles were used. The major axis of the particles was 4 mm. The minor axis was 1 mm for the small particles and 2 mm for the large particles, as shown in Figure 6.1. Three samples were used for each size. Table 6.1 shows the geometrical and electrical parameters of small and large particles. The E_R, E_L, and E_{max}/E_0 values are determined by the analysis in Chapter V. Under the standing orientation (α = 90°), the maximal field at the top pole of the small particle was greater than that of the large particle by a factor of about 2.5 times.

(a) Small particle   (b) Large particle
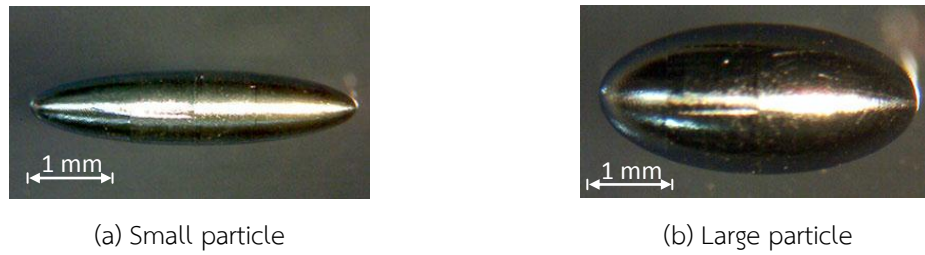
Figure 6.1. Two kinds of prolate spheroidal particles used in this dissertation.

Table 6.1. Details of the spheroidal particles.

Parameter	Symbol	Small particle	Large particle
Minor axis (mm)	$2b$	1	2
Major axis (mm)	$2c$	4	4
Axis ratio	c/b	4	2
Surface area (mm^2)	S	10.1	21.5
Volume (mm^3)	V	2.1	8.4
Mass (mg)	m	5.7	22.6
Rotating field when α = 0° (kV/cm)	E_R	7.2	8.9
Lifting field at when α = 0° (kV/cm)	E_L	8.0	10.1
Maximal field ratio at top pole when α = 90°	E_{max}/E_0	21.7	8.8

6.1.2 Wire particles

Wire particles were cut from aluminum wires of diameter 0.5 mm (AL-011385, Nilaco) by diagonal pliers. The length of the particles was 2 and 4 mm. The particle ends were (i) left unfurnished to be sharp, (ii) rounded by sandpaper, or (iii) coated with a dielectric. Figure 6.2 shows the images of the particles ends. The rounded ends are shown in Figure 6.2a. For the uncoated sharp ends, the particles were cut with two slanting angles, as shown in Figures 6.2b and 6.2c. The ending profiles in Figure 6.2c are sharper than those in Figure 6.2b, and hereafter we refer to the profile as "very sharp end". Under an applied voltage, the degree of corona discharge (if exists) at the particle ends is supposed to be lowest at the rounded end and highest at the very sharp end. Also note that the field at the tips also depends on the particle orientation on the electrode. Comparing the orientations in Figure 6.3, the electric field is higher at the sharp ends when the tip is well separated from the electrode (Figure 6.3a) than when the tip is in contact or close to the electrode (Figure 6.3b).

The dielectric coating was applied to the particle end for suppressing the corona discharge there. The dielectric material was a kind of varnish obtained from a local supplier. The images of the coated ends are given in Figures 6.2d and 6.2e. The dielectric coating is thicker in Figure 6.2e, and is supposed to suppress the corona discharge more efficiently. This ending profile is referred as "thickly-coated end". The average thickness at the tip was about 0.05 mm and 0.15 mm for Figure 2d and 2e, respectively. A preliminary experiment was carried out to estimate the attractive force between the coating layer and electrode (including coating weight). The force was about 7.3 μN (equal to the weight of 1.4-mm long aluminum wire particles).

Table 6.2 summarizes the combination of the particle ends used in the experiments. The particle types (such as R-R, S-S, etc.) are referred to the particles hereafter for convenience. The particles can be classified into two main categories: uncoated particles and particles with dielectric coating at one (rounded) end.

| (a) Rounded end | (b) Sharp end | (c) Very sharp end | (d) Coated end | (e) Thickly-coated end |
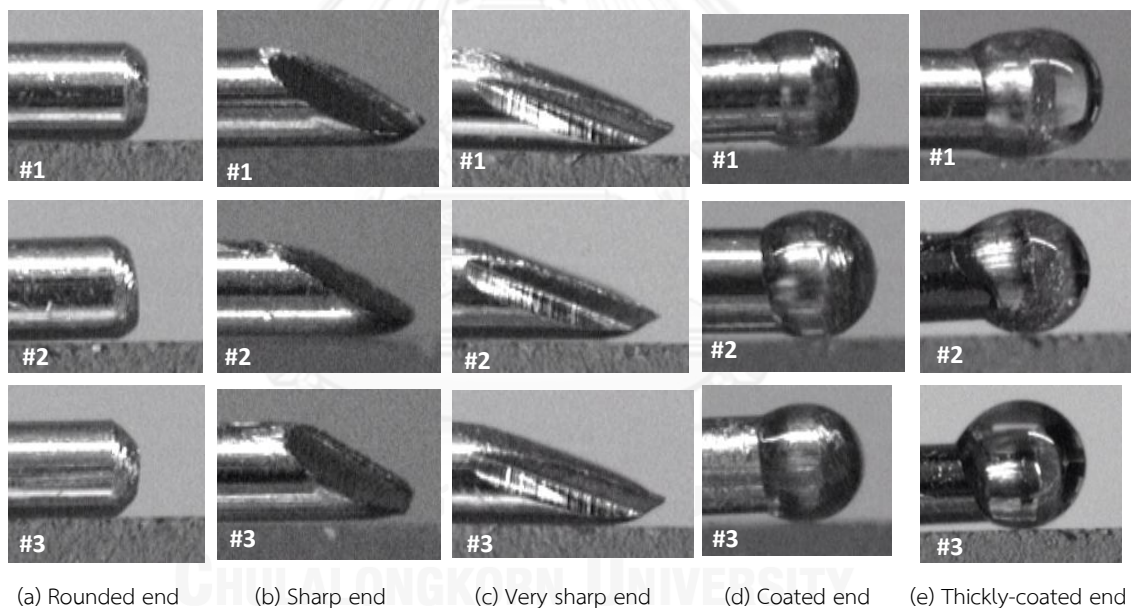
Figure 6.2. Images of particle ends (not on the same scale).
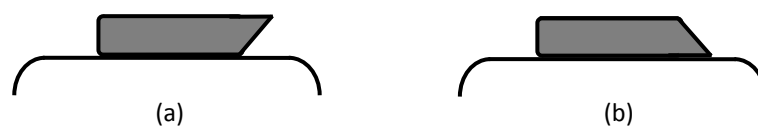
Figure 6.3. A wire particle with different orientations on an electrode.

Table 6.2. Types of wire particles used for experiments.

Particle type	Description	Profile
R-R	Two rounded ends	
S-S	Two sharp ends	
R-S	Rounded end and sharp end	
R-SS	Rounded end and very sharp end	
C-R	Coated end and rounded end	
C-S	Coated end and sharp end	
CC-S	Thickly-coated end and sharp end	

6.2 Experimental setup

Figure 6.4 shows the schematic diagram of the experimental setup for the observation of the particle movement and for the measurement of the corona discharge. The major components were a DC high voltage power source, an electrode system, and observation and measurement equipments. The high-voltage (HV) electrode was connected to the power source through a 10 MΩ resistor. The potential at the HV electrode was measured by using a resistive voltage divider. The other electrode was grounded. To measure the corona discharge on the particle, a 50 Ω resistor was connected in series with the grounded electrode. The movement of the particle between the electrodes was recorded with a digital video camera with a frame rate of 1000 fps. The video images were subsequently transferred to a computer for analyzing the particle behavior. All experiments were carried out in air. The pressure used in the experiments was mostly atmospheric one. In some cases, the pressure was 0.2 MPa pressurized by using a test chamber.
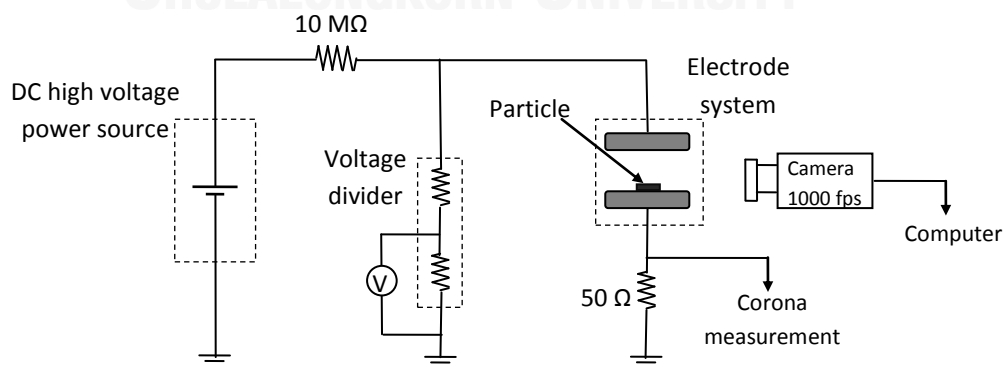
Figure 6.4. Schematic diagram of experimental setup.

6.3 DC high voltage sources

The magnitude of the applied voltage was up to 20 kV. The DC high voltage was generated from: (i) a function generator associated with a high voltage amplifier, (ii) a HV test transformer connected to a rectifier circuit, or (iii) a DC high voltage generator.

6.3.1 Combination of a function generator and a HV amplifier

The DC applied voltage was generated by using a function generator (AFG3021B, Tektronix) and a high-voltage amplifier (610E, Trek). The function generator could generate arbitrary electrical waveforms with a frequency 0–25 MHz and peak value up to ±10 V. The amplifier magnified the input signal to 0 to ±10 kV with output current from 0 to ±200 μA. These equipments were applied to the experiments about the movement of the wire particles.

6.3.2 Combination of a HV test transformer and a rectifier circuit

For the experiments on the spheroidal particles, the voltage greater than 10 kV was needed. For this case, the DC voltage was obtained by using a 220/100 kV, 50 Hz high-voltage test transformer and a 2-stage, Cockcroft–Walton rectifier circuit, as shown in Figure 6.5. An AC voltage was applied to the transformer through a control panel and an autotransformer. These equipments could deliver a voltage up to 100 kV for both polarities with rated current of ± 50 mA.

6.3.3 ±100 kV DC high voltage power supply

The corona discharge was measured at the high voltage laboratory of the University of Tokyo, Japan. The voltage was applied by using positive and negative DC high voltage power supplies (MODEL-502, Nissin). The rated voltage and current are 100 kV and 5 mA, respectively.

(a) HV test transformer

(b) Two-stage CW multiplier
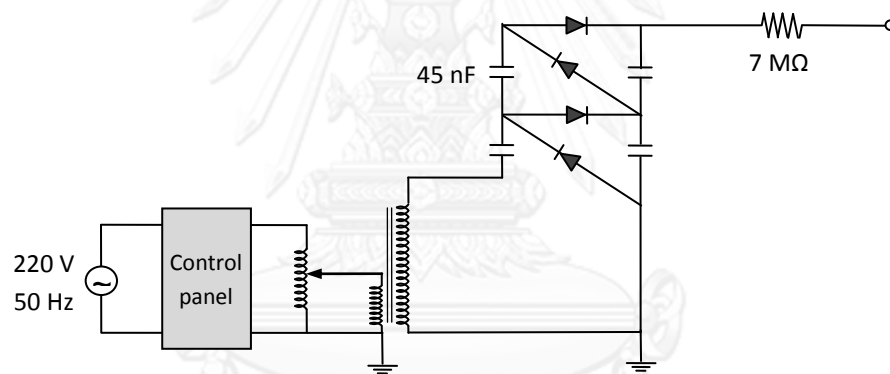
(c) Circuit diagram

Figure 6.5. DC voltage obtained by using a HV test transformer and a two-stage CW multiplier.

6.4 Electrode systems

Two electrode systems with different arrangements were utilized for observation of the particle movement and measurement of the corona discharge on the particles.

6.4.1 Electrode system used for observation of the particle movement

For the observation of the particle movement, the electrode system was composed of two parallel stainless-steel plates of 40 mm in diameter and 15 mm in thickness, as shown in Figure 6.6. The edges were rounded to prevent excessively high electric field. The high-voltage electrode was suspended from a z-axis stage (ZSG880, Misumi),

which had 26 mm travel distance. The grounded electrode was set on a *xyz*-axis stage (XYZLN60, Misumi), whose travel distances were ±9, ±10, and +26 mm in the *x*, *y*, *z* axis, respectively. The particle movement was observed with the gap distance between the electrodes of 9, 10, or 18 mm, which could be adjusted through the stages.

For the experiments using pressurized air, the electrode system was set inside a test chamber described in Section 6.5.
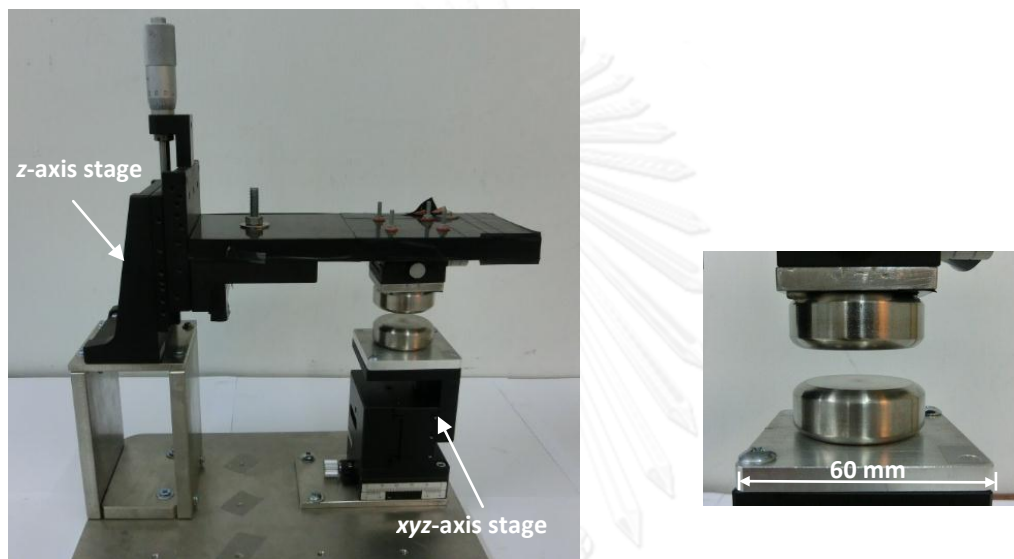
<table>
<tr><td>(a) Electrode-system setup</td><td>(b) Parallel electrodes</td></tr>
</table>

Figure 6.6. Electrode system for observation of the particle movement.

6.4.2 Electrode system used for measurement of the corona discharge

Figure 6.7 shows the electrode system used for the measurement of the corona discharge in atmospheric air. The upper electrode was a copper disc with diameter of 110 mm. It was supported by three cylindrical Polyoxymethylene (POM) spacers located on the lower electrode. The lower electrode was made from aluminum, and consisted of two concentric parts separated by a thin Polyethylene-terephthalate (PET) sheet. The inner part, called as the central electrode, was a cylinder with 10 mm in thickness and 20 mm in diameter. The outer one was a block composed of a plate and a hollow cylinder. Note that the plate had a hole at its center, and the diameter of this hole was that of the PET sheet. The hollow cylinder of the outer part resulted in a void space between the lower electrode and the grounded plane. This space was covered by a closed conducting surface. In this space, a 50 Ω resistor was connected between the inner and outer parts (see Figure 6.7b). In

addition, a conducting wire was connected between the inner part and the center core of a coaxial cable connector installed on the outer part. With this connection, the obtained signal at the cable connector was the voltage signal across the resistor. In the corona measurement, the test particle was placed on the central electrode (the inner part).

The electrode system in Figure 6.7 eliminated unwanted corona discharges at the electrode edges. The corona measurement was performed with a gap distance of 10 mm, set by the spacer height.

For the measurement of the corona inception voltage, the wire particle was kept in standing orientation on the central electrode by using a silicone rectangular-parallelepiped piece ($3 \times 2 \times 0.5$ mm^3), as shown Figure 6.8.
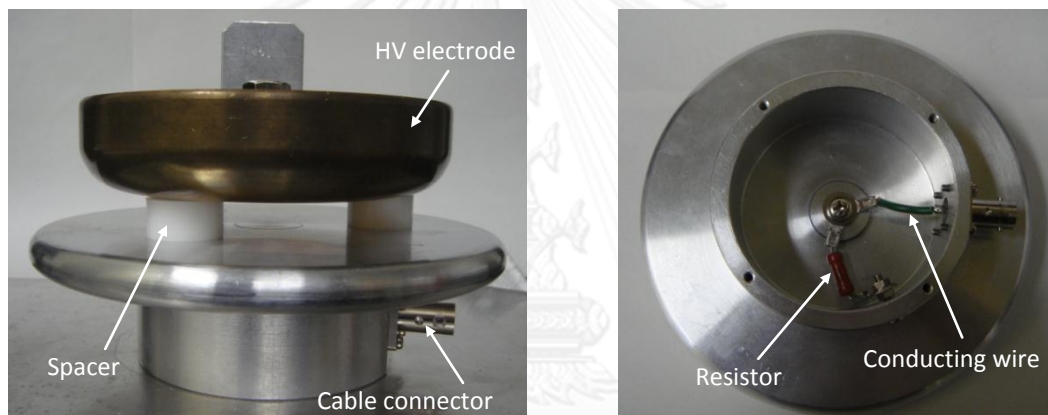
(a) Image of electrode-system setup (b) Bottom view of lower electrode
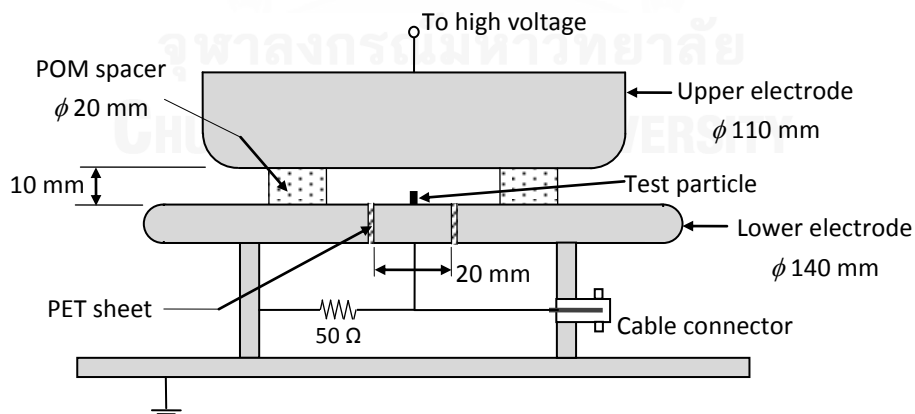
(c) Schematic diagram of electrode-system setup

Figure 6.7. Electrode system for measurement of the corona discharge on the particle.
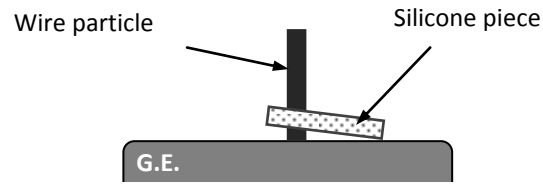
Figure 6.8. Wire particle kept vertically on the grounded electrode.

6.5 Test chamber

For the experiments under pressurized air, the electrodes were contained in a steel chamber, as shown in Figure 6.9. The chamber had an inner diameter of 250 mm and a height of 230 mm. Two glass windows of diameter 60 mm were installed at the middle of the wall for illumination and for observation. The top and bottom plates of the chamber were 10-mm thick and 340-mm diameter stainless-steel. The top cover was removable. It had a hole with diameter of 40 mm at the center, sealed by a rectangular-parallelepiped block of epoxy resin on the lower side of the cover. Rubber O-rings were used to prevent the leakage of the air. The inlet and outlet of air and the port of the pressure measurement were installed on the chamber wall (see Figure 6.9).

A stainless-steel rod plugged through the block was used as a conducting wire. The upper electrode was connected to the lower end of the conducting rod. The lower electrode was set on the *xyz*-axis stage mounted on the chamber base. The gap was set equal to 10 mm in the experiments. The experiments with the chamber were carried out with air at 0.2 MPa gauge pressure at room temperature and humidity.

6.6 Observation and measurement equipments

6.6.1 Observation equipment

The photographs or images of the test particles were taken by a charge-coupled device (CCD) camera (902H2 SUPREME, Watec) with a fixed-focus telecentric lens (GT-TC2-65, Generex) and by a stereo microscope (EMT-1, Meiji) with 10 or 20 time magnification. The Meiji microscope and another one (VMT-2F-M, Olympus) with 10 or 20 time magnification were used to examine the profile of wire particles.

To observe the behavior of the spheroidal and wire particles under electric field, a digital video camera was used to record the particle trajectory with a frame rate up to 1000 fps. The video images exported to a computer for analysis.

Most of the experiments used the digital camera (EX-ZR200, Casio) having frame rates between 30 and 1000 fps. An external LED light was used to enhance the images at the electrode system. A few tests of the movement of wire particles, performed at the University of Tokyo, used a high-speed camera (V311, Phantom) having the frame rate up to 500,000 fps. For this camera, the use of the external light was unnecessary at 1000 fps.
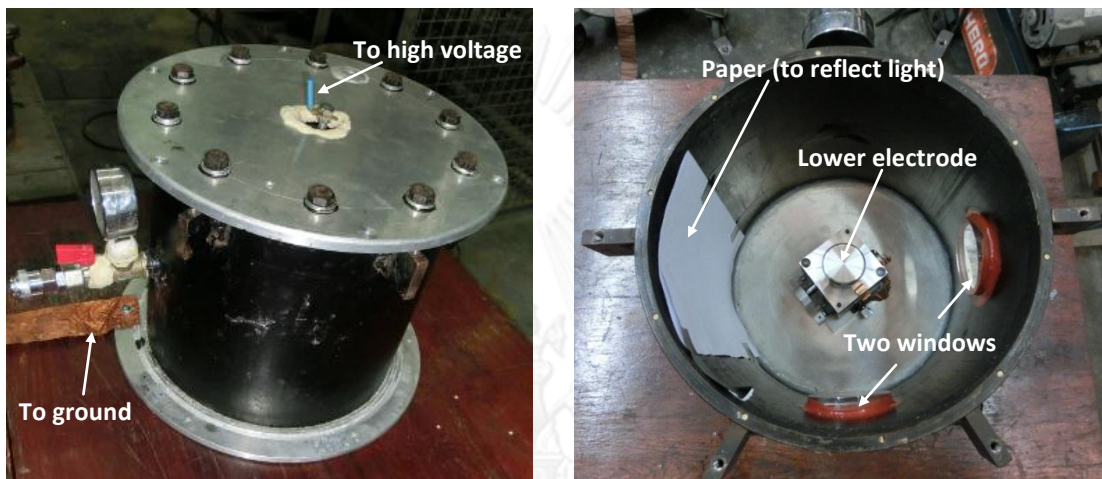
(a) Image of test chamber   (b) Top view when the cover was removed
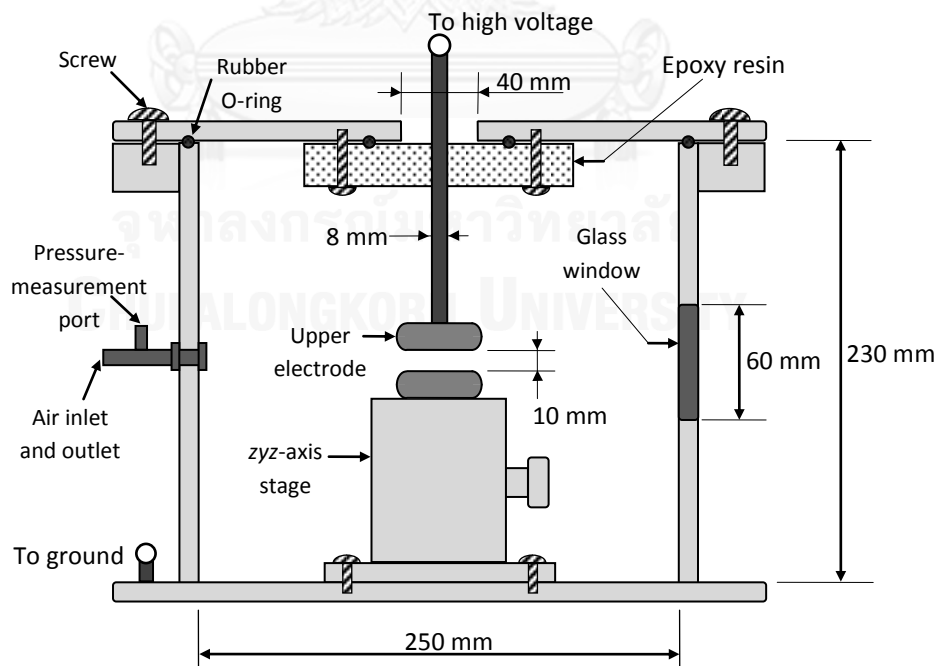
(c) Schematic diagram

Figure 6.9. Test chamber for experiments in pressurized air.

6.6.2 Measurement equipment

Measurement of corona discharge used the electrode system with a central electrode, presented in Figure 6.7. Corona current pulses on the particles were measured through a 50 Ω resistor connected in series with the grounded electrode. The voltage waveform was measured by a 4-channel, 1-GHz digital oscilloscope (DPO 4104, Tektronix). The oscilloscope was synchronized with the high-speed camera through the trigger output signal of the oscilloscope. The minimum trigger level of the oscilloscope was set to be less than 10 mV (equivalent to 200 μA) to detect the corona pulses.

6.7 Experimental procedure

In the experiments, test particles and the electrode surface were cleaned by ethanol, and by a hair dryer or waiting for about 3 minutes under room temperature. The cleaning was done before each test for observation of the particle movement and every ten tests for the measurement of the corona inception voltage.

For observation of the particle movement, a particle was placed on the lower (grounded) electrode in lying orientation. The applied voltage was then increased gradually with the rate of about 0.5 kV/s until the particle moved for observation under lifting voltage. The movement of the particle was detected by eyes through the monitor of the digital camera or that of a computer connected to the high-speed camera. Some observation was made under a specified applied voltage, i.e., 8 or 9 kV. Note that when using the chamber, the chamber was opened after each test to reset the particle position for the next test.

For measurement of the corona inception voltage, a particle was placed on the central electrode in standing orientation. The applied voltage was increased gradually with the rate of about 0.5 kV/s until the corona discharge was detected by using the trigger mode of the oscilloscope.

CHAPTER VII

EXPERIMENTAL RESULTS AND DISCUSSION

This chapter presents the experimental results of the movement behavior of prolate spheroidal and wire particles described in Chapter VI. The experiments are carried out in air with DC positive and negative voltage applied to the upper electrode. The author focuses on the lifting electric field and the lifting behavior of the particles. For the spheroidal particles, the experimental results are compared with the analytical prediction. For the wire particles, the electrostatic force and torque on the particles are analyzed by using a prolate spheroidal model for various arrangements. The charge amount on the particles is varied in the analysis to reflect the charge losses due to corona discharge.

7.1 Prolate spheroidal particles

The experiments on the spheroidal particles were done in the atmospheric air with 9 mm or 18 mm gap between electrodes under positive voltage application. The particle movement was observed by gradually increasing the applied voltage. Two sizes of the particles were used for the experiments as explained in Section 6.1.1.

7.1.1 Movement behavior

From the recorded images, it was found that the particle might move initially at either end or at both ends. The behaviors of the particles may be classified into three main patterns. For the first movement pattern, the particle moved initially at an end. Then, it rotated on the electrode, and departed from the electrode at a tilt angle, mostly between 35° to 65°. Figure 7.1 shows the diagram and images of the first pattern. After the departure, the particle continued rotating while moving to the upper electrode, as shown in the rightmost image in Figure 7.1b. The second pattern was similar to the first one, but the particle fell after departure, as shown in Figure 7.2. The last pattern is shown in Figure 7.3. The particle was lifted parallel from the electrode. Afterward, it began rotation while moving up to the upper electrode.

(a) Diagram

#1 #2 #3 #4

(b) Images (in a temporal sequence)
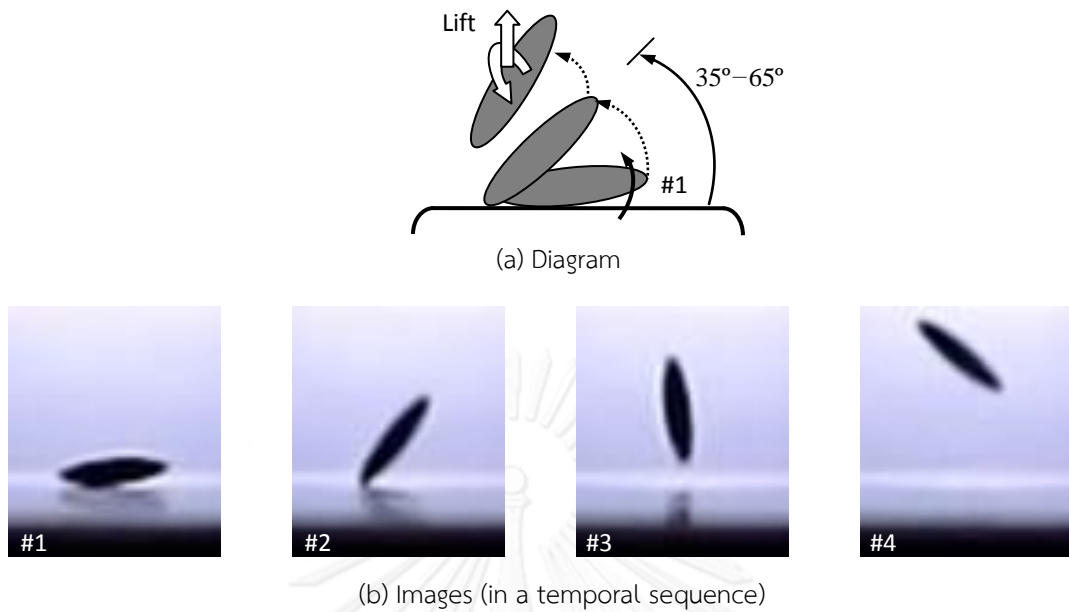
Figure 7.1. Diagram and images of the first movement pattern.

(a) Diagram

#1 #2 #3 #4

(b) Images (in a temporal sequence)
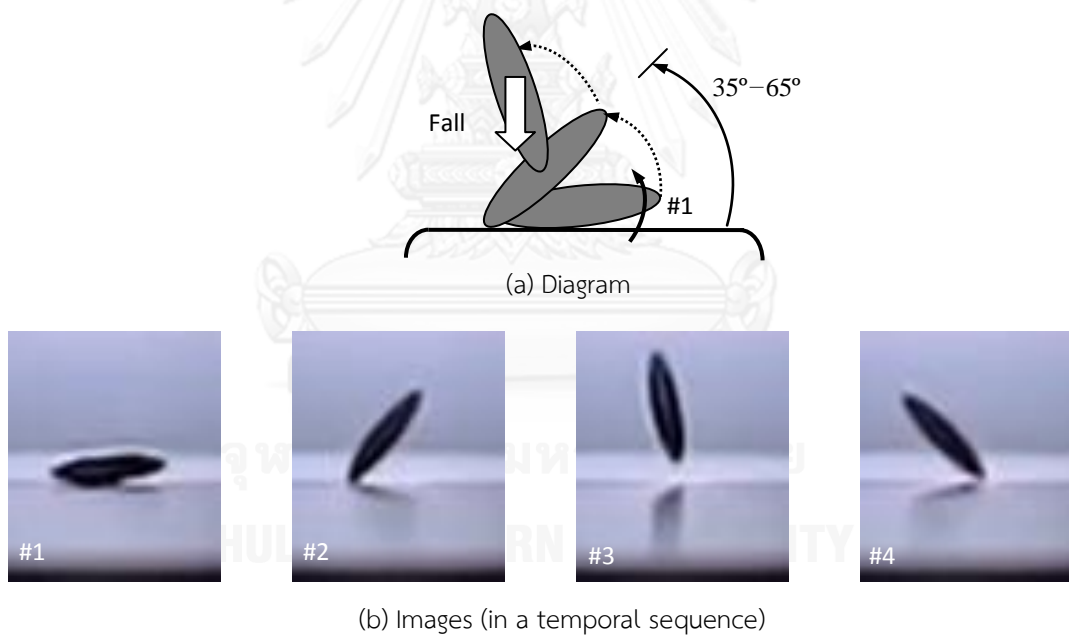
Figure 7.2. Diagram and images of the second movement pattern.

Figure 7.4 presents the incident rates of the movement patterns of the small and large particles in the 9 mm and 18 mm electrode gaps. It is clear from the figure that the particles mostly moved initially at an end (first and second patterns). In particular, the large particle did not exhibit the third pattern in the 18 mm gap. After the initial movement at an end, the particles always immediately lifted to the upper electrode, except the small particles in the 18 mm gap. In this case, the incident rate

of the falling phenomenon after departure was 17%. The probability of the initially parallel movement was greater for the electrode gap of 9 mm than for that of 18 mm for both particle sizes.

(a) Diagram

(b) Images (in a temporal sequence)
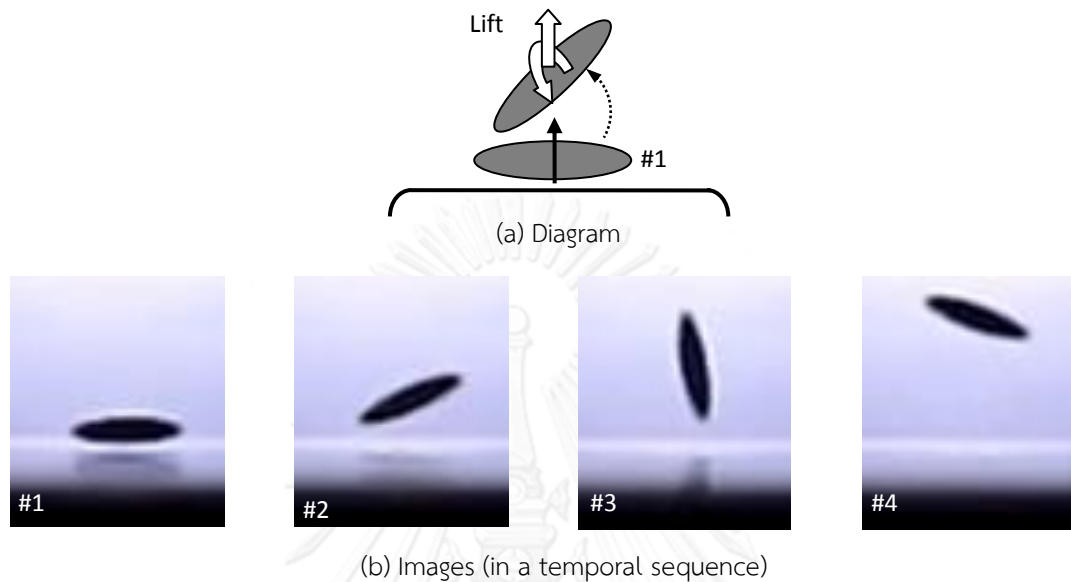
Figure 7.3. Diagram and images of the third movement pattern.
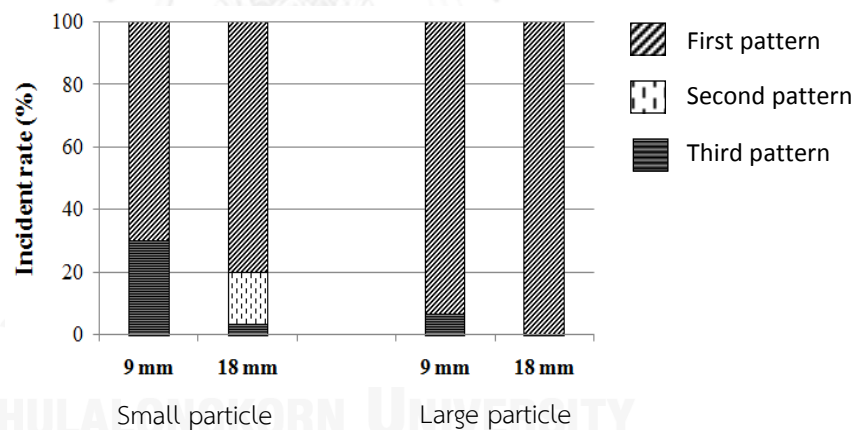
Figure 7.4. Incident rates of the movement patterns.

7.1.2 Lifting electric field

Figures 7.5a and 7.5b present the measured lifting electric field for the small and large particles, respectively. The maximum, minimum, and average values are given on the graphs. The figures indicate that the average lifting field was slightly smaller for shorter electrode gap. This might be due to the effects of the image charges induced on the upper electrode. However, the difference was rather insignificant. The

average lifting field was 8.15 kV/cm for the small particle and 9.75 kV/cm for the large particle.

(a) Small particle

(b) Large particle
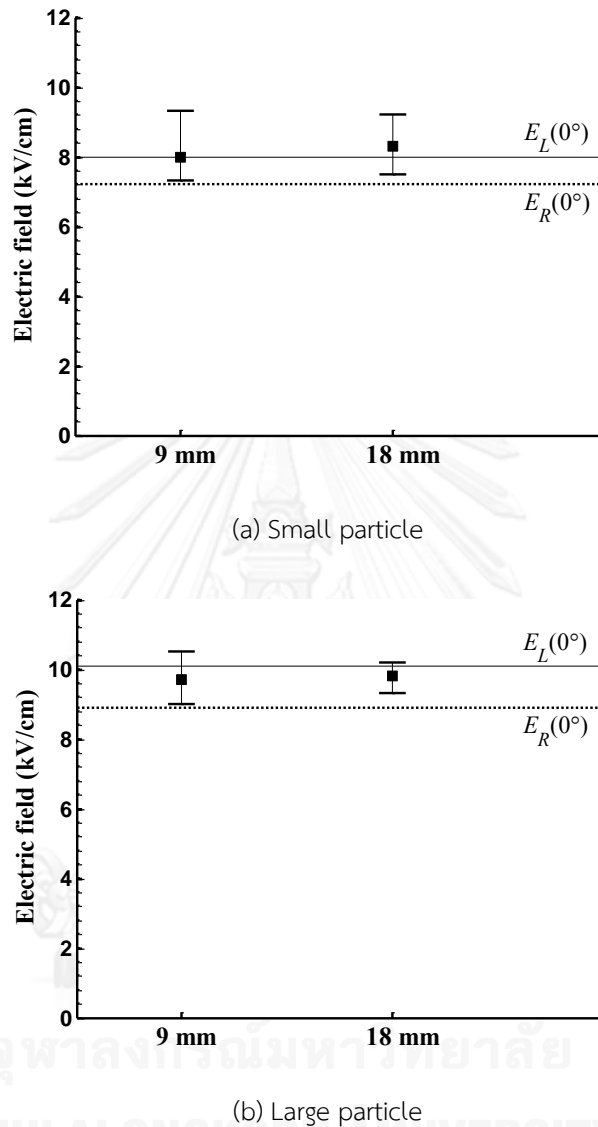
Figure 7.5. Measured lifting electric field of the particles in 9 mm and 18 mm electrode gaps.

7.1.3 Discussion

The 3D analysis of the electrostatic force and torque on a conducting spheroid has been presented in Chapter V. Figure 7.6 shows the characteristics of E_L and E_R for the small and large particles used in the experiments. Note that $E_R(\alpha = 0°)$ is the critical field that rotates the particle if there is a small disturbance on α. $E_R(0°) < E_L(0°)$ in Figure 7.6. Hence, if the angle α slightly deviates from 0, the particle rotates on the

electrode and is then lifted from the electrode at $\alpha = \alpha_1$ when $E > E_L(\alpha_1)$. From Figure 7.6, $\alpha_1 = 15°$ for the small particle and 37° for the large particle.
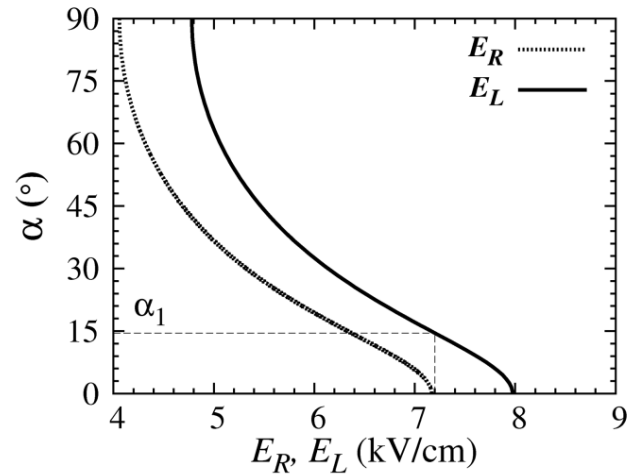
(a) Small particle
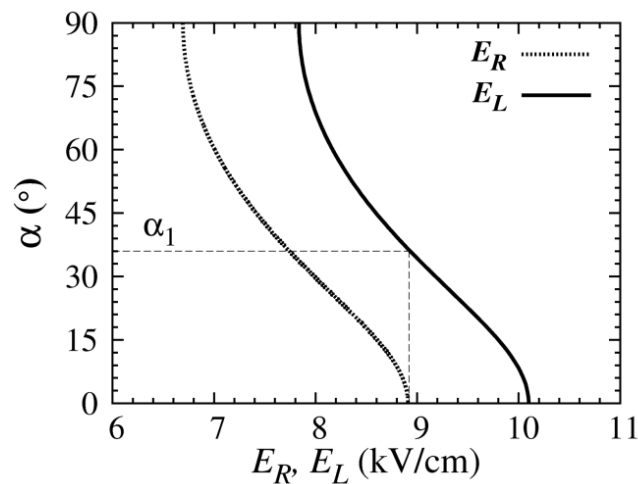
(b) Large particle

Figure 7.6. Characteristics of lifting electric field E_L and rotating electric field E_R of the particles used in the experiments.

As shown in Figure 7.4, the particles rotated on the lower electrode in most cases. Only for the small particle in the 9 mm electrode gap, the incident rate of the parallel lift (third pattern) was about 30%. Thus, the theoretical lifting-field was not $E_L(0°)$ but was $E_R(0°)$. The $E_L(0°)$ and $E_R(0°)$ values for the small and large particles are plotted as the solid and dotted lines in Figure 7.5 for comparison. From the figure, we can see that the average values of the measured lifting field were larger than $E_R(0°)$. The difference between the average lifting field and $E_R(0°)$ was between 10%

and 15%. In the experiments, when a particle moved initially at both ends, it was lifted at field strength greater than $E_L(0°)$ by about 8%. Therefore, the lifting field obtained from the experiment agreed quite well with calculation values. The discrepancy might result from the surface force between the particle and the lower electrode.

The departing angle obtained from the experiment was between 35–65° for both particles, which was greater than theoretical ones. This difference may be explained based on the displacement of the particle center in the vertical direction as follows. At $\alpha > \alpha_1$, the Coulomb force exceeds the gravitational force, lifting the particle center in the vertical direction. At the same time, the total torque at $\alpha > \alpha_1$ also rotates the particle in the increasing-α direction. The rotation raises the height of the particle center. If the vertical displacement of the particle center is greater due to the rotation than due to the translation, the particle does not separate from the lower electrode.

After departure from the electrode, corona discharge might take place at the upper pole of the particles due to field enhancement. At that time, the induced charge on the particles reduced, as mentioned in Chapter II. This resulted in the reduction of the Coulomb force on the particles. When the Coulomb force became smaller than the gravitational force, the particle fell on the lower electrode. However, the second movement pattern was observed only in the cases of the small particles in 18 mm gap, where the field is supposed to be larger than that in the cases of large particles. Further study is needed to clarify this behavior.

7.2 Wire particles

The experiments on the wire particles were done with the electrode gap of 10 mm under both negative and positive polarities of the applied voltage. Types of the wire particles were shown in Table 6.2. The particle end was in rounded, sharp, or very sharp profile. Dielectric coating was applied to an end of some samples (see Figure 6.2). The experiments were carried out in the atmospheric air, except for Section 7.2.5 that the pressurized air was used.

7.2.1 Lifting electric field

The lifting electric field was measured for two types of 4 mm uncoated particles, i.e., particles with rounded ends (R-R), and particles with a rounded end and a sharp end (R-S). The R-S particles were placed on the grounded electrode in two different manners (orientations). For the first orientation, the tip of the sharp end was on or

very close to the electrode. For the second orientation, the tip was at the highest position, separated from the electrode. The electric field at the tip was stronger in the latter orientation.

The average value of the measured lifting field was 7.3 kV/cm for the R-R particles. For the R-S particles, the lifting field was 7.4 kV/cm when the tip was on the electrode and 7.0 kV/cm when the tip was separated from the electrode. The theoretical value of the lifting electric field is 7.2 kV/cm for an infinitely long conducting cylinder on a planar electrode. Hence, the measured values deviate slightly from the theoretical prediction.

7.2.2 Initial movement

The initial movement was defined as the first motion on the grounded electrode under the voltage application. The initial movement was at either end first or at both ends simultaneously. For example, the R-S particles may exhibit an initial movement at the rounded end, at both ends (parallel lift), or at the sharp end. The initial movement was discussed here for the 4 mm uncoated particles. For the particles having a sharp end, orientations with tip on the electrode and with tip separated from the electrode were used to investigate their influence on the behavior. The initial movement was observed under application of a gradually increasing voltage or a fixed voltage magnitude 8 kV or 9 kV for both positive and negative polarities.

a) Under gradually increased voltage

Figure 7.7 presents the initial movement of the R-S particles when the voltage was gradually increased. The results are grouped by the initial orientations and the voltage polarities. Figure 7.7a indicates that when the tip was on the electrode surface, the particle often moved initially either at the rounded end or at the sharp end. On the other hand, when the tip was highest from the electrode surface in Figure 7.7b, the sharp end was almost raised first. The behavior in Figure 7.7b agreed well with the results obtained in [22]. The initial movement at both ends was seldom observed. Figure 7.7 does not show a dependency of the initial movement on the applied voltage polarity.

For the R-R particles, probability of the initial movement at both ends was 30% and 26.7% under negative and positive voltage application, respectively. The results imply the consistency of the rounded profiles of the particles.

<table>
<tr><td></td><td>(a) On electrode surface</td><td>(b) Highest from electrode surface</td></tr>
</table>

(a) On electrode surface   (b) Highest from electrode surface
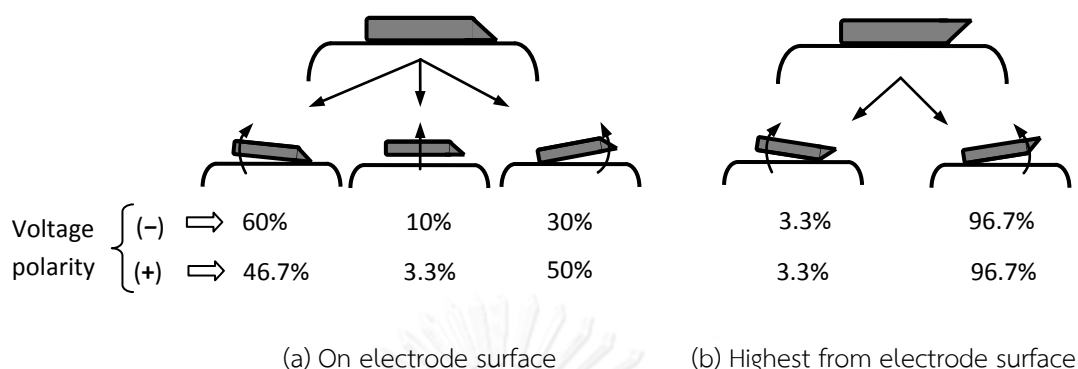
Figure 7.7. Probability of initial movement of the 4 mm R-S particles when the
applied voltage was gradually increased.

b) Under 8 kV or 9 kV applied voltage

Figure 7.8 presents the result of the initial movement for the R-S and R-SS
particles under 8 kV application separately for each combination of the initial tip
orientation and voltage polarity. The initial movements are presented using the
patterns as shown in the inset. From Figure 7.8, the initial movement of the R-S and
R-SS particles has the same behavior for the same orientation and voltage polarity.
When the tip was on the electrode in Figure 7.8a, the probabilities of the movement
patterns were close to each other under the negative voltage polarity, and the
probability of the initial movement at both ends was smaller under the positive
voltage application. When the tip was separated from the electrode in Figure 7.8b,
the sharp end was mostly raised first, irrespective of the voltage polarity.

The initial movement of the R-S and R-SS particles when the tip was
separated from the electrode was further investigated under stronger field by using 9
kV voltage application. The results are shown in Figure 7.9. The figure indicates that
the R-S and R-SS particles had the similar behavior of the initial movement under
both voltage polarities. The initial movement at the sharp end was still dominant.
However, the movement at both ends had clearly higher probability in comparison
with Figures 7.8c and 7.8d.

(a) Tip on the electrode under negative voltage

(b) Tip on the electrode under positive voltage

(c) Tip separated from the electrode under negative voltage

(d) Tip separated from the electrode under positive voltage
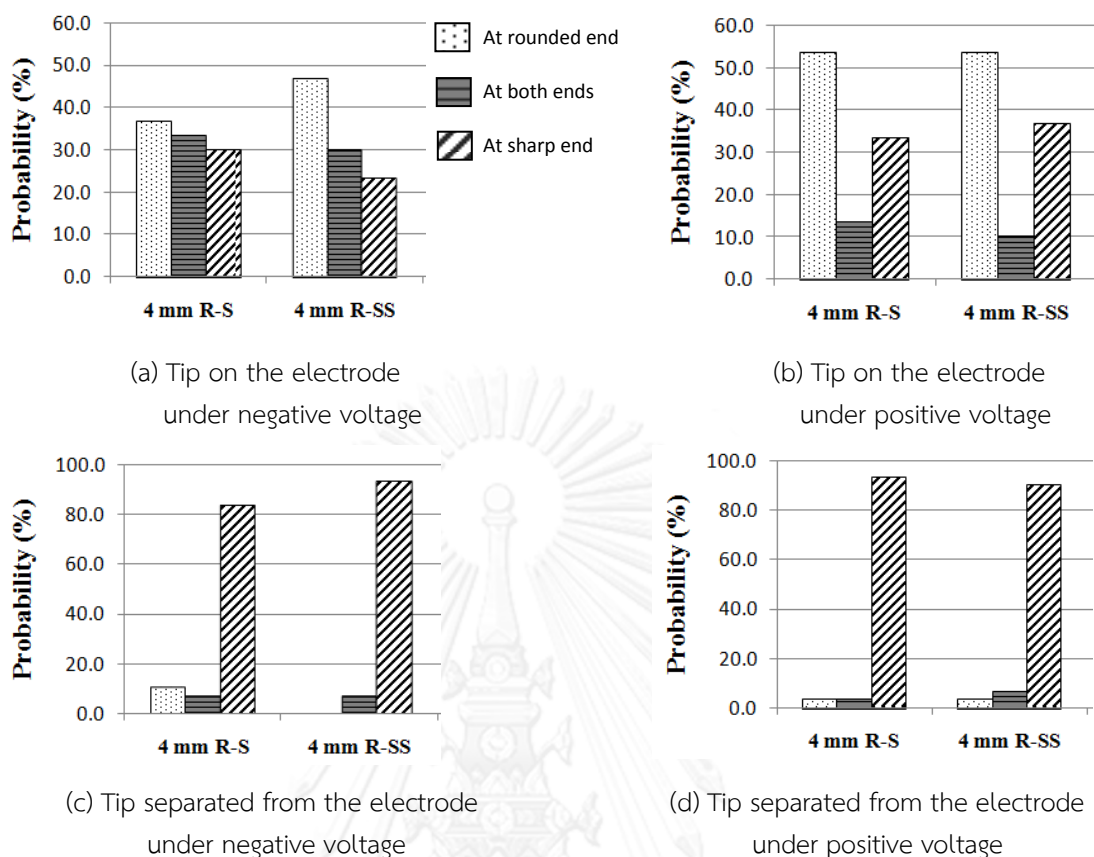
Figure 7.8. Probability of initial movement of the 4 mm R-S and R-SS particles under 8 kV voltage application.

(a) Negative voltage

(b) Positive voltage
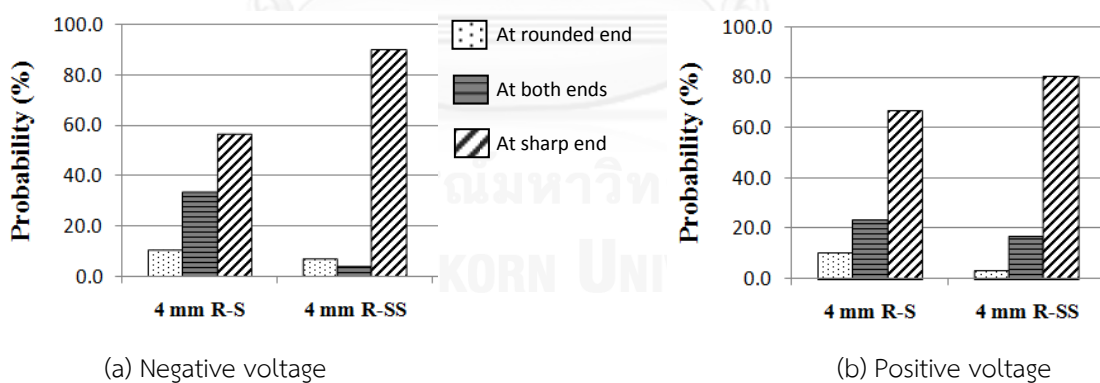
Figure 7.9. Probability of initial movement of the 4 mm R-S and R-SS particles under 9 kV voltage application when the tip was separated from the electrode.

The initial movement of the R-R and S-S particles did not depend much on the voltage polarity. The results of the initial movement are presented in Figure 7.10. The probability of the initial movement at both ends was 28% for the R-R particles and 23% for the S-S ones under 8 kV voltage application. The probability was larger

when the voltage was increased to 9 kV, especially for the R-R particles. From the results in this section and in Section 7.2.1, where the applied voltage was usually smaller than 8 kV, the particles tended to have a higher probability of the initial movement at both ends with stronger applied electric field.

(a) Under 8 kV   (b) Under 9 kV
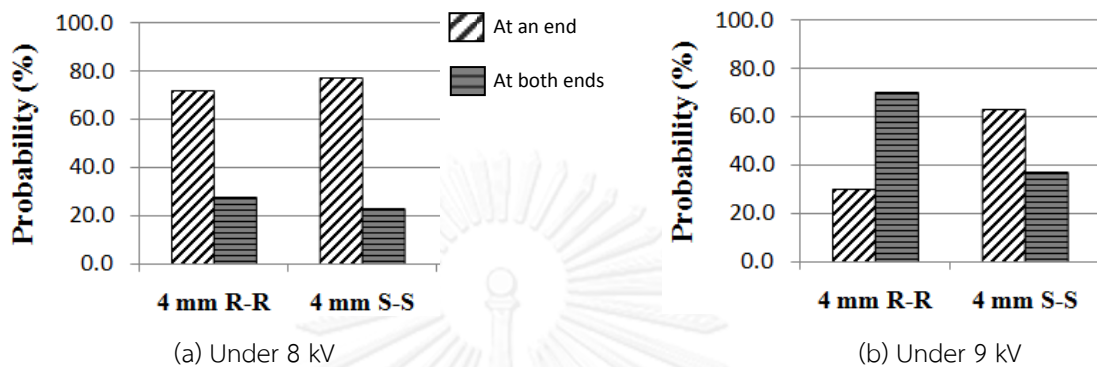
Figure 7.10. Probability of initial movement of the 4 mm R-R and S-S particles.

7.2.3 Subsequent movement of uncoated particles

The behavior of the particles after their initial movement is referred as "subsequent movement". The observation of the subsequent movement was done mainly for the applied voltage of 8 kV and 9 kV to investigate the effect of the corona discharge. For the particles having a sharp end, the tip of the sharp end was placed separated from the grounded electrode to obtain high field intensification under 9 kV voltage application. Under 8 kV, both initial orientations of the tip were used.

The previous section explains a variety of the initial movements, which directly contributes to the subsequent movement. In addition, the initial movements affected the variation of the particle charges and the degree of corona discharge, which also had an effect on the subsequent movement. Therefore, this section discusses the subsequent movement separately for each kind of the initial movement.

The number of occurrences of the initial movements of uncoated particles under both voltage polarities is presented in Tables 7.1 and 7.2 for 8 kV and 9 kV voltage applications, respectively.

Table 7.1. Number of occurrences of initial movements for uncoated particles under 8 kV.

Voltage polarity	(−)			(+)		
Initial movement / Particle type	At rounded end	At both ends	At sharp end	At rounded end	At both ends	At sharp end
2 mm R-S	14	11	35	10	20	30
4 mm R-S	14	12	34	17	5	38
4 mm R-SS	14	11	35	17	5	38
4 mm S-S	✕	13	47	✕	15	45
4 mm R-R	44	16	✕	42	18	✕

Table 7.2. Number of occurrences of initial movements for uncoated particles under 9 kV.

Voltage polarity	(−)			(+)		
Initial movement / Particle type	At rounded end	At both ends	At sharp end	At rounded end	At both ends	At sharp end
2 mm R-S	0	9	21	0	6	24
4 mm R-S	3	10	17	3	7	20
4 mm R-SS	2	1	27	1	5	24
4 mm S-S	✕	9	21	✕	13	17
4 mm R-R	10	20	✕	8	22	✕

a) Under negative voltage

After initial movement at the sharp end

After initial movement at the sharp end, uncoated particles rotated about the lower end. During the rotation, they might also slide on the electrode. The particles departed from the lower electrode at a tilt angle between 20° to 55°, as illustrated in Figure 7.11a. They also continue rotation while moving to the upper electrode. We refer to this behavior as "immediate lift". In other cases, electrical discharge occurred between the upper or lower particle tips and the electrodes after departure, as shown in Figure 7.11b. These cases are referred as "lift and breakdown".

Figure 7.12 shows the incident rates of the immediate lift and the particle-induced breakdown for each particle type. We can see from the figure that the 2 mm particles always immediately lifted to the upper electrode, whereas the 4 mm

particles exhibited both kinds of the behaviors. For each applied voltage magnitude, the incident rate of the lift and breakdown behavior of the 4 mm particles increased in the following order: R-S, R-SS, and S-S particles.
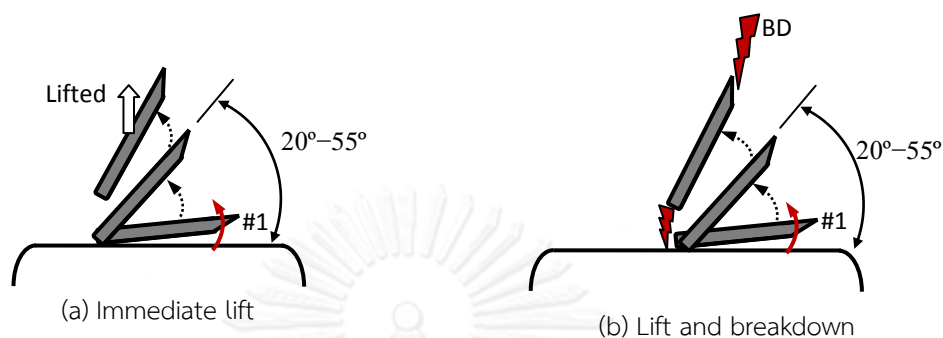
Figure 7.11. Typical behaviors of uncoated particles after initial movement at the sharp end under negative voltage.
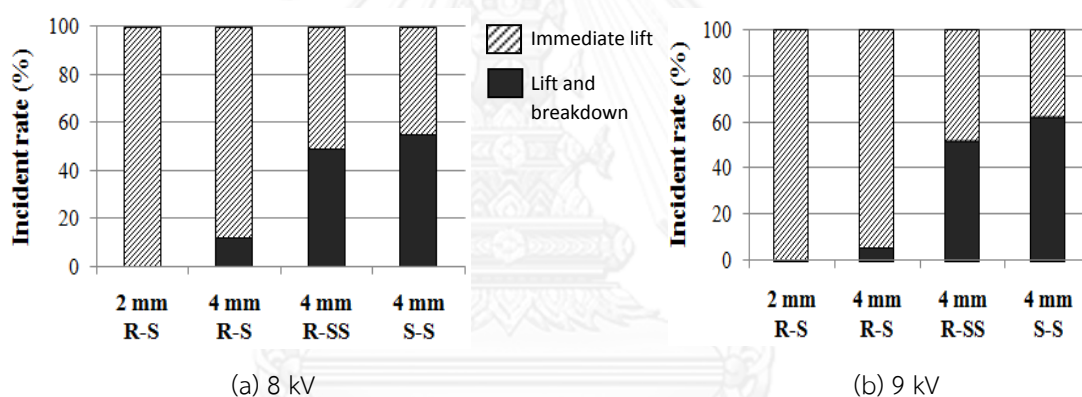
Figure 7.12. Incident rates of the subsequent movement under negative voltage after initial movement at the sharp end.

After initial movement at both ends

After initial movement at both ends, particles might rotate one of its ends up. When the rounded end was rotated up, all particles exhibited immediate lift. When the sharp end of the S-S particles was rotated up, the breakdown took place with the incident rate about 38% under 8 kV and 33% under 9 kV applied voltage. These incident rates were considerably lower than those of the corresponding cases in Figures 7.12a and 7.12b. For other kinds of particles except the S-S ones, however, breakdown did not take place even when their sharp end was rotated up.

After initial movement at the rounded end

When the particles initially moved at the rounded end, they were lifted immediately to the upper electrode without breakdown.

b) Under positive voltage

After initial movement at the sharp end

Under positive voltage, the behavior after the initial movement differed from that under negative voltage. After departing from the electrode, some particles fell on the lower electrode. Subsequently, the particles either (i) bounced on the electrode and lifted again to the upper electrode or (ii) rotated on the lower electrode. These kinds of behavior are referred as "lift after falling" and "rotation after falling", respectively. Their approximate trajectories are illustrated in Figures 7.13a and 7.13b, where the dotted arrows indicate the sequence of movements. For the immediate lift, the tilt angle at which the particles departed from the lower electrode was between 30° and 55°.

(a) Lift after falling   (b) Rotation after falling

Figure 7.13. Movements of uncoated particles that fell on the lower electrode after departure.

(a) 8 kV   (b) 9 kV

Figure 7.14. Incident rates of the subsequent movement of uncoated particles after initial movement at the sharp end under positive voltage.

Figure 7.14 presents the incident rates of the classified behaviors under 8 kV and 9 kV positive voltages. The figure shows similar tendencies of the incident rates for 8 kV and 9 kV. The immediate lift was always observed for the 2 mm particles,

but seldom seen for the 4 mm particles. For the 4 mm particles, the rate of rotation after falling increased in the order of R-S, R-SS, and S-S particles. In particular, the rotation after falling was predominant for the 4 mm S-S particles. For the lift after falling, the incident rate varied reversely to this order.

After initial movement at both ends

Similarly to the cases of negative voltage application, the particle behavior is considered separately based on which end is rotated up after the initial movement. When the rounded end was rotated up, the immediate lift was usually observed. The incident rates of lift after falling were only 8.7% under 8 kV and 0% under 9 kV applied voltages, whereas the rotation after falling was not observed.

Figure 7.15 presents the incident rates when the sharp end is rotated up after the initial movement. The results are similar to those in Figure 7.14 (after initial movement at the sharp end) as the 2 mm particles were always immediately lifted, and the 4 mm particles exhibited both immediate-lift behavior and lift-and-falling behavior. Except the case of the 4 mm R-S particles (second column in Figure 7.15a), the incident rates of the rotation after falling and the lift after falling increased in the same order of particles types as those in Figure 7.14. In comparison of Figures 7.14 and 7.15, the incident rate of rotating after falling was lower in Figure 7.15 for the same particle ending profiles.

(a) 8 kV   (b) 9 kV
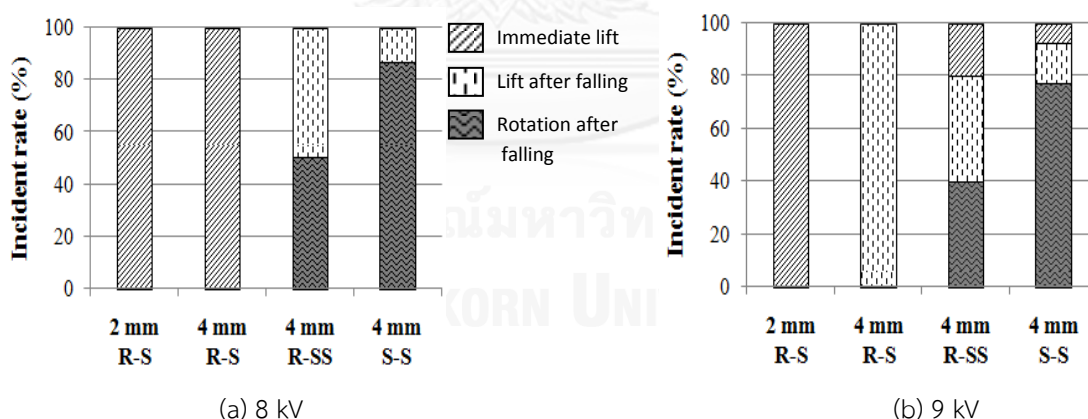
Figure 7.15. Incident rates for the uncoated particles under positive voltage when the sharp end is raised after initial movement at both ends.

After initial movement at the rounded end

After the initial movement at the rounded end, the 2 mm particles (with a rounded end and a sharp end) were always lifted to the upper electrode. The 4 mm particles (including the particles with both rounded ends) mostly exhibited the

immediate lift. There were only 1.3% and 33.3% incident rates under 8 kV and 9 kV applied voltages for the lift after falling. No rotation after falling was observed. The tendency of particle behavior in this case was similar to that when the rounded end was rotated up after initial movement at both ends.

7.2.4 Subsequent movement of coated particles

The coated particles were initially placed such that the tip of the uncoated end in sharp profile had both orientations on the grounded electrode. However, for a coated particle, the tip might not be located perfectly at the highest or lowest position due to non-symmetrical shape of the dielectric coating. The number of occurrences of the initial movement for 8 kV and 9 kV voltage applications is presented in Tables 7.3 and 7.4, respectively.

Table 7.3. Number of occurrences of initial movements for coated particles under 8 kV.

Voltage polarity	(−)			(+)		
Initial movement Particle type	At coated end	At both ends	At uncoated end	At coated end	At both ends	At uncoated end
2 mm C-R	16	23	21	22	20	18
2 mm C-S	9	27	24	11	21	28
4 mm C-R	22	13	25	24	7	29
4 mm C-S	12	8	40	11	9	40
4 mm CC-S	4	12	44	5	7	48

Table 7.4. Number of occurrences of initial movements for coated particles under 9 kV.

Voltage polarity	(−)			(+)		
Initial movement Particle type	At coated end	At both ends	At uncoated end	At coated end	At both ends	At uncoated end
2 mm C-R	-	-	-	-	-	-
2 mm C-S	0	10	20	1	21	8
4 mm C-R	6	9	15	11	11	8
4 mm C-S	3	10	17	5	9	16
4 mm CC-S	4	8	18	5	13	12

a) Under negative voltage

After initial movement at the uncoated end

Under negative voltage, after initial movement at the uncoated end, coated particles exhibited the following behaviors:

- Immediate lift: the particle rotated about the coated end to obtain a larger tilt angle and then departed from the electrode.

- Rotation: the particle rotated on the lower electrode.

- Bounce: the particle rotated about 180°, made a bounce on the electrode, and then lifted.

- Breakdown: a breakdown occurred during the particle rotation.

The behaviors are illustrated in Figure 7.16.

Figure 7.17 presents the incident rates of the classified behaviors under 8 kV and 9 kV voltages. As shown in Figure 7.17a for 8 kV, the 2 mm particles mostly exhibited the immediate lift, whereas the 4 mm particles mainly rotated on the electrode, except the CC-S particles (with thick coating). The bounce behavior was observed sometimes for the 4 mm C-S particles and seldom for the 2 mm C-S particles. The behavior under 9 kV was similar to that under 8 kV. However, the incident rate of the breakdown was remarkable for the 4 mm C-S particles under 9 kV voltage.

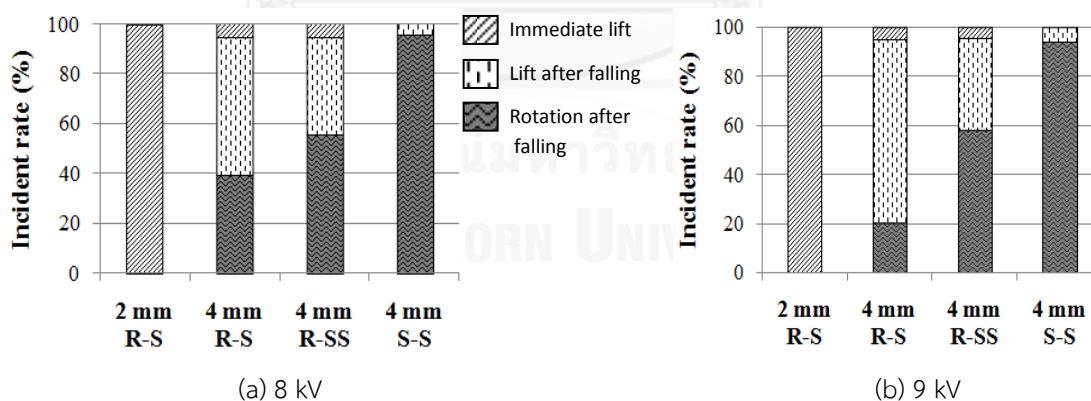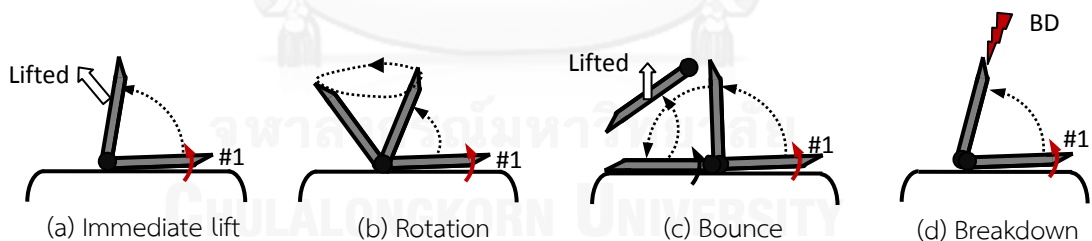Figure 7.16. Typical behaviors of coated particles after initial movement at uncoated end.
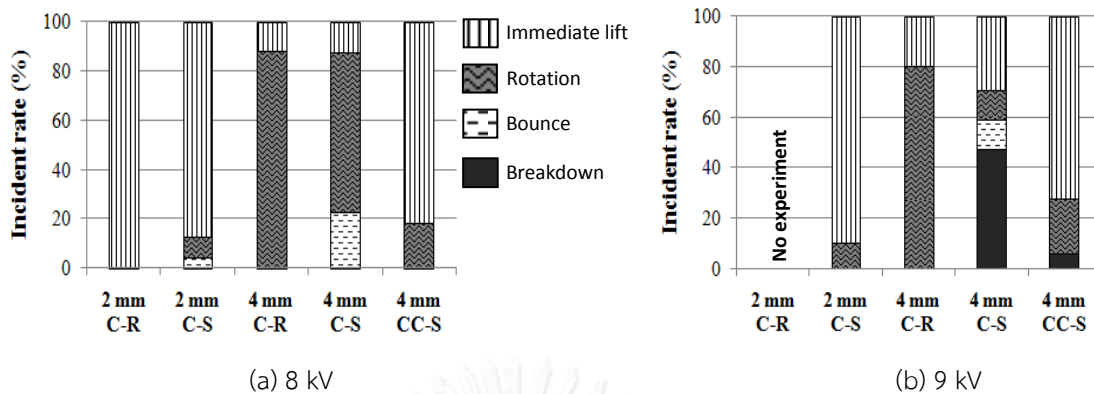
Figure 7.17. Incident rates of the subsequent movement of coated particles after initial movement at the uncoated end under negative voltage.

After initial movement at both ends

When the coated end was rotated up after the initial movement, all particles exhibited the immediate lift. When the uncoated end was rotated up, the lift after falling behavior was sometimes observed for the 4 mm C-S particles under 9 kV; however, the incident rate was only 9%.

After initial movement at the coated end

After initial movement at the coated end, all particles were lifted immediately to the upper electrode. The tilt angle before departure was about from 20° to 55°.

b) Under positive voltage

After initial movement at the uncoated end

Breakdown was not observed under positive voltage application after initial movement at the uncoated end. The incident rates of the other behaviors are presented in Figure 7.18. For the 8 kV voltage application in Figure 7.18a, the 2 mm particles tended to exhibit the immediate lift, especially for the C-S particles. For the 4 mm particles, the C-R particles mostly rotated on the electrode, whereas the C-S and CC-S particles usually exhibited the bounce behavior. With increasing the applied voltage to 9 kV, Figure 7.18b shows that the incident rate of the bounce behavior became higher and that of the rotation became lower for the 4 mm particles.

(a) 8 kV   (b) 9 kV
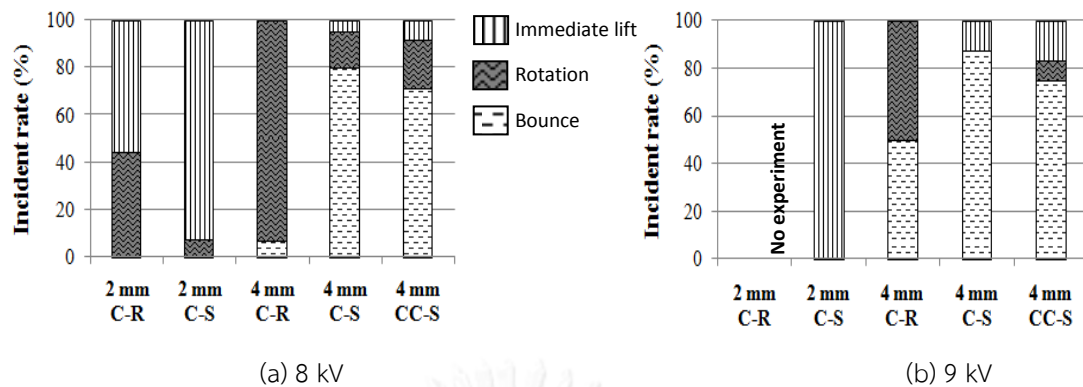
Figure 7.18. Incident rates of the subsequent movement of coated particles after initial movement at the uncoated end under positive voltage.

In comparison between Figure 7.17 and 7.18, the similar behavior was obtained for the 2 mm C-S particles (second column) with both magnitudes of the applied voltage. There was a clear difference in the behavior of the 4 mm particles, except the C-R particles (third column) under 8 kV.

After initial movement at both ends

When the coated end was rotated up after the initial movement, all particles exhibited the immediate lift, similarly to the case of negative voltage application. When the uncoated end was rotated up, apart from the immediate lift, the lift after falling behavior was observed for the 4 mm C-S and CC-S particles with the incident rate about 55% under 8 kV and 85% under 9 kV.

After initial movement at the coated end

When the particles moved initially at the coated end, the immediate lift was always observed for all particles.

7.2.5 Subsequent movement in pressurized air

Experiments were carried out in pressurized air where dielectric strength is stronger. The experiments were done at 0.2 MPa gauge pressure with the applied voltage increased gradually. The 4 mm S-S and C-S particles were used. The gap distance was 10 mm.

From the experiments, the S-S particles always moved immediately to the upper electrode after departure from the lower electrode. This behavior was independent of the initial movement and the voltage polarity.

The C-S particles exhibited similar behaviors to those in the atmospheric air. For a clear comparison, the incident rates of the subsequent movement behaviors in the pressurized air are shown in Figure 7.19 together with the results in the atmospheric condition. The figure indicates that the rotation behavior was more frequently found over other ones with increasing the pressure. Note that if the pressure of air is high enough to prevent the corona discharge, the particles are supposed to exhibit the same behavior under negative and positive voltages.

(a) Under negative voltage   (b) Under positive voltage
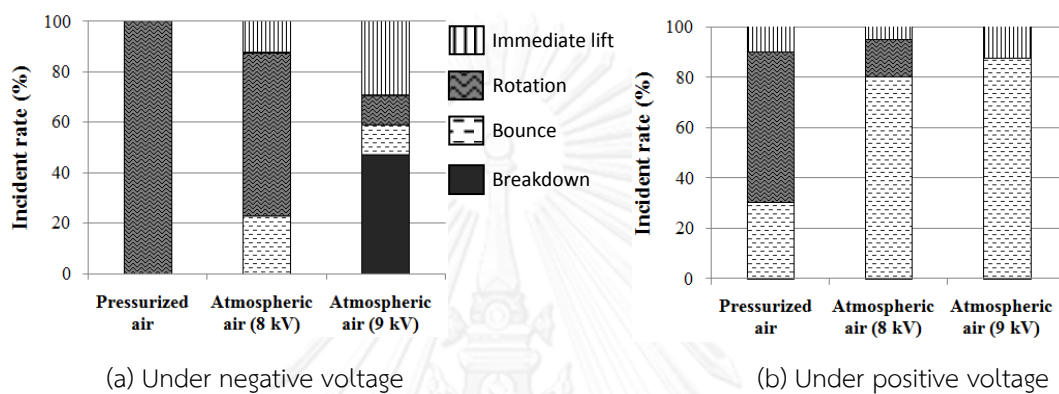
Figure 7.19. Incident rates of the subsequent movement of the 4 mm C-S particles.

7.2.6 Discussion

The induced charge on a particle after departure from the grounded electrode may be reduced by the corona discharge at its ends. This affects the force and torque on the particle. To clarify the movement behavior of the uncoated and coated particles in the experiment, a configuration based on the spheroid model was used to approximate force and torque on the particle under 8 kV voltage application. The author focused on the tendency of the force and torque with variation of the induced charge as well as the position of particle above the electrode.

Table 7.5 compares the weight, induced charge, and electrostatic force for lying and standing orientations of the wire particles and approximate spheroids. It can be seen from Table 7.5 that the wire particles were considerably heavier than the spheroidal ones. However, the charge and force of the spheroids are not significantly different from those of the wire particles.

Table 7.5. Comparison between the wire particles and approximate spheroids under the external field of 8 kV/cm.

Particles			Wire		Spheroid	
Length			2 mm	4 mm	2 mm	4 mm
Weight (μN)		P	10.4	20.8	6.9	13.9
Induced charge (pC)	Lying	Q_{ly}	22.3	44.5	22.5	40.9
	Standing	Q_{stand}	50.2	144.4	53.5	154.0
Electrostatic force (μN)	Lying	F_{ly}	12.7	25.5	14.0	24.6
	Standing	F_{stand}	35.8	106.5	38.8	114.3

Unlike uncoated particles, the coated particles can suppress the corona discharge at the coated end. When the coated end is in contact with the electrodes, the coating layer prevents the direct charging of the particles from the electrode. Note that, the layer forms an attractive force between the particle and the electrode. The force (including coating weight) for the normally thick layer was about 7.3 μN.

a) Uncoated particles

Uncoated particles acquire charge amount Q from the grounded electrode before departure from the electrode. Note that Q increases with tilt angle α as presented in Figure 5.3. After departure, the particle charge might be reduced by the corona discharge at the particle ends. Four typical values of the particle charge (Q, $Q/2$, $Q/4$ and 0) are used to observe the force variation. The first value represents the case of absence of corona discharge, which is defined as "the fully charged condition" in Chapter V.

Figures 7.20 presents the total force F_{tot} with variation of tilt angle α at δ = 0.2 mm and 2 mm for the 2 mm and 4 mm particles. Note that Q in the figure is different for different α values. The figure shows similar behaviors of the force with respect to α for the particles and the separations. The force in Figure 7.20 is reduced when the charge decreases. The figure indicates that the force is positive (in upward direction) at α > 45° when the particle charge is greater than $Q/4$. This can be applied to the explanation of that the 2 mm and 4 mm particles can approach the upper electrode after the initial movement at both ends. For example, a 4 mm particle moved initially at both ends. After departure, in the absence of the corona discharge, the particle charge was kept equal to 44.5 pC. This value is about 0.3

times of Q_{stand} (= 144.4 pC). Thus, even at the tilt angle 90°, the force on the particle was still in upward direction.

From the analysis in Chapter V, the electrostatic torque $T_{e,o}$ (also total torque) about the center **o** is positive for α between 0° and 90°. This means that the torque rotates the particle in increasing-α direction. The torque varies roughly as a parabolic function of α, and is maximal at α about 45°. Figures 7.21 shows maximum of $T_{e,o}$ with variation of δ from 0.01 to 2 mm for the 2 mm and 4 mm particles. The maximal torque increases with the reduction of the induced charge and the separation. For δ > 0.5 mm, the torque is nearly independent of induced charge and the separation.

(a) 2 mm particle at δ = 0.2 mm

(b) 2 mm particle at δ = 2 mm

(c) 4 mm particle at δ = 0.2 mm

(d) 4 mm particle at δ = 2 mm
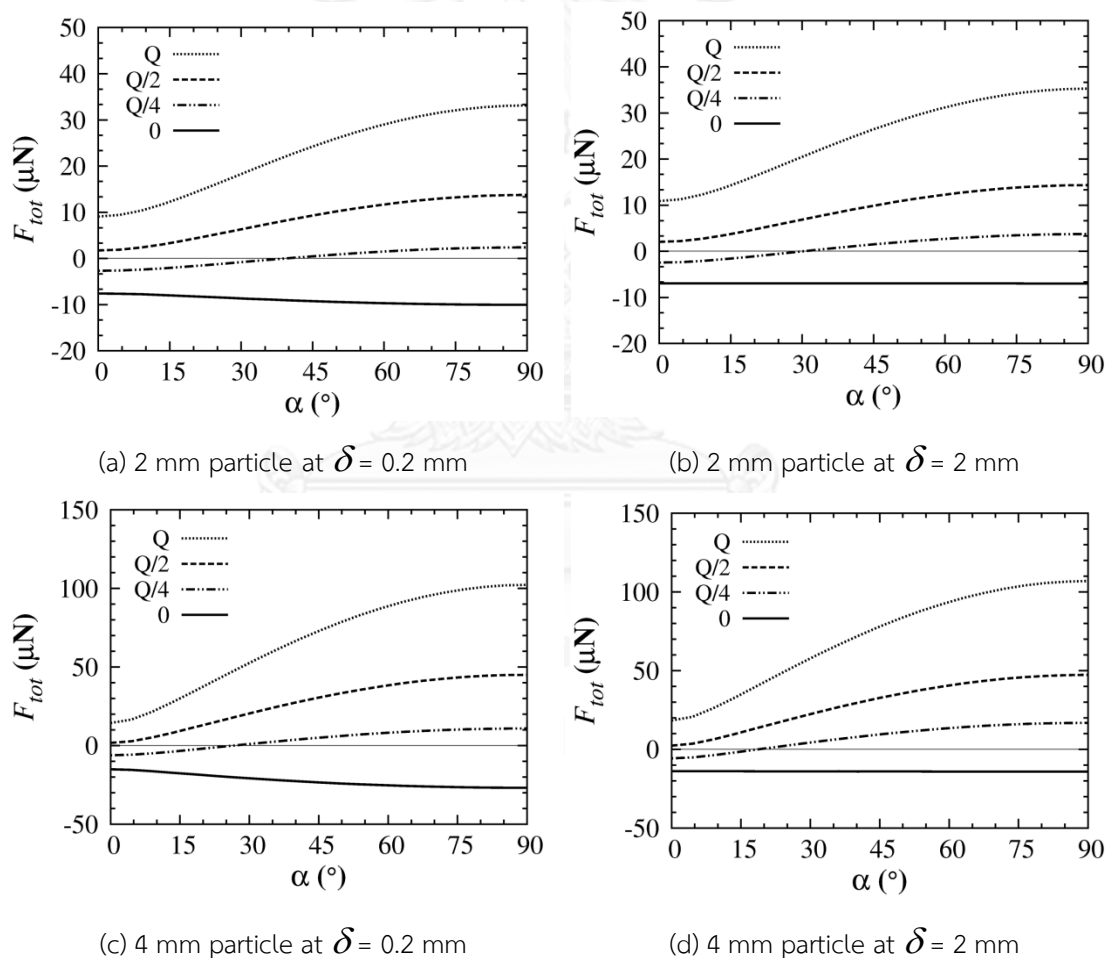
Figure 7.20. Total force on 2 mm and 4 mm particles for two δ values.

(a) 2 mm particle   (b) 4 mm particle
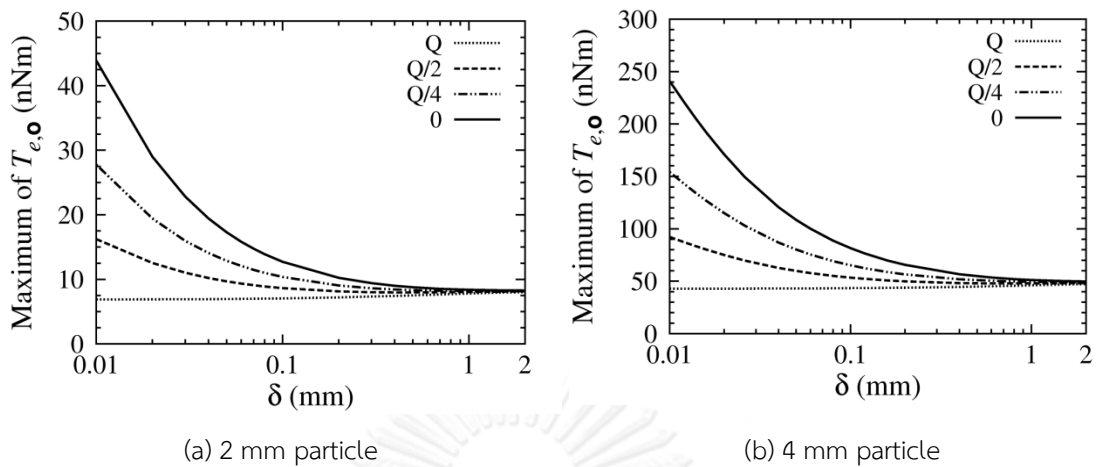
Figure 7.21. Maximum of electrostatic torque about the particle center **o**.

Under negative voltage, when a particle is near the grounded electrode, the complete breakdown occurred without preceding the corona discharge. If there is no breakdown or corona discharge, under negative voltage application the induced charge on the particles is not reduced after departure. Thus, the particles always move immediately to the upper electrode without falling even for the initial movement at both ends which has lowest initial charge amount compared with the initial movement at an end. This agreed well with the experimental results of the 2 mm and 4 mm particles.

Under positive voltage, the corona inception voltage is minimal when the wire particle is in contact with a grounded electrode [14]. According to the measurement of the corona inception voltage U_i of the 2 mm and 4 mm particles in standing position (in Appendix C), the corona inception voltage decreased with the particle length and the degree of the sharpness at the particle ends. This means that with the same applied voltage, the corona degree is greater for longer and sharper particles.

For the 2 mm R-S particles, the measured U_i was 7.2 kV. The corona inception voltage increases considerably with separation between the particle and the electrode [14]. Hence, after the 2 mm particles departed from the electrode, under the 8 kV or 9 kV voltage application, the particles exhibited the immediate lift if the corona discharge was very small or did not exist.

The measured U_i was also about 7.2 kV for the 4 mm R-R particles and 5.8 kV for the 4 mm R-S particles. When the condition that rounded end was rotated up, the charge loss was negligible, and the particles exhibited the immediate lift. When

the condition that sharp end was rotated up, the discharge degree increased. The particle charge was reduced significantly. Hence, the force direction might become downward, resulting in the falling behavior. For the falling behavior, the greater downward force or charge reduction resulted in a larger probability of that the lower end of the particles touched first the grounded electrode. The results from the observation indicate that when the lower end touched the electrode first, the particles tended to exhibit the rotation on the electrode. On the other hand, when the upper end touched the electrode first, the particles tended to bounce on the electrode. As the discharge degree increased with the sharp degree of the ending profile, the incident rate of the rotation increased in the order of the sharp end and the very sharp end, as presented in Figure 7.14. For the S-S particles, after departure the corona discharge occurred more easily at the lower end. This discharge played an important role in forming the rotation behavior on the grounded electrode of the particles.

b) Coated particles

As there was no corona discharge at the coated end, the coated particles moved immediately to the upper electrode without falling after the coated end was rotated up. For the initial movement at both ends with the uncoated end rotating up further, corona discharge might exist at the uncoated end under positive voltage. The degree of the corona discharge was greater for sharper profile and higher applied voltage. Therefore, the lift after falling behavior was usually observed for the particles having the sharp end, and increased with the applied voltage.

After the particle moved initially at the uncoated end, the author supposes that the charge amount on the particle was Q_{ly} in Table 7.5. However, this charge amount might be reduced by the corona discharge at the uncoated end. Four typical values of the particle charge (Q_{ly}, $3Q_{ly}/4$, $Q_{ly}/2$, and 0) are considered for reference. Figure 7.22 shows the total force on the 2 mm and 4 mm particles at δ = 0.05 mm and 0.15 mm, representing two thicknesses of the coating layer. It can be seen from the figure that the force is greater for thicker coating layer. The calculation of the total torque about the contact point **p** indicates that the toque rotates the particle in increasing-α direction when the particle charge is greater than $Q_{ly}/2$. The torque is nearly independent of coating thickness, and reduces when the particle charge decreases.

(a) 2 mm particle at δ = 0.05 mm

(b) 2 mm particle at δ = 0.15 mm

(c) 4 mm particle at δ = 0.05 mm

(d) 4 mm particle at δ = 0.15 mm
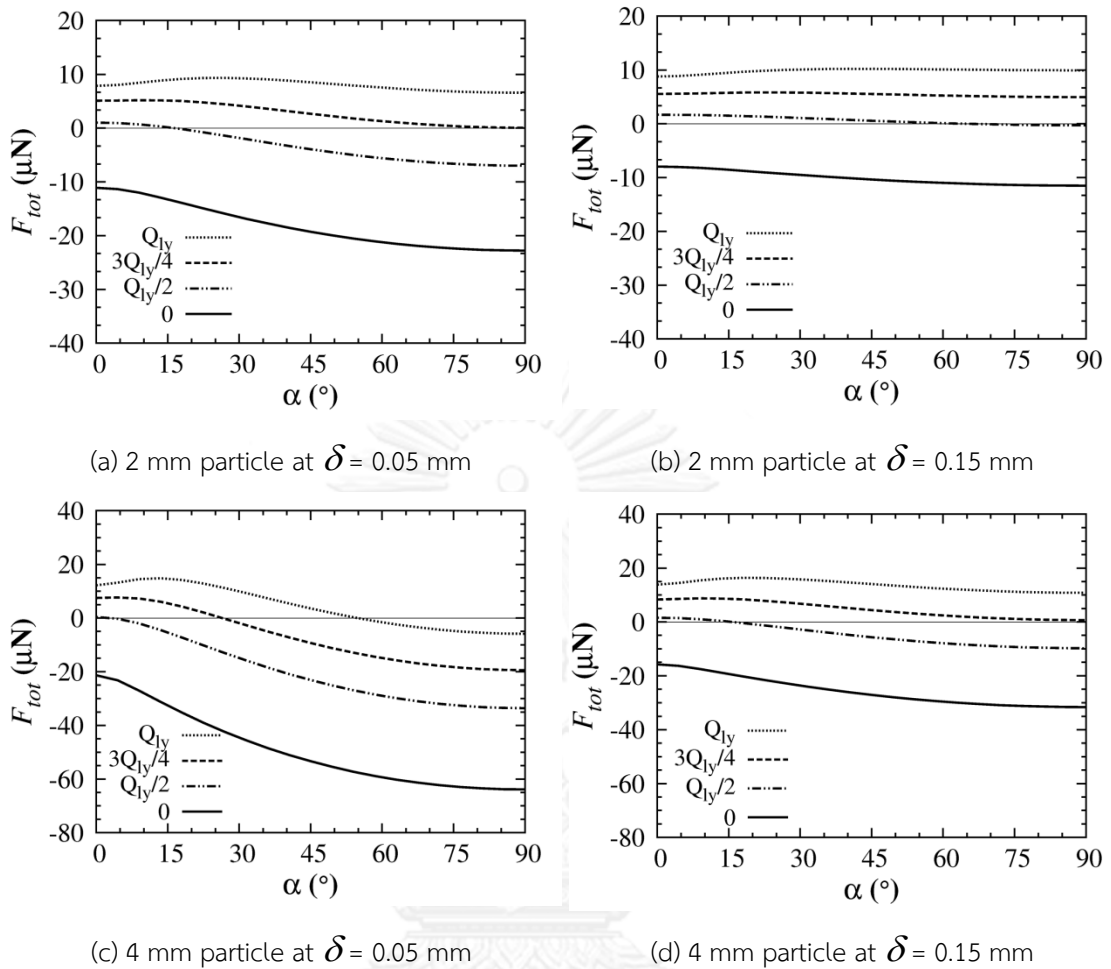
Figure 7.22. Total force on 2 mm and 4 mm particles for two thickness of the coating layer.

The author believed that the subsequent movements, immediate lift, rotation, and bounce, after the initial movement at the uncoated end result from the different degree of corona discharge. After moving initially at the uncoated end, the particles rotated about the coated end to obtain standing position. For the 2 mm particles, the corona discharge might be very small or not exist under negative and positive voltages. As presented in Figure 7.22a, the total force at α about 90° was positive when the particle charge was greater than $3Q_{ly}/4$. Thus, the predominance of the immediate lift behavior of the 2 mm particles under both voltage polarities in Figures 7.17 and 7.18 can be explained.

When the pulling-back torque was not strong enough to exterminate the kinetic energy obtained in the rotating process from α = 0° to 90°, the particles bounced on the electrode. Therefore, for increasing in the discharge degree, the

immediate lift tended to be replaced by the rotation, and the rotation tended to be replaced by the bounce.

For the 4 mm particles under negative voltage, the calculated total force at α = 90° is negative with normal coating thickness (δ = 0.05 mm in Figure 7.22c). Therefore, the particles keep rotating by the increasing-α torque without departure, produce the predominant rotation behavior in Figure 7.17a. On the other hand, the calculated force in Figure 7.22d is positive with thick coating thickness (δ = 0.15 mm in Figure 7.22d) when the particle charge was greater than $3Q_{ly}/4$. The positive force corresponds to the high incident rates of the immediate lift behavior in Figure 7.17a. However, it was unclear why the incident rate was smaller when the voltage was increased to 9 kV.

Under positive voltage, the C-R particles had the corona inception voltage between 8 kV and 9 kV. Thus, with the application of 8 kV, there was no corona discharge, leading to that the particles also usually exhibited the rotation behavior as under negative voltage. This behavior tended to be replaced by the bounce behavior under 9 kV voltage application due to the occurrence of the corona discharge. For the C-S and CC-S particles, as the corona discharge was large due to low U_i, most of their behaviors were the bounce on the electrode as presented in Figure 7.18.

7.3 Summary

For the spheroidal particles, the measured lifting field and the movement behavior did not depend significantly on the electrode gap and the size of the particles. The lifting field from the experiment was greater than the calculated values by 10–15%. Most of the particles moved initially at an end and then departed from the lower electrode at a tilt angle between 35° and 65°. The tendency of the initial movement at an end agreed with the theoretical prediction. However, the measured tilt angle before departure was greater than theoretical values.

For the wire particles, the lifting field from the experiment depended on the ending profile and initial orientation on the grounded electrode of the particles. However, the measured lifting field for different ending profiles and initial orientations deviated slightly from the calculated value. The particles usually moved initially at which the end had a stronger field (or force), as expected, regardless of the polarity of the applied voltage. The probability of the initial movement at both ends (parallel lift) increased with the applied voltage. The movement behavior of a particle after departure from the electrode depended significantly on the initial

movement of the particle and the voltage polarity. The behavior was governed by the degree of the corona discharge on the particle after departure. The calculation results can explain the particle behavior that the corona discharge may result in the change in the force direction on the particle.

CHAPTER VIII

CONCLUSIONS

Contaminating metallic or dielectric particles in gas insulated systems may reduce the insulation performance of the systems. Considerable efforts have been made to investigate the particle-initiated corona discharge, the particle movement, and the methods of particle deactivation. The clear understanding of the particle movement, which is affected significantly by the corona discharge on the particle, is useful in the deactivation of the contaminating particles. This dissertation presents the analysis and experiments related to the particle movement under various conditions.

8.1. Analytical results

In this dissertation, the electromechanics of conducting and dielectric prolate spheroids is analyzed under uniform electric field with the presence of a grounded plane. The spheroid may be in contact with or separated from the plane. The major axis of the spheroid makes a tilt angle with the plane. When the major axis is perpendicular to the plane, the analysis becomes asymmetric. The charge condition is taken into account for floating conducting spheroids. In order to realize high accuracy, the analytical method of multipole images and the multipole re-expansion in prolate spheroidal coordinates are applied to the electric field calculation. The induced charge is determined from the multipole images. The electrostatic force and torque are determined from the stress on the spheroid surface. For axisymmetric configurations, the force can be expressed in a closed form.

For AS configurations, the analysis focuses on the effect of the major-to-minor axis ratio c/b, the separation δ between the spheroid and the plane, and the spheroid-to-medium permittivity ratio ε on electrostatic behaviors. The main results can be summarized as follows:

1. For a conducting spheroid in contact with the plane, the maximal field at the top pole increases nonlinearly with the axis ratio. About 80% of net induced charge resides on the upper half of the spheroid. The force on the lower half is negligible. The charge and the force are compared between the spheroids of the same surface area, the same minor axis, or the same major axis. It is found that the hemispheroidal model can

estimate the charge and force on the spheroid with a difference smaller than 10% when $c/b > 3$.

2. For an uncharged conducting spheroid above the plane, the maximal field at the bottom pole increases significantly with decreasing δ/c from 0.1. Based on the critical field strength of the background medium, the relationship of the critical separation of the spheroid where the partial discharge takes place and the external electric field is investigated. This relationship is approximately linear on the logarithmic scales when δ/c approaches zero.

3. For a charged conducting spheroid above the plane, the maximal field under the fully charged condition hardly varies with δ. The force increases gradually with δ and converges well to the product of the charge and the external field when $\delta/c \geq 10$. The bottom-pole field reduces linearly with increasing the charge amount on the spheroid. When $\delta/c > 1$, the force is repulsive from the plane. When $\delta/c \leq 1$, the force direction depends on the charge amount.

4. For an uncharged dielectric spheroid lying on or above the plane, the maximal field at bottom pole and the force are greater for larger ε. For the same ε, the slender spheroids have larger maximal field. The field and force increases significantly with decreasing δ/c less than 1. With decreasing δ/c close to 0, the force converges more rapidly than the field. The force magnitude is less than that on a conducting spheroid in the same configuration.

For 3D configurations, the purpose of the analysis is to clarify the role of the tilt angle α between the spheroid and the plane on the electrostatic force and torque on the spheroid. The main results can be summarized as follows:

1. For a conducting spheroid in contact with the plane, the maximal field takes place at or near the higher pole of the spheroid for nonzero α. The electrostatic force is minimal at $\alpha = 0°$, and increases nonlinearly with α to the maximum at 90°. The electrostatic torque is in the increasing-α direction. It varies as a parabolic function of α and obtains the maximum at α about 45°. When the gravitational force of the spheroid is taken into account, the electromechanical behavior can be classified into three

regimes, depending on the externally applied field and the tilt angle. The presence of the electrostatic torque enhances the probability of the spheroid to be lifted from the grounded plane.

2. For a fully charged conducting spheroid above the plane, the variation of the electrostatic force and torque about the center **o** with α is similar to that when the spheroid is in contact with the plane. The force and torque increase slightly with increasing δ. The torque about **o** of a floating spheroid is smaller than that about the contact point **p** of a grounded spheroid.

3. For the uncharged dielectric spheroid with c/b = 2 and ε = 2 in contact with the plane, the electric field is maximal at the contact point **p** for all α values. The force is maximal at α = 0°, and reduces nonlinearly with α to the minimum at 90°. The torque about **p** always tends to rotate the spheroid to the standing position, similarly to the case of the conducting spheroid.

8.2 Experimental results

Experiments were done for the lifting electric field and the movement behavior of aluminum prolate spheroidal and wire particles. Two sizes of the spheroidal particles of 4 mm length were used. The wire particles have 2 or 4 mm length and different ending profiles: rounded, sharp, very sharp, coated, and thickly coated ones.

The experimental results of the spheroidal particles were compared with the analytical results. The measured lifting field and the movement behavior did not depend significantly on the electrode gap and the particle size. Most of the spheroidal particles moved initially at an end and then departed from the lower electrode at a tilt angle between 35° and 65°. The measured lifting field was greater than the calculated values by 10–15%. The tendency of the initial movement at an end agreed with the theoretical prediction. However, the tilt angle at which the particle departed from the electrode was greater than theoretical values.

The wire particles were used to investigate the effects of the particle profile and the corona discharge on the movement behavior of non-spherical conducting particles under electric field. The measured lifting field depended on the ending profile and initial orientation on the grounded electrode of the particles. The particles usually moved initially at which the end had a stronger field (or force). The

probability of the initial movement at both ends (parallel lift) increased with the applied voltage. The movement behavior of a particle after departure from the electrode depended on the initial movement and the voltage polarity. The behavior was governed by the degree of the corona discharge on the particle after departure. The corona discharge was measured for fixed and movable particles to examine the degree of corona discharge at the particle ends. The force and torque on the particle were estimated by using the prolate spheroidal model for various conditions. The charge amount on the particle was varied in the analysis to reflect the charge losses due to corona discharge.

This dissertation contributes the understanding of the movement behavior of metallic non-spherical particles in gas insulated systems with presence of the corona discharge on the particles. Moreover, the analytical results in this dissertation can be used for the applications of electrostatics and dielectric materials which concern prolate spheroidal particles and require accurate quantities of electrostatic behaviors such as electric field, force, and torque on the particles.

REFERENCES

1. Fujimoto, N. and G.L. Ford, Results of recent GIS fault survey, in IERE Workshop on Gas Insulated Substations. 1996. p. 1.1–1.7.
2. Indira, M.S. and T.S. Ramu, Motion of conducting particles causing inadvertent outages in GIS. Ieee Transactions on Dielectrics and Electrical Insulation, 2000. **7**(2): p. 247-253.
3. Cooke, C.M., Particle contamination in compressed gas insulations, limitations and control. 1978, Gaseous dielectrics I. p. 162–187.
4. Laghari, J.R. and A.H. Qureshi, Surface Flashover of Spacers in Compressed Gas Insulated Systems. Electrical Insulation, IEEE Transactions on, 1981. **EI-16**(5): p. 373-387.
5. Brown, G.W., R. Samm, and J. Cronin, AC Analysis and Testing of Realistically Contaminated Fas-Insulated Systems. Power Apparatus and Systems, IEEE Transactions on, 1978. **PAS-97**(1): p. 59-67.
6. Research, W.E.C., D. Center, W. Research, D. Center, R.E. Wootton, and E.P.R. Institute, Investigation of High-voltage Particle-initiated Breakdown in Gas-insulated Systems. 1979: Electric Power Research Institute.
7. Morcos, M.M., S.A. Ward, H. Anis, K.D. Srivastava, and S.M. Gubanski, Insulation integrity of GIS/GITL systems and management of particle contamination. Electrical Insulation Magazine, IEEE, 2000. **16**(5): p. 25-37.
8. Takuma, T. and B. Techaumnat, eds. Electric Fields in Composite Dielectrics and their Applications. 2010, Springer, Netherland. 178.
9. Chakrabarti, A.K., R.G. Van Heeswijk, and K.D. Srivastava, Spacer Involvement in Conducting-Particle-Initiated Breakdown in Compressed Gas Insulated Systems. Electrical Insulation, IEEE Transactions on, 1987. **EI-22**(4): p. 431-438.
10. Hampton, B.F. and S.P. Fleming, Impulse flashover of particle-contaminated spacers in compressed sulphur hexafluoride. Electrical Engineers, Proceedings of the Institution of, 1973. **120**(4): p. 514-518.
11. Kuwahara, H., S. Inamura, T. Watanabe, and Y. Arahata, Effect of Solid Impurities on Breakdown in Compressed SF6 Gas. Power Apparatus and Systems, IEEE Transactions on, 1974. **PAS-93**(5): p. 1546-1555.
12. Asano, K., K. Yatsuzuka, and T. Yamaki, DC corona discharge of a metal filament particle within parallel-plate electrodes. Industry Applications, IEEE Transactions on, 2000. **36**(1): p. 87-92.

13.   Asano, K., R. Hishinuma, and K. Yatsuzuka, Bipolar DC corona discharge from a floating filamentary metal particle. Industry Applications, IEEE Transactions on, 2002. **38**(1): p. 57-63.

14.   Kudo, Y., T. Sugimoto, and Y. Higashiyama, DC corona discharge from a wire particle floated with a microgap in parallel plate electrodes. Industry Applications, IEEE Transactions on, 2006. **42**(4): p. 909-915.

15.   Hara, M., Y. Negara, M. Setoguchi, T. Kurihara, J. Suehiro, and N. Haashi, Particle-triggered pre-breakdown phenomena in atmospheric air gap under AC voltage. Dielectrics and Electrical Insulation, IEEE Transactions on, 2005. **12**(5): p. 1071-1081.

16.   Akazaki, M. and M. Hara, Mechanisms and characteristics of DC corona from floating particle. Electrical Engineering in Japan, 1970. **90**(4): p. 131-141.

17.   Negara, Y., K. Yaji, K. Imasaka, N. Hayashi, J. Suehiro, and M. Hara, AC particle-triggered corona discharge in low pressure SF_6 gas. Dielectrics and Electrical Insulation, IEEE Transactions on, 2007. **14**(1): p. 91-100.

18.   Negara, Y., K. Yaji, J. Suehiro, N. Hayashi, and M. Hara, DC corona discharge from floating particle in low pressure SF_6. Dielectrics and Electrical Insulation, IEEE Transactions on, 2006. **13**(6): p. 1208-1216.

19.   Hara, M., H.H. Lee, and T. Egashira, Effect of electrode shape on particle-initiated breakdown in SF_6 gas under DC voltage. Electrical Insulation, IEEE Transactions on, 1991. **26**(1): p. 156-170.

20.   Khan, A., Y. Khan, N.H. Malik, and A.A. Al-Arainy, Influence of Spacer Defects and Adhered Metal Particles on Electric Field Intensifications in GIS. Journal of Basic and Applied Scientific Research, 2012. **2**(8): p. 7866-7875.

21.   Cooke, C.M., R.E. Wootton, and A.H. Cookson, Influence of particles on AC and DC electrical performance of gas insulated systems at extra-high-voltage. Power Apparatus and Systems, IEEE Transactions on, 1977. **96**(3): p. 768-777.

22.   Asano, K., K. Anno, and Y. Higashiyama, The behavior of charged conducting particles in electric fields. Industry Applications, IEEE Transactions on, 1997. **33**(3): p. 679-686.

23.   Félici, N.J., Forces et charges de petits objets en contact avec une électrode affectée d'un champ électrique. Rev. Gén. Elec., 1966. **75**(10): p. 1145-1160.

24.   Hara, M. and M. Akazaki, A method for prediction of gaseous discharge threshold voltage in the presence of a conducting particle. Journal of Electrostatics, 1977. **2**(3): p. 223-239.

25.   Sakai, K.I., D.L. Abella, Y. Khan, J. Suehiro, and M. Hara, Experimental studies of free conducting wire particle behavior between nonparallel plane electrodes with AC voltages in air. Dielectrics and Electrical Insulation, IEEE Transactions on, 2003. **10**(3): p. 418-424.

26.   Cooke, C.M. and A.H. Cookson, The Nature and Practice of Gases as Electrical Insulators. Electrical Insulation, IEEE Transactions on, 1978. **EI-13**(4): p. 239-248.

27.   Sakai, K.I., D.L. Abella, Y. Khan, J. Suehiro, and M. Hara, Theoretical and experimental studies for spherical free-conducting particle behavior between nonparallel plane electrodes with AC voltages in air. Dielectrics and Electrical Insulation, IEEE Transactions on, 2003. **10**(3): p. 404-417.

28.   Sakai, K., S. Tsuru, D.L. Abella, and M. Hara, Conducting particle motion and particle-initiated breakdown in dc electric field between diverging conducting plates in atmospheric air. Dielectrics and Electrical Insulation, IEEE Transactions on, 1999. **6**(1): p. 122-130.

29.   Holmberg, M.E. and S.M. Gubanski, Motion of metallic particles in gas insulated systems. Electrical Insulation Magazine, IEEE, 1998. **14**(4): p. 5-14.

30.   Higashiyama, Y., Y. Kudo, and K. Asano, Influence of Corona Discharge from a Wire Particle Located in a DC Electric Field on its Precessional Motion. IEEJ Transactions on Fundamentals and Materials, 2007. **127**(11): p. 724-728.

31.   Kudo, Y., T. Sugimoto, and Y. Higashiyama, Corona and Micro-gap Discharge occurring at a Wire Particle in a Precessional Motion under a DC Electric Field. IEEJ Transactions on Fundamentals and Materials, 2005. **125**(2): p. 107-112.

32.   Diessner, A. and J.G. Trump, Free Conducting Particles in a Coaxial Compressed-Gas-Insulated System. Power Apparatus and Systems, IEEE Transactions on, 1970. **PAS-89**(8): p. 1970-1978.

33.   Sakai, K.I., D. Labrado Abella, J. Suehiro, and M. Hara. Lateral motion of wire particles toward decreasing electrode gap regions in atmospheric air. in Properties and Applications of Dielectric Materials, 2000. Proceedings of the 6th International Conference on. 2000.

34.   Khan, Y., K.I. Sakai, E.K. Lee, J. Suehiro, and M. Hara, Motion behavior and deactivation method of free-conducting particle around spacer between diverging conducting plates under DC voltage in atmospheric air. Dielectrics and Electrical Insulation, IEEE Transactions on, 2003. **10**(3): p. 444-457.

35.   Morcos, M.M., S.A. Ward, and H. Anis. On the detection and control of metallic particle contamination in compressed GIS equipment. in Electrical Insulation and Dielectric Phenomena, 1998. Annual Report. Conference on. 1998.

36.   Dale, S.J. and M.D. Hopkins, Methods of Particle Control in SF_6 Insulated CGIT Systems. Power Apparatus and Systems, IEEE Transactions on, 1982. **PAS-101**(6): p. 1654-1663.

37.   Morcos, M.M. and K.D. Srivastava, On electrostatic trapping of particle contamination in GITL systems. Power Delivery, IEEE Transactions on, 1992. **7**(4): p. 1698-1705.

38.   Pace, M.O., J.L. Adcock, and L.G. Christophorou. New particle control techniques for gas-insulated apparatus. in Proceeding of 4th International Symposium on High Voltage Engineering. 1983. Athens.

39.   Khan, Y., S. Okabe, J. Suehiro, and M. Hara, Proposal for new particle deactivation methods in GIS. Dielectrics and Electrical Insulation, IEEE Transactions on, 2005. **12**(1): p. 147-157.

40.   Hasegawa, T., K. Yamaji, M. Hatano, F. Endo, T. Rokunohe, and T. Yamagiwa, Development of insulation structure and enhancement of insulation reliability of 500 kV DC GIS. Power Delivery, IEEE Transactions on, 1997. **12**(1): p. 194-202.

41.   Phansiri, N. and B. Techaumnat, Study on the electromechanics of a conducting particle under nonuniform electric field. Dielectrics and Electrical Insulation, IEEE Transactions on, 2013. **20**(2): p. 488-495.

42.   Srivastava, K.D. and R.G. Van Heeswijk, Dielectric Coatings-Effect on Breakdown and Particle Movement in Gitl Systems. Power Apparatus and Systems, IEEE Transactions on, 1985. **PAS-104**(1): p. 22-31.

43.   Parekh, H., K.D. Srivastava, and R.G. Van Heeswijk, Lifting Field of Free Conducting Particles in Compressed SF_6 with Dielectric Coated Electrodes. Power Apparatus and Systems, IEEE Transactions on, 1979. **PAS-98**(3): p. 748-758.

44.   Ooishi, T., M. Yoshimura, H. Hama, H. Fujii, and K. Nakanishi, Charging mechanisms of a conducting particle on dielectric coated electrode at AC and DC electric fields. 1994, Gaseous dielectrics VII, Plenum Press, New York. p. 585-592.

45.   Honda, M., H. Okubo, H. Aoyagi, and A. Inui, Impulse Breakdown Characteristics of Coated Electrodes in SF6 Gas. Power Delivery, IEEE Transactions on, 1987. **2**(3): p. 699-708.

46.   Edwards, H.M., Riemann's Zeta Function. 2001, Dover Publication Inc, New York.

47.   Smythe, W.R., Static and dynamic electricity. 1950, 2nd ed., McGRAW-HILL, New York.

48.   Kai, Z. and S. Boggs, Uniform field charge on a conducting particle. Dielectrics and Electrical Insulation, IEEE Transactions on, 2009. **16**(4): p. 1158-1159.

49.   Kai, Z. and S. Boggs, Derivation of exact and approximate formulas for the force on a conducting particle standing on a ground plane, and comparison with finite element computations. Dielectrics and Electrical Insulation, IEEE Transactions on, 2010. **17**(5): p. 1602-1606.

50.   Khan, Y., A. Oda, S. Okabe, J. Suehiro, and M. Hara, Wire Particle Motion Behavior and Breakdown Characteristics around Different Shaped Spacers within Diverging Air Gap. IEEJ Transactions on Power and Energy, 2003. **123**(11): p. 1288-1295.

51.   Hirsh, M.N. and H.J. Oskam, Gaseous Electronics. Volume 1. 1978, Electrical Discharges, Academic Press, New York.

52.   Meek, J.M. and J.D. Craggs, Electrical Breakdown of Gases. 1953, Oxford at The Clarendon Press.

53.   Chen, J., Direct current corona-enhanced chemical reactions. 2002, Ph.D. thesis, Univ. of Minnesota, USA.

54.   Sattari, P., C.F. Gallo, G.S.P. Castle, and K. Adamiak, Trichel pulse characteristics—negative corona discharge in air. Journal of Physics D: Applied Physics, 2011. **44**(15): p. 1-11.

55.   Goldman, M., A. Goldman, and R.S. Sigmond, The corona discharge, its properties and specific uses. Pure and Applied Chemistry, 1985. **57**(9): p. 1353–1362.

56.   Chang, J.S., P.A. Lawless, and T. Yamamoto, Corona discharge process. IEEE Transactions on Plasma Science, 1991. **19**(6): p. 1152-1166.

57.   Sigmond, R.S., The Oscillations of the Positive Glow Corona. J. Phys. IV France, 1997. **7**(4): p. 383-395.

58.   Zentner, R., Ober die Anstiegzeiten der negativen korona entladung simpulse 2 angew. Journal of Mathematical Physics, 1970. **29**: p. 294-301.

59.   Soria, C., F. Pontiga, and A. Castellanous, Particle-in-cell simulation of Trichel pulses in pure oxygen. Journal of Physics D: Applied Physics, 2007. **40**(15): p. 4552–4560.

60.   C. Soria, F.P., and A. Castellanous, Numerical simulation of Trichel pulses in low pressure oxygen. 2001, Annual Report Conference on Electrical Insulation and Dielectric Phenomena. IEEE.

61.   Budiman, H. and J. Talib, Prolate Spheroidal Coordinate: An Approximation To Modeling Of Ellipsoidal Drops In Rotating Disc Contractor Column. Journal of Science and Technology, 2011. **3**(1): p. 87–95.

62.	Moon, P. and D.E. Spencer, Field Theory Handbook, Including Coordinate Systems, Differential Equations and Their Solutions. 1988, 2nd ed. New York: Springer-Verlag.

63.	Satterly, J., Formulae for volumes, surface areas and radii of gyration of spheres, ellipsoids and spheroids. The Mathematical Gazette, 1960. **44**: p. 15–19.

64.	Techaumnat, B. and M. Washizu, Equivalent image charges of a prolate spheroid under an external electric field. Journal of Electrostatics, 2011. **69**(4): p. 388–393.

65.	Griffiths, D.J. and R. College, Introduction to electrodynamics. 1999, 3rd ed. Prentice Hall.

66.	Prudnikov, A.P., Y.A. Brychkov, and O.I. Marichev, Integrals and series, volume 2: special functions. 1986, USSR Academy of Sciences Moscow.

67.	Jones, T.B., Electromechanics of particles. 1995, Cambridge University Press. p. 222–226.

68.	Washizu, M. and T.B. Jones, Dielectrophoretic interaction of two spherical particles calculated by equivalent multipole-moment method. Industry Applications, IEEE Transactions on, 1996. **32**(2): p. 233-242.

69.	Morse, P.M. and H. Feshbach, Method of theoretical physics. 1953, McGraw-Hill Book Company.

70.	Crichton, G.C., A. Karlsson, and A. Pedersen, Partial discharges in ellipsoidal and spheroidal voids. Electrical Insulation, IEEE Transactions on, 1989. **24**(2): p. 335-342.

71.	McAllister, I.W., Partial discharges in spheroidal voids. Void orientation. Dielectrics and Electrical Insulation, IEEE Transactions on, 1997. **4**(4): p. 456-461.

72.	Techaumnat, B. and T. Takuma, Electric field and force on a conducting sphere in contact with a dielectric solid. Journal of Electrostatics, 2006. **63**(3-4): p. 165–175.

73.	Hara, M. and M. Akazaki, Analysis of microdischarge threshold conditions between a conducting sphere and plane. Journal of Electrostatics, 1982. **13**(2): p. 105–118.

74.	Ono, T., D.Y. Sim, and M. Esashi, Micro-discharge and electric breakdown in a micro-gap. Journal of Micromechanics and Microengineering, 2000. **10**(3): p. 445–451.

APPENDICES

Appendix A: Calculation Accuracy of Axisymmetric Configurations

Although the method of multipole images is an analytical method, numerical errors exist because only a finite number of harmonics, (n = 0, 1, $\cdots$, N) used in the calculation. The N = 1 case represents the dipole approximation. The calculation accuracy is improved with increasing N.

This appendix considers the variation of calculation accuracy with N for the axisymmetric configuration of a conducting or dielectric spheroid in Figure 3.2b. As the harmonic potentials naturally satisfy the Laplace equation, the accuracy of the calculation results is evaluated from the boundary conditions on the grounded plane and on the spheroid surface. In all cases of calculation, the zero potential condition on the plane is well negligible. Hence, the evaluation of the boundary conditions was done on the spheroid surface. In addition, the author has confirmed that with $c/b \longrightarrow 1$, the calculation results converge well to the analytical solutions for the case of a conducting sphere [23, 24] and that of a dielectric sphere [68] in the corresponding configurations.

A1. Configuration of conducting spheroids

For the configurations of the conducting spheroid, the potential ψ and its average value ψ_{avg} on the spheroid surface are calculated. To evaluate the calculation accuracy, the error *err* between ψ and ψ_{avg},

$$err = \psi - \psi_{avg},\tag{A1}$$

and the mean squared error ω,

$$\omega = \frac{1}{S} \oiint_S err^2 dS \,,\tag{A2}$$

are taken into account.

For the configuration of a grounded spheroid, Figure A1 presents the variation of the maximal error, max{|err|}, with N from 1 to 1000 on the logarithm scales for c/b = 1, 10, and 32. The error in the figure is normalized by cE_0. It is clear from the figure that the maximal error reduces considerably with increasing N. With $N \geq 20$, we can achieve max{|err|} $\leq 2 \times 10^{-4} cE_0$ for the values of c/b up to 32. max{|err|} in Figure A1 is smaller for lower c/b. The result of the mean squared error ω is shown in

Figure A2. The variation with *N* and *c/b* of ω is similar to that of max{|err|}. With *N* ≥ 20, ω is less than 10^{-8} for the range *c/b*.
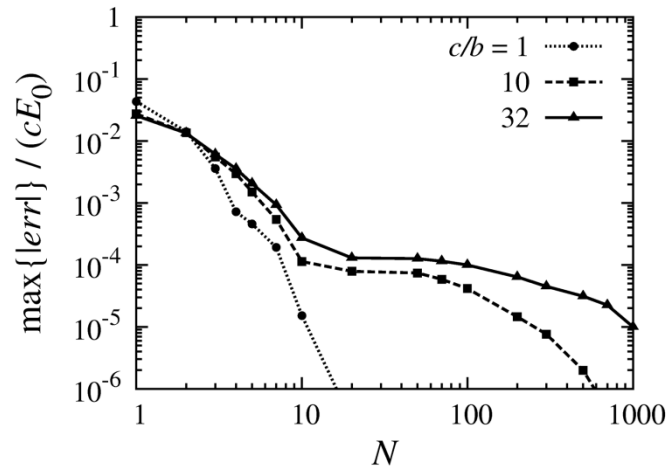

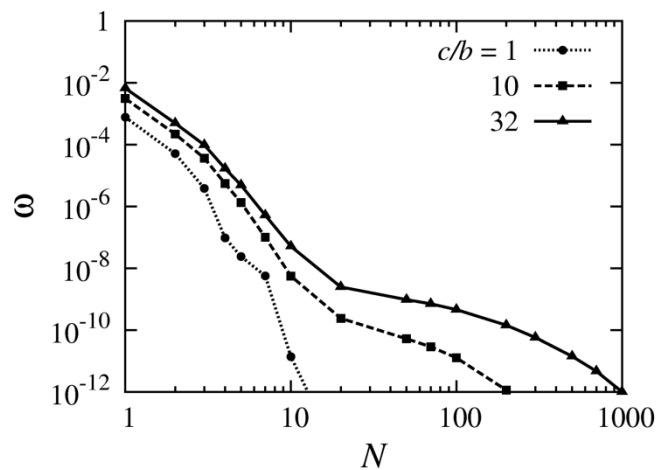Figure A1. Maximal error of the potential on a grounded conducting spheroid.

Figure A2. Mean squared error of the potential on a grounded conducting spheroid.

For the configuration of the electrically floating case, uncharged spheroid with two values of the separation is considered here as a reference. The calculation results of the maximal error, max{|err|}, for δ/c = 0.1 and 0.01 are presented in Figures A3a and A3b, respectively. As shown in Figure A3a for δ/c = 0.1, max{|err|} decreases significantly when *N* increases from 5 to 30. It is smaller than $10^{-4}cE_0$ when *N* ≥ 20. As shown in Figure A3b for δ/c = 0.01, max{|err|} reduces more slowly than that in Figure A3a for δ/c = 0.1. To obtain max{|err|} ≤ $10^{-4}cE_0$, *N* > 200 is required.

The calculation results of the mean squared error ω for δ/c = 0.1 and 0.01 are presented in Figures A4a and A4b, respectively. The figures indicate that the variation with N and c/b of ω is similar to that of max{|err|} for both the separations. To achieve $\omega \le 10^{-8}$ for the range c/b, N must be larger than 20 for δ/c = 0.1 and 70 for δ/c = 0.01. The results in Figures A3 and A4 confirm that the calculation accuracy is improved with increasing the separation.
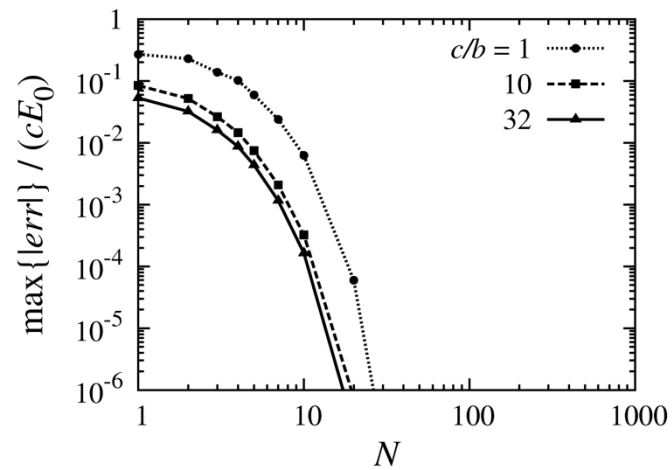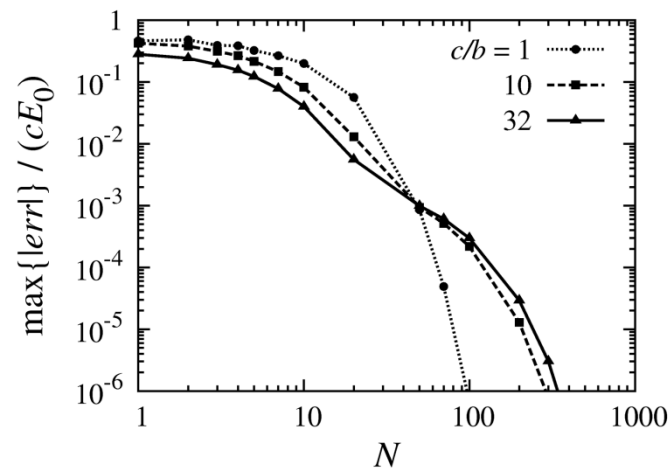

(a) δ/c = 0.1

(b) δ/c = 0.01

Figure A3. Maximal error of the potential on an uncharged floating conducting spheroid.
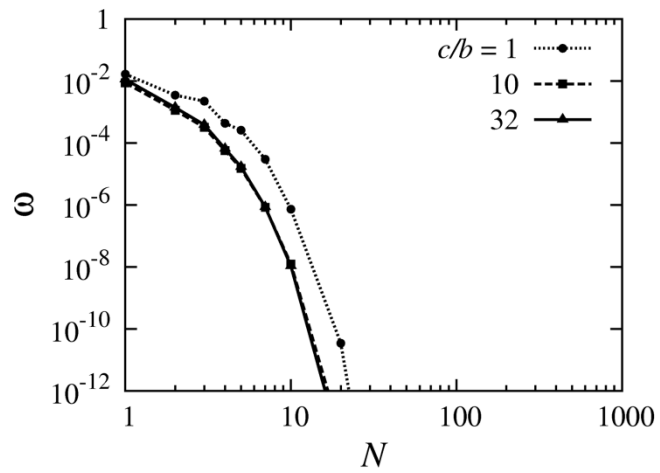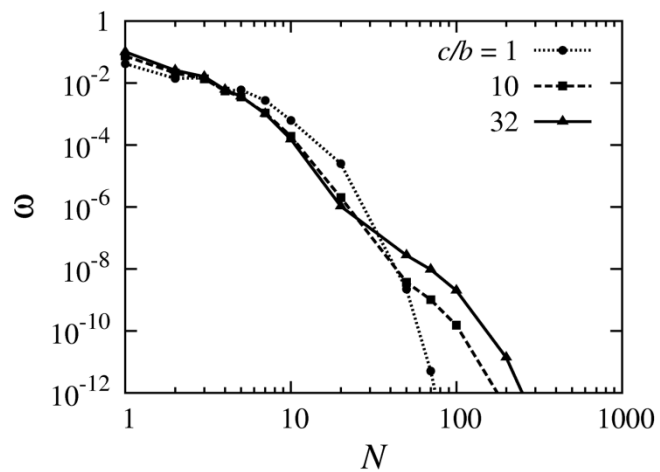
(a) $\delta/c = 0.1$

(b) $\delta/c = 0.01$

Figure A4. Mean squared error of the potential on an uncharged floating conducting spheroid.

A2. Configuration of dielectric spheroids

The configuration of a dielectric spheroid lying on the grounded plane usually requires a higher *N* value in comparison with that of the spheroid separated from the plane for the same accuracy. The author considers here only the case that the spheroid is in contact with the plane. The obtained result can be used as a reference for other case. For the configuration of the spheroid, the error is defined as

$$err = \frac{K_e - \varepsilon}{\varepsilon} \, , \tag{A3}$$

where K_e is the ratio of the normal electric field on the spheroid surface.

Figure A5a presents the variation of the maximal error, max{|err|}, with *N* from 1 and 1000 on the logarithm scales when *c/b* = 1 (sphere). It is obvious from the figure that max{|err|} reduces significantly when *N* increases from 10 to 100. max{|err|} converges well to its limiting values as $N \geq 300$. These values are smaller than 10^{-5}. Figures A5b and A5c show the result for the cases of *c/b* = 2 and 4, respectively. We can see that max{|err|} in these figures reduces more slowly than that in Figure A5a. max{|err|} does not converge even at *N* = 1000, except the case of *c/b* = 2 and ε = 2. For the same *N* value, the accuracy is lower for the spheroids with higher values of *c/b* and ε. For the ranges of *c/b* and ε considered here, the maximal error is less than 0.005 when $N \geq 500$.

The calculation results of the mean squared error ω are presented in Figure A6. The figure implies that the variation of ω with *N* smaller than 200 is quite similar for different values of *c/b* and ε. That is, ω oscillates with *N* between 1 and 20, and reduces considerably with *N* increasing from 20 to 200. With *N* = 200, ω is smaller than 10^{-7}. For *N* > 200, ω converges for *c/b* = 1 but oscillates for *c/b* = 2 and 4.
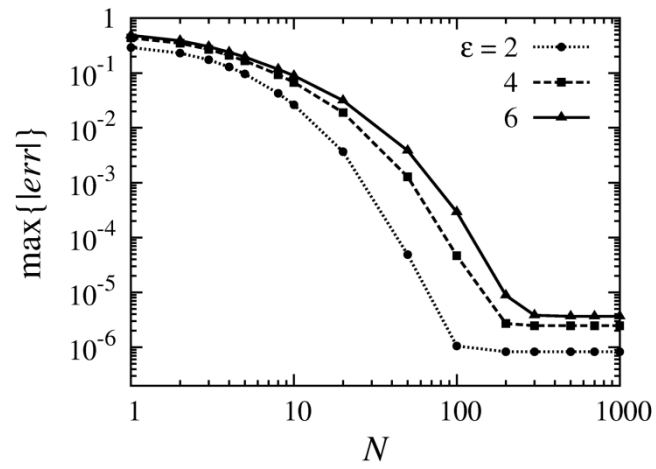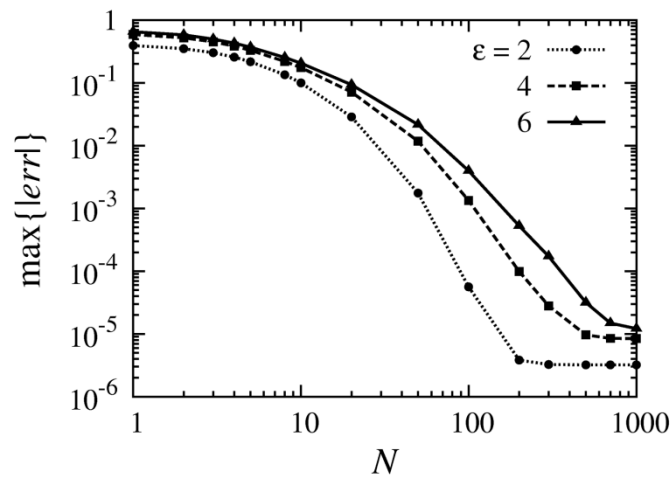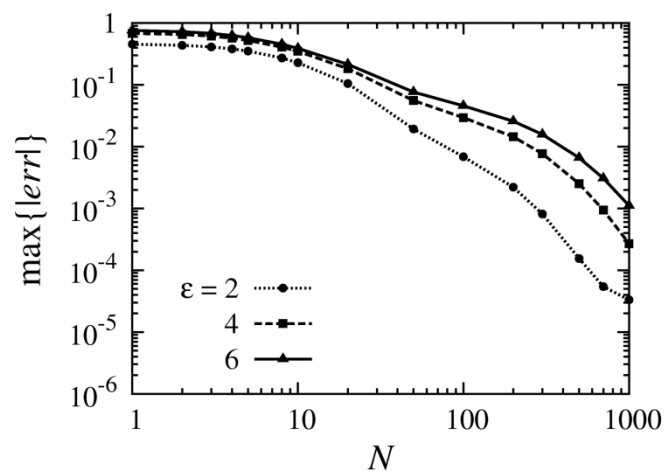
(a) *c/b* = 1

(b) *c/b* = 2

(c) *c/b* = 4

Figure A5. Maximal error of the normal electric field on the surface of the dielectric spheroid lying on the grounded plane.
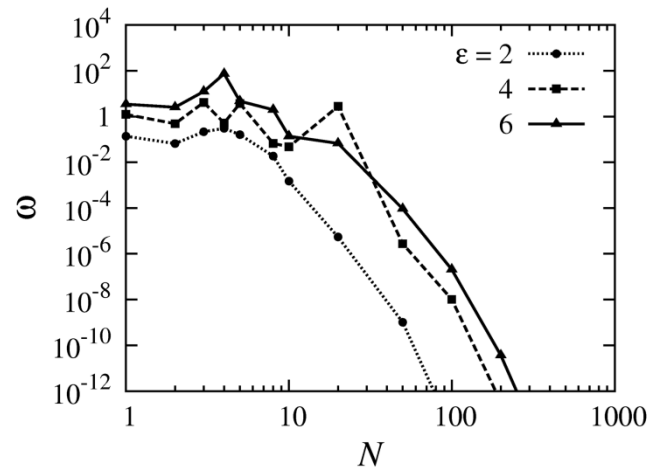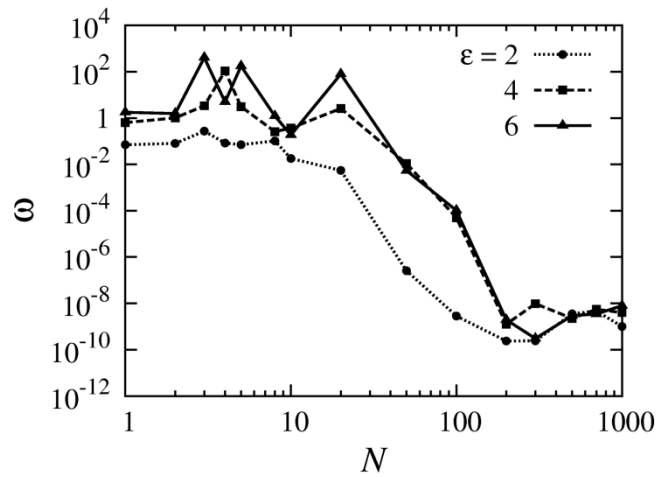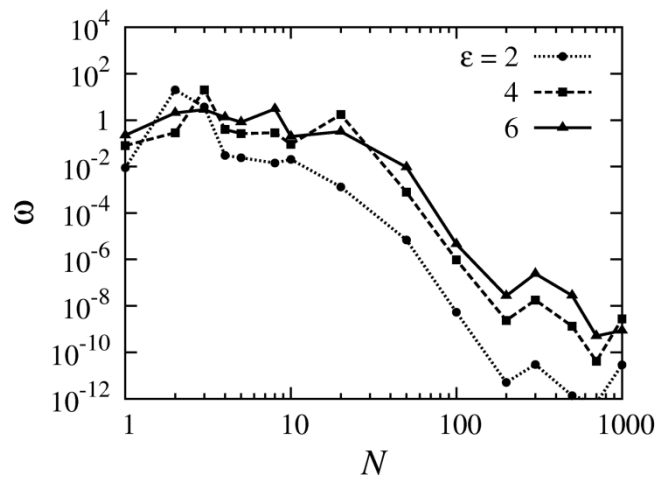
(a) *c/b* = 1

(b) *c/b* = 2

(c) *c/b* = 4

Figure A6. Mean squared error of the normal electric field on the surface of the dielectric spheroid lying on the grounded plane.

Appendix B: Calculation of Lifting and Rotating Fields

This appendix derives the lifting and rotating fields of conducting spheroidal particles in contact with a grounded plane. The lifting field is determined from the electrostatic and gravitational forces on the spheroid. The torques about the contact point produced by the forces is applied to calculate the rotating field. The result shows that the lifting and rotating fields are a function of the square root of the mass density of the particle. The ratio of the rotating field to the lifting field is independent of the material and the size of the particle.

B1. Lifting field E_L

Consider a conducting spheroidal particle in contact with a grounded plane under external field E_0. The minor semi-axis and major semi-axis of the particle are b and c, respectively. The major axis makes tilt angle α with the grounded plane. The electrostatic force F_e on the particle can be expressed as

$$F_e = k_f(c/b, \alpha) \left[4\pi\varepsilon_E b^2 E_0^2 \right],$$

(B1)

where $k_f(c/b, \alpha)$ is presented in Figure 5.5.

The gravitational force of the particle is

$$F_g = \frac{4}{3}\pi c b^2 \rho g .$$

(B2)

At tilt angle α between 0° and 90°, the lifting field E_L of the particle is determined from the balance of F_e and F_g,

$$E_L = \sqrt{\frac{1}{3} \frac{c\rho g}{\varepsilon_E k_f(c/b, \alpha)}} .$$

(B3)

B2. Rotating field E_R

The electrostatic torque $T_{e,\mathbf{p}}$ on the particle about the contact point $\mathbf{p}$ between the particle and the grounded plane is

$$T_{e,\mathbf{p}} = k_t(c/b, \alpha) \left[4\pi\varepsilon_E b^3 E_0^2 \right],$$

(B4)

where $k_t(c/b, \alpha)$ is shown in Figure 5.7. The gravitational torque $T_{g,\mathbf{p}}$ about the contact point $\mathbf{p}$ is determined as

$$T_{g,\mathbf{p}} = -F_g d = -\frac{4}{3}\pi c b^2 \rho g \frac{(c^2 - b^2)\sin\alpha}{\sqrt{b^2 + c^2 \tan^2\alpha}},$$

(B5)

where d is the horizontal distance between the particle center and the contact point defined in equation (3.9).

At tilt angle α between 0° and 90°, the critical rotating field E_R of the particle is

$$E_R = \sqrt{\frac{1}{3}\frac{c\rho g}{\varepsilon_E k_t(c/b,\alpha)}\frac{\left[\left(\frac{c}{b}\right)^2 - 1\right]\sin\alpha}{\sqrt{1 + \left(\frac{c}{b}\right)^2\tan^2\alpha}}} \ . \tag{B6}$$

B3. Field ratio

From equations (B3) and (B6), we can see that E_L and E_R are directly proportional to the square root of the mass density ρ. The ratio of E_R to E_L is

$$\frac{E_R}{E_L} = \sqrt{\frac{k_f(\frac{c}{b},\alpha)}{k_t(\frac{c}{b},\alpha)}\frac{\left[\left(\frac{c}{b}\right)^2 - 1\right]\sin\alpha}{\sqrt{1 + \left(\frac{c}{b}\right)^2\tan^2\alpha}}} \ . \tag{B7}$$

Equation (B7) indicates that the ratio E_R/E_L is a function of the axis ratio c/b and the tilt angle α. The ratio does not depend on the material and the size of the particle.

Appendix C: Corona Discharge Measurement

This appendix presents the corona discharge measurement in atmospheric air for the uncoated and coated wire particles described in Table 6.2. Electrode gap used in the measurement was 10 mm. The corona current pulses were detected by using the trigger feature of an oscilloscope. The experiments in this appendix were carried out at the high voltage laboratory, the University of Tokyo. The experimental setup and experimental equipments of the measurement are mentioned in Chapter VI.

C1. Corona inception voltage

For the measurement of the corona inception voltage U_i, a wire particle was set to stand on the lower (grounded) electrode. A small silicone piece was used to fix the particle on the electrode. As the lower end of the uncoated particle touched the electrode, the ending shape did not affect the inception of the corona discharge at the upper end. The applied voltage was increased gradually until the corona discharge at the upper end occurred. The polarity of the corona discharge was positive under a negative voltage application and negative under a positive voltage application. In this dissertation, U_i was defined as the applied voltage at the time when the first corona pulse was detected.

The experiments were carried out for uncoated particles with the R-R, R-S, and R-SS profiles and coated particles with the C-R and C-S profiles. The sharper end was set to be the upper end for the uncoated particles. Two samples were used for each ending profile. Every sample was subject to 10 tests for each voltage polarity.

Figure C1 presents U_i of the uncoated and coated particles with different profiles of the upper end. The maximum, minimum, and average values are given on the graphs. The average values are represented by void circles or triangles. It is clear from Figure C1 that U_i was higher under negative voltage than under positive voltage for all particles. For the 4 mm particles, U_i decreased as the upper end became sharper.
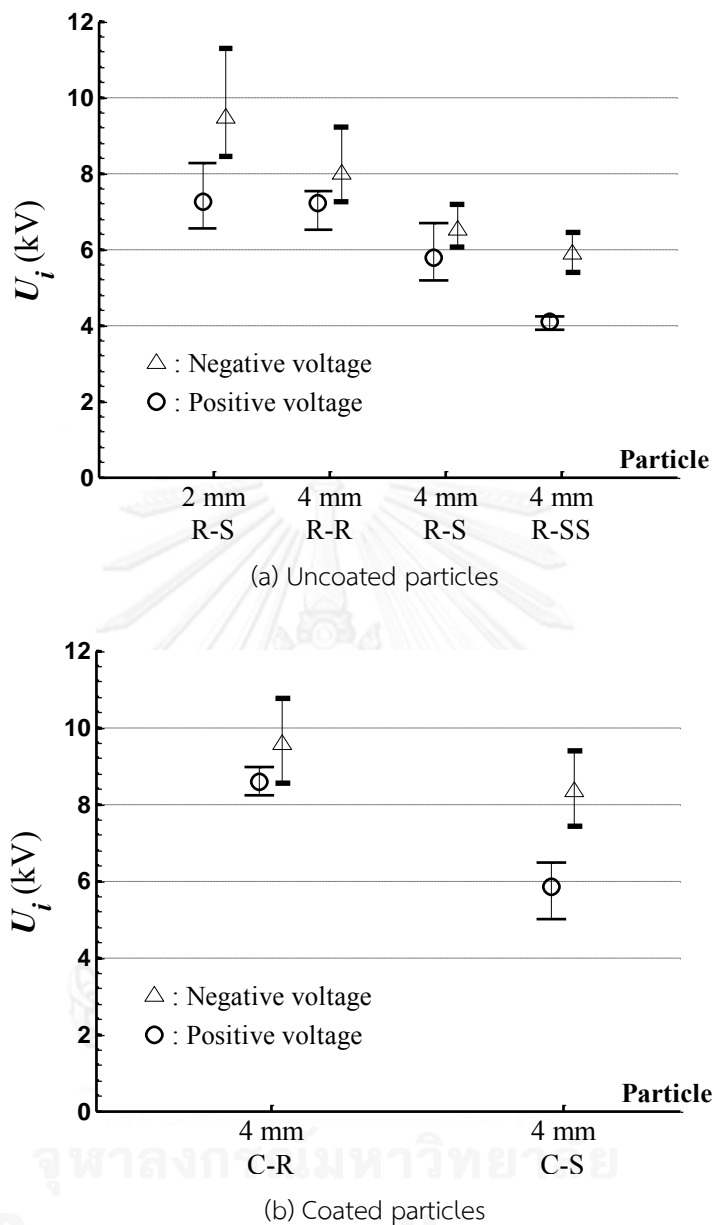
Figure C1. Corona inception voltage of the uncoated and coated particles.

The number of corona current pulses associated with the discharge was random. Figure C2 presents the measured waveform of the corona current i_c in a 200 μs interval. Note that, the direction from the upper to lower electrodes is referred to the positive direction of the current. The charge amount Q_c of the first corona current pulse was calculated by numerically integrating the current pulse with respect to time. The results are presented in Figure C3. It is obvious from the figure that Q_c under negative voltage was about two orders larger than that under positive voltage for both uncoated and coated particles.
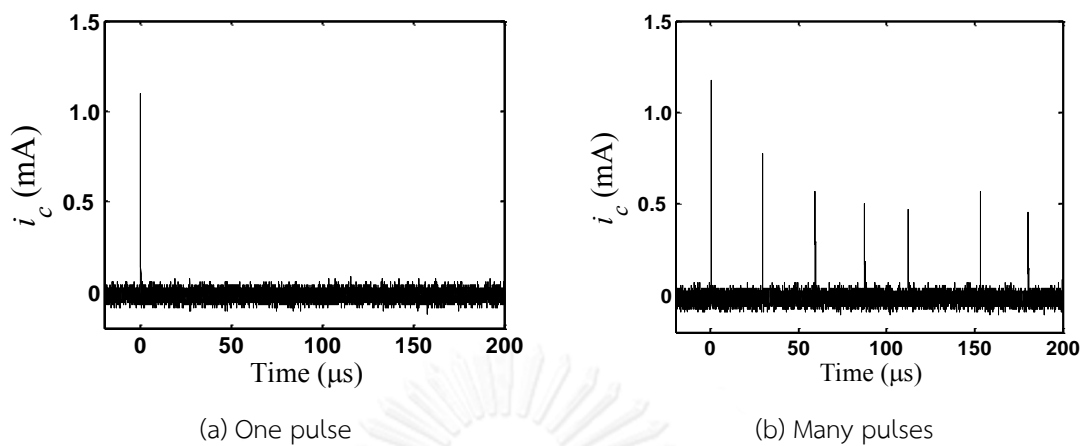
(a) One pulse

(b) Many pulses

Figure C2. Waveform of corona current under positive voltage application.

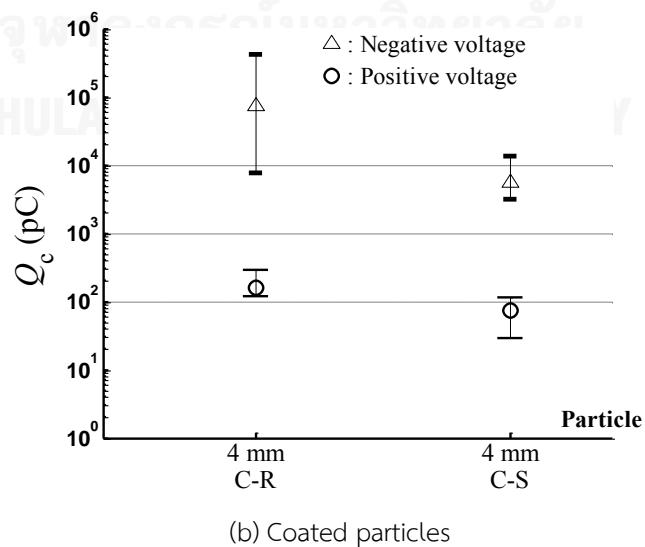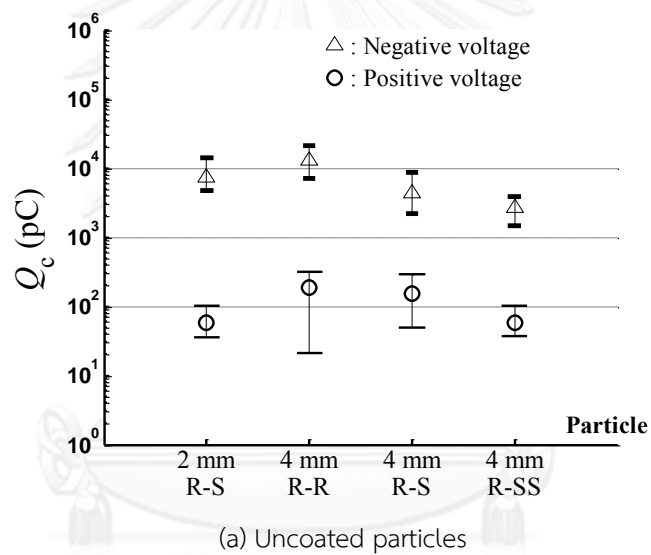(a) Uncoated particles

(b) Coated particles

Figure C3. Charge amount of the first corona current pulse.

Under the negative voltage application, the corona discharge often develops into a complete breakdown via the particles. For the uncoated particles, the probability of the complete breakdown was about 20%. For the coated particles, the probability was 100% for the C-R particles and 85% for the C-S particles.

C2. Corona discharge during movement

Experiments were done to detect the corona discharge that might occur during the particle movement. The particle movement was observed with a high speed camera, and the corona current pulses were measured by a digital oscilloscope through a detecting resistor. The oscilloscope and the camera were synchronized with a 40 ns delay. The experiments used the 4 mm R-R, R-S, R-SS, and S-S uncoated particles, and the 4 mm C-R, C-S, and CC-S coated particles. Positive and negative waveforms were used in the experiments. The voltage waveform applied to the upper electrode is shown in Figure C4, which was generated by a DC high voltage power supply. The voltage magnitude was 8.3 kV with a rise time of about 200 ms. The uncoated particles were subject to 60 tests under negative voltage and 100 tests under positive voltage. For the coated particles, the number of test was 40 and 90 under negative and positive voltage, respectively. In the experiments, the initial orientation of the particles on the grounded electrode was random.
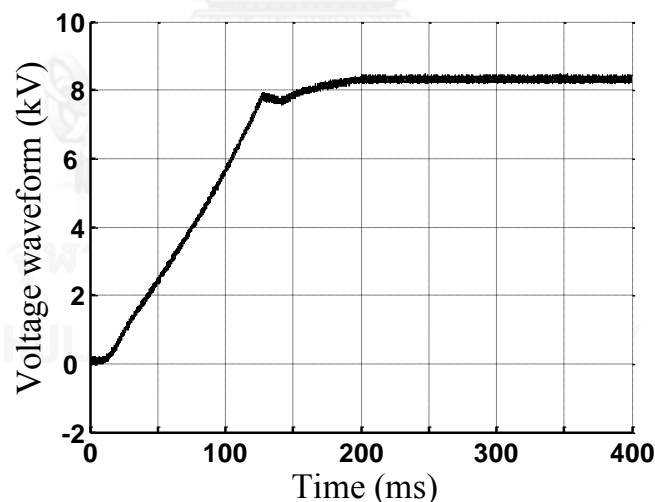

Figure C4. Voltage waveform applied to upper electrode.

a) Under negative voltage

For the behaviors that the uncoated and coated particles moved immediately to the upper electrode after departure from the grounded electrode or the coated particles rotated on the electrode, no corona discharge was detected.

There was 1 test showing that the R-SS particle fell on the electrode after departure. In this test, one corona current pulse was detected before falling. The charge due to this pulse was −2400 pC. Note that, this value was extremely greater than the charge amount acquired from the contact with the lower electrode before departure.

b) Under positive voltage

Similarly to the case of negative voltage application, corona discharge did not exist in the immediate lift behavior and always occurred before the particle fell on the electrode for both uncoated and coated particles. When the separation between the particle and the electrode was greater than about 0.5 mm, only one corona current pulse was recorded. The charge due to the pulse was between +50 pC and +200 pC. It is noticed that the induced charge on the particles before discharge was between −45 pC and −144 pC, which are the charge values for lying and standing positions under the positive voltage application, respectively.

When the uncoated particle rotated on the electrode, the corona discharge at the upper end was observed together with the microdischarge between the lower end and the grounded electrode, as shown in Figure C5a. The discharge current pulses are shown in Figure C5b. As shown in Figure C5b, the number and magnitude of the positive current pulses was predominant. This means that the corona discharge at the upper end took place more frequently with larger degree.

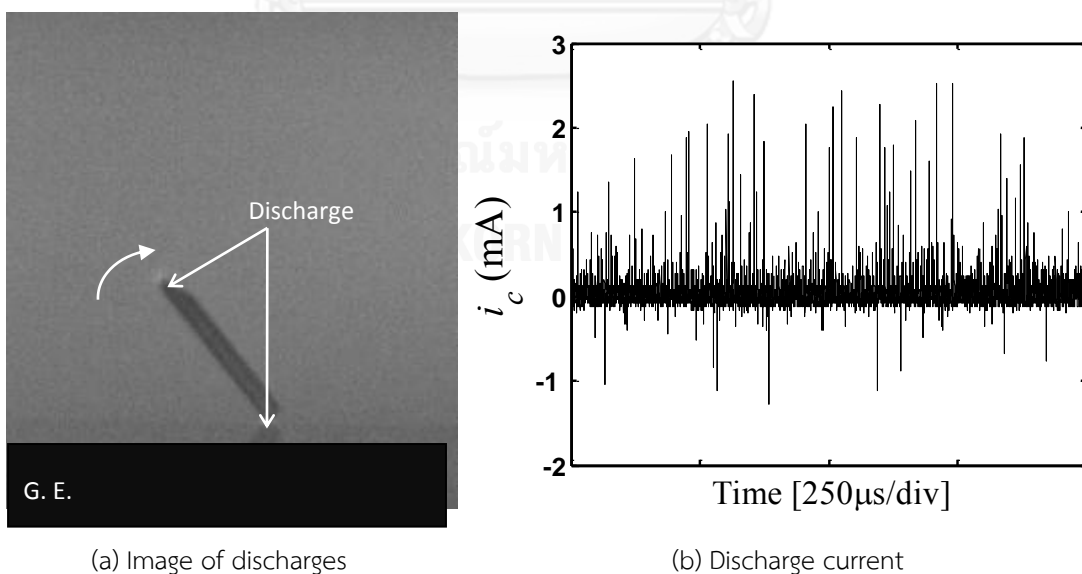(a) Image of discharges   (b) Discharge current

Figure C5. Discharge at two ends for the rotation of the uncoated particles on the grounded electrode.

When the coated particle rotated on the electrode, no corona discharge was detected, similarly to the case of the negative voltage application. For bounce behavior on the electrode of the coated particle, one or a few corona current pulses were recorded when the particles obtained a tilt angle greater than 60° with the grounded electrode. Figure C6 shows the recorded images and corona current pulses during the bounce behavior.
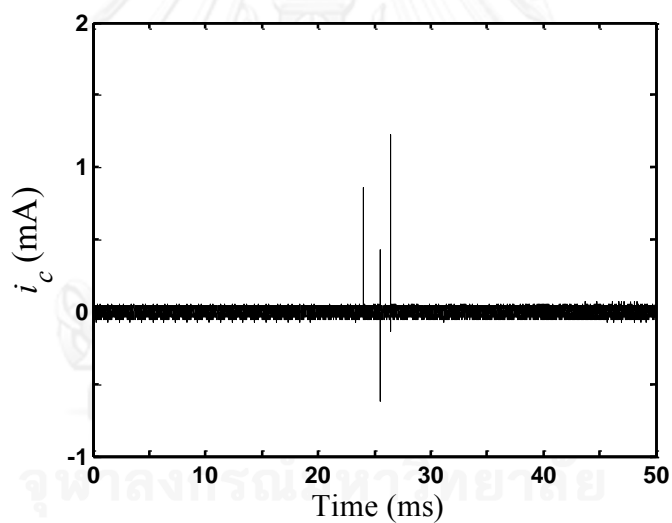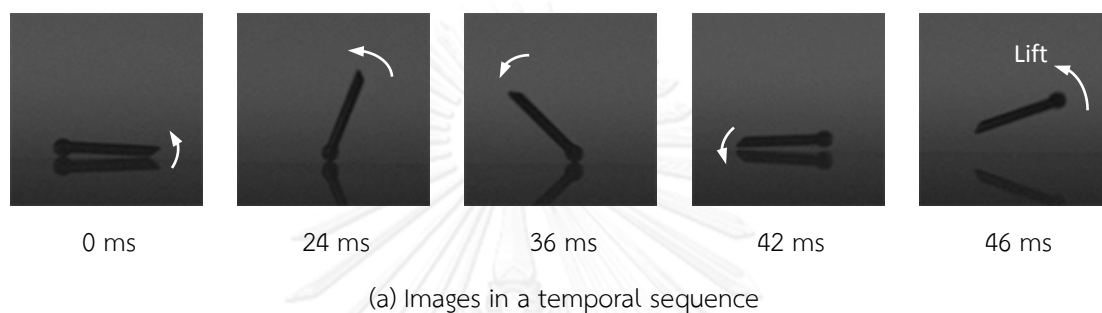

| 0 ms | 24 ms | 36 ms | 42 ms | 46 ms |

(a) Images in a temporal sequence

(b) Corona current pulse

Figure C6. Recorded images and corona current pulses during the bounce behavior of the coated particles.

VITA

Viet Quoc Huynh was born in Ben Tre, Vietnam, in 1985. He received the Bachelor's degree in electrical engineering from Ho Chi Minh City University of Technology, Vietnam, in 2008. He has been granted a scholarship of the AUN/SEED-Net (www.seed-net.org) to pursue the master and doctoral degrees in electrical engineering since 2009. He conducted the graduate studies at the High Voltage Laboratory, Department of Electrical Engineering, Faculty of Engineering, Chulalongkorn University, Thailand. His research interests are the analysis of electric field in high voltage engineering and the electromechanics of non-spherical particles under electric field.